An Investigation of Graph Signal Processing Applications to

Muscle BOLD and EMG

An Investigation of Graph Signal Processing Applications to Muscle BOLD and EMG

By Thaejaesh Sooriyakumaran, B.Eng

Master of Applied Science (2022)

School of Biomedical Engineering

McMaster University

Hamilton, Ontario, Canada

TITLE: An Investigation of Graph Signal Processing Applications
                   to Muscle BOLD and EMG

AUTHOR: Thaejaesh SOORIYAKUMARAN, B.Eng

SUPERVISOR: Dr. Michael D. NOSEWORTHY

NUMBER OF PAGES: xvii,167

Lay Abstract

Magnetic Resonance Imaging(MRI) and electromyography (EMG) are techniques used in the analysis of muscle, for detecting injury or deepening the understanding of muscle function. Graph Signal Processing (GSP) is a methodology used to represent data and the information flow between positions. While GSP has been used in modelling the brain, applications to muscle are scarce. This work aimed to model muscle activation using GSP methods, using both MRI and EMG data. To do so, a method for being able to simultaneously record MRI and EMG data was developed through hardware construction and the software implementation of EMG signal filtering. The collected data were then used to construct multiple GSP models based on the coherence and complexity of the signals, the goodness of fit for each of the constructed models were then compared. In conclusion, it is feasible to use GSP to model muscle activity with multimodal MRI and EMG data. This shows promise for future investigations into the applications of GSP to muscle research.

Abstract

Graph Signal Processing (GSP) has been used in the analysis of functional Magnetic Resonance Imaging(fMRI). As a holistic view of brain function and the connections between and within brain regions, by structuring data as node points within the brain and modelling the edge connections between nodes. Many studies have used GSP with Blood Oxygenation Level Dependent (BOLD) imaging of the brain and brain activation. Meanwhile, the methodology has seen little use in muscle imaging. Similar to brain BOLD, muscle BOLD (mBOLD) also aims to demonstrate muscle activation. Muscle BOLD depends on oxygenation, vascularization, fibre type, blood flow, and haemoglobin count. Nevertheless the mBOLD signal still follows muscle activation closely. Electromyography (EMG) is another modality for measuring muscle activation. Both mBOLD and EMG can be represented and analyzed with GSP. In order to better understand muscle activation during contraction the proposed method focused on using GSP to model mBOLD data both alone and jointly with EMG. Simultaneous mBOLD imaging and EMG recording of the calf muscles was performed, creating a multimodal dataset. A generalized filtering methodology was developed for the removal of the MRI gradient artifact in EMG sensors within the MR bore. The filtered data was then used to generate a GSP model of the muscle, focusing on gastrocnemius, soleus, and tibialis anterior muscles. The graph signals were constructed along two edge connection dimensions; coherence and fractility. For the standalone mBOLD graph

signal models, the models' goodness of fits were 1.3245×10^{-05} and 0.06466 for coherence and fractility respectively. The multimodal models showed values of $2.3109 \times {}^{-06}$ and 0.0014799. These results demonstrate the promise of modelling muscle activation with GSP and its ability to incorporate multimodal data into a singular model. These results set the stage for future investigations into using GSP to represent muscle with mBOLD, EMG, and other biosignal modalities.

Acknowledgements

Throughout my time in graduate school, I have been helped by many and would like to give them my thanks: Firstly, to my supervisor Dr. Michael Noseworthy, who welcomed me into the lab and the world of magnetic resonance. For tutelage about much more than engineering, for travelling across the Atlantic Ocean, for life advice, for friendship, and for some great stories. I also want to thank Dr. Huibregt De Bruin for all of the guidance over the past years, from the construction of EMG systems to how to live a more carefree life. To Dr. Dinesh Khumbare for watching over the project for the past two years, with insight into muscle activation and excitation. To the technologists at the St. Joseph's Hospital Imaging Research Centre, who taught me so much about how the scanner works and even more on the not-so-odd chance the scanner was not working. A thanks goes to the research team, be it asking questions on how to set up a protocol or a delivery of cookies, they have always been welcoming. A special thanks to Ethan Danielli, Nicholas Simard, and Cameron Nowikow for a wonderful time at ISMRM. An extra special thank you to both Joshua McGillivray and Alejandro Amador, without whom, this thesis would not have been possible. From the late nights in the lab wondering why the machine refuses to work, to the tours of Barcelona, could not have picked better friends to do it with.

To my parents Niva and Sooriya who were always ready to give everything they had, thank you. To Matana who watched me battle MATLAB code, win or lose,

who believed in me every step of the way, thank you. To my friends and family that supported me throughout the past two years, thank you. For all the others, who made it possible for this project to be completed, thank you.

Contents

List of Figures

List of Tables

Chapter 1

Lower Limb Background

1.1 Muscle

1.1.1 Anatomy

Muscle, due to its ability to contract, is the tissue responsible for movement. Muscular tissue is subdivided into three categories; cardiac, skeletal, and smooth, each having a specific role within the body (Noto et al. 2020); cardiac (i.e. heart) being responsible for circulating blood, skeletal being responsible for movement of bones, and smooth for peristaltic movement of the viscera and vasoconstriction in arterioles. The following is a description specifically of skeletal muscle. Muscle is both highly vascularized and highly metabolically active. (Noto et al. 2020) It is a multi-nucleated tissue with high numbers of mitochondria per cell; this allows muscle to generate the large amounts of energy necessary for contraction.

The fundamental contractile unit is the sarcomere, comprised of myofilaments. Myofilaments come in two protein types; thick comprised of myosin, and thin made of actin.

Sarcomeres are joined end to end to form a myofibril. Muscle cells are referred

1
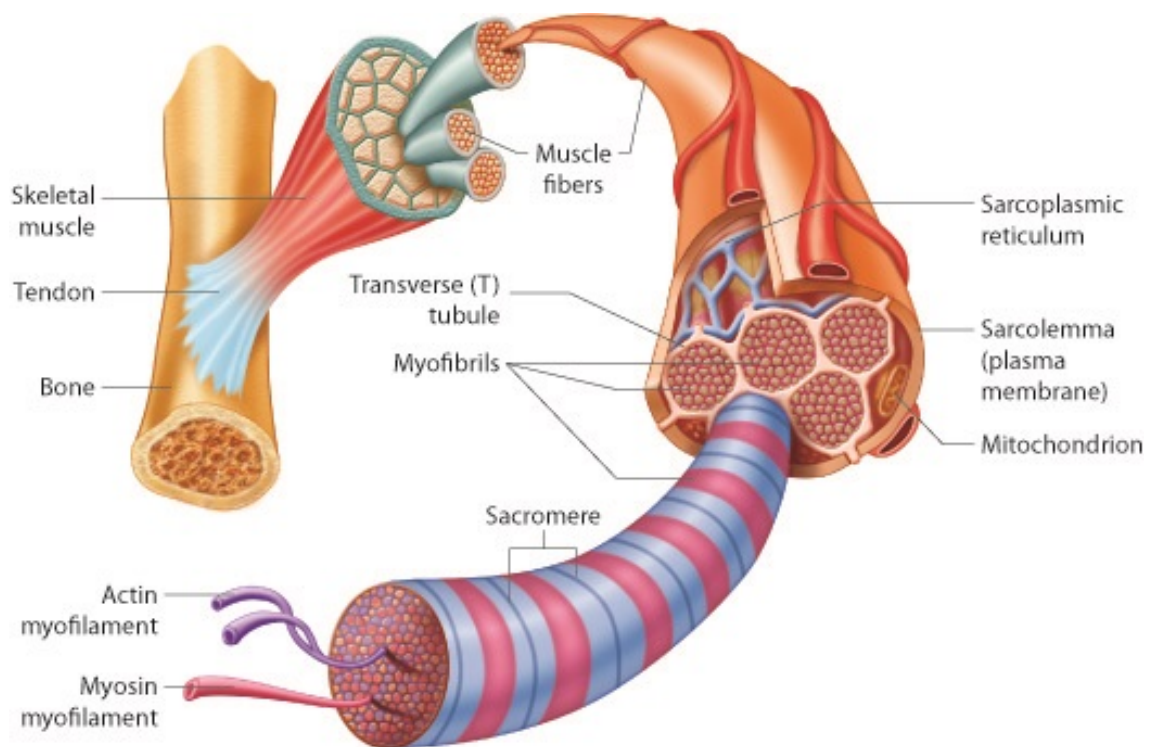
FIGURE 1.1: Muscle Structure Illustration: Visualization of Microstructure to Macrostructure. Sarcomere to Muscle, the hierarchical grouping of substructure. (Credits: "OLI - Drawing Structure of skeletal muscle - English labels" at AnatomyTOOL.org by Open Learning Initiative, license: Creative Commons Attribution-NonCommercial-ShareAlike)

to as muscle fibres and are made up of myofibrils. The fibres are multi-nucleated and elongated cells. These fibres are bundled within sheaths of connective tissues; the bundles are called fascicles. Groupings of fascicles, along with the vascular and nervous tissue, comprise a muscle (Noto et al. 2020).

Motor neurons are efferent neurons that innervate muscle fibres; a motor unit (MU) is defined as a motor neuron and all the muscle fibres that it innervates(Noto et al. 2020). A NeuroMuscular Junction (NMJ) is the junction between the motor nerve and the motor unit endplate. The endplate connects to the sarcolemma; a tissue that acts like a sleeve containing the myofibrils within a muscle fibre. (Noto et al. 2020) The sarcolemma invaginates deep into the muscle cells, the invaginations are termed transverse tubules (T-Tubules). Between the T-Tubules are sarcoplasmic reticuli (SR), hollow structures that contain Ca^{2+}. (Noto et al. 2020)

1.1.2 Physiology

The myofibrils actin and myosin found within muscle cells are responsible for contraction. The sliding of these myofibrils past each other allows for the contraction of individual sarcomeres; multiple sarcomeres contracting together is what allows a muscle fibre to contract. This contraction is fueled by high energy phosphate from adenosine triphosphate (ATP), which is maintained through the hydrolysis of phosphocreatine (PCr) to creatine (Noto et al. 2020). The binding sites on myosin are where ATP is hydrolyzed into ADP, the protein tropomyosin covers these binding sites. When Ca2+ is present, it causes troponin to bind to tropomyosin which then causes tropomyosin to uncover the ATP binding sites; allowing for contraction to occur (Noto et al. 2020). Muscle contraction is a metabolically demanding

action, sustained contraction requiring large amounts of energy. To have access to that much energy, glycogen, an endogenous polysaccharide macromolecule made up of multiple glucose units, is hydrolysed into multiple glucoses. The resultant glucose is then oxidized for energy via glycolysis, to generate the necessary amounts of energy for the muscle. In addition to the glucose, large amounts of oxygen is also needed (McLean et al. 2018; T. et al. 2013). This process is called aerobic respiration, and continues while sufficient oxygen is supplied. In the case that the energy demand outpaces the cardiovascular system's ability to provide oxygen to a muscle, the regime transitions from aerobic to anaerobic respiration (McLean et al. 2018). The energy deficit is compensated by using alternative pathways of extracting energy from the glucose molecules that do not rely on the supplied oxygen (T. et al. 2013). Anaerobic respiration is not used until aerobic respiration (and oxygen delivery) cannot keep up with demand because it is less efficient and creates waste byproducts, such as lactate, that need to be excreted (McLean et al. 2018; T. et al. 2013).

1.1.2.1 Electrophysiology

The motor neuron conducts an action potential (AP) from the central nervous system (CNS) to the motor unit towards a synapse that terminates at the neuromuscular junction (NMJ) (Noto et al. 2020). The AP crosses via a cholinergic synapse causing the muscle fibre to depolarize; however this creates not an AP but an end plate potential (EPP). The EPP opens voltage gated sodium (Na^+) channels resulting in an AP that is propagated by sarcolemma (Noto et al. 2020). The AP travels deep into the tissue along the sarcolemma, into the T-Tubules. The

AP triggers voltage gated Ca^{2+} channels lateral sac of SR, this kicks off contraction by releasing Ca^{2+} into the sarcomere. (Noto et al. 2020; Rodríguez-Carreño et al. 2012) The electrophysiological signal is called a motor unit action potential (MUAP), similar to an AP but encompasses all of the fibres in the motor unit (Noto et al. 2020; Rodríguez-Carreño et al. 2012).

1.1.2.2   Skeletal Muscle

Skeletal muscle is responsible for more than just movement; it plays a role in temperature regulation, and is vital to maintaining proper posture. Skeletal muscle is the only muscle tissue that can be voluntarily controlled, garnering it name voluntary muscle (Institute n.d.). Skeletal muscle is defined as muscles that connect to bone and actuate the skeletal system. This is generally the case, however, in the case of ocular muscles they connect to and actuate the eyeball. Skeletal muscle is attached to bones via tendons, these bundles of connective tissue aid muscles in movement by absorbing shock, and acting as springs to rebound energy. This rebounding is crucial to energy efficient movement, reusing energy that could otherwise damage the body if not properly counter-balanced.

Contraction/Activation Modes

The energy needed for contraction of muscle is supplied by constant levels of ATP, which is maintained by PCr. This releases energy that is then used by the muscle to contract. The ATP available to a muscle is limited by; ATP stores in the muscle, glycogen and triacylglycerols stores in the muscle, and the muscle's ability to generate ATP during sudden metabolic demand (Baker et al. 2010).

Muscles do not have large stores of ATP, with a density of 8mmol per kg of muscle (Baker et al. 2010). This ATP store is quickly depleted in highly metabolically active cells like myocytes. There are three pathways for replenishing the ATP; direct phosphorylation, aerobic respiration, and anaerobic glycolysis.

Direct phosphorylation, transfers a phosphate group from PCr to adenosine diphosphate (ADP), regenerating an ATP molecule. This is the fastest and most direct method of phosphorylating an ADP. It is so direct that the muscle stores much more PCr than ATP, since it can replenish direct ATP stores as they begin depletion. However PCr levels will also be depleted quickly, leading to the other two methods of ATP generation.

When PCr is low, phosphorylation will have to be performed using blood glucose and muscle glycogen. The glucose is broken down into pyruvate at which point the pathway splits based on oxygen availability. In the case of sufficient muscle oxygen supply and fibre perfusion, aerobic respiration will metabolize pyruvate via oxidative metabolism in the mitochondria to create carbon dioxide, water, and ATP. In the alternate case of insufficient oxygenation, pyruvate is reduced to lactic acid (via lactate dehydrogenase) in an anaerobic fashion and much less ATP is produced; 19 molecules of ATP are produced in aerobic respiration for every one in anaerobic respiration. (Rockel 2017)

Fibre Type

Skeletal muscle can be split into two fibre types; Type I and Type II. Type I are slow-twitch muscles designed for prolonged activation, and reduced reaction time compared to Type II. Type I fibres are also known as slow oxidative fibres. Slow-twitch fibres have increased delivery of oxygen and nutrients within the fibre.

Slow-twitch muscles also have large capillary systems to facilitate oxygen supply necessary for the large number of mitochondria to maintain aerobic metabolism. The oxygen is both stored and shuttled around the muscle fibre by myoglobin (*Muscle Fibre Types* 2022). Slow oxidative fibres have large amounts of this protein which increases oxygen delivery and consequently the endurance of the fibre type (*Muscle Fibre Types* 2022; *Human Skeletal Muscle Fiber Type Classifications | Physical Therapy | Oxford Academic* 2022).

Type II are fast-twitch muscles. These are better suited for short duration contraction, with greater speed and force. Fast-twitch fibres respond faster but are not suited for extended periods of activation. Type II is further divided into two subcategories; Type IIa and Type IIb. The majority of fast-twitch fibres are Type IIb, or anaerobic fibres with reduced oxygen demand. This results in reduced mitochondrial numbers and blood supply. On the other hand, Type IIa fibres perform oxidative metabolism(*Muscle Fibre Types* 2022). Type IIb fibres are called fast glycolytic fibres, while IIa fibres are also called fast oxidative fibres. The fibre type composition of a skeletal muscle is drives the functional characteristics of the muscle. Muscles that require the ability to exert great amounts of rapid force have larger proportions of fast-twitch fibres, while the so called "anti-gravity" muscles associated with posture and stabilization are primarily slow-twitch fibres that are more suited to long, constant contraction(*Muscle Fibre Types* 2022; *Human Skeletal Muscle Fiber Type Classifications | Physical Therapy | Oxford Academic* 2022).

Exercise

Exercise is defined as the flexion of muscles. The ends and purposes of which are dependent on the scenario. An exercise paradigm can greatly impact the way the muscles function and are used. Flexion and relaxation, onset and offset, nutrient and oxygen supply will all be influenced by multiple factors.

Muscle contraction can be divided into two categories defined by muscle tension and length; isometric and isotonic. Isometric contraction refers to the length of a muscle staying static while tension changes, whereas isotonic contraction is maintenance of muscle tension while muscle length changes. The change in length of isotonic contraction has two further divisions; the elongation of the muscle is eccentric and the shortening of the muscle is concentric.

The efficacy of the contraction of a muscle is dictated by the anatomy of the joints and the force exerted by the muscle. The anatomy is important as it directs the force of a contracting muscle in a desired direction. If a muscle crosses over a joint, it will act upon; if it attaches to a bone, it will pull on it. This is made evident by antagonistic muscles such as the biceps and triceps muscles of the upper arm. They both actuate on the elbow and it is the differences in attachment that make the biceps responsible for flexion of the elbow and the triceps for extension.

The contractile force generated by a muscle can be modeled as a function of its cross sectional area (Zamparo et al. 2022). This shows that a muscle's force output is non-linear along the length of its contraction, as the change in cross sectional area is also non-linear along its range of motion. Interpreting this to the micro-scale it is due to the sarcomeres producing highest amounts of tension when there is a certain overlap of the thick and thin filaments. Either more or

less overlap results in reduced output. The contractile force of a sarcomere is due to molecular cross-bridge activation binding. The hydrolysis of ATP causes the cross-bridge to extend in order to attach to actin, then the cross-bridge undergoes the power stroke before detaching from the actin. This results in the movement of one filament in reference to another, shortening the distance between sarcomere z-discs. This cycle will repeat causing further contraction. This is done en masse by the sarcomeres leading to the contraction of the entire muscle. This explains why innervation of muscle is so deep, and why asynchronous contraction of sarcomeres within a muscle creates irregularities in contraction. This may have side-effects such as; reduced coordination and delaying full contraction.

Recovery

While a muscle is contracting, resources are being used to perform the activity. The units of a muscle are self-limiting in their exertion, preventing the muscle from contracting to the point of damaging the contractile units. There is strong negative feedback from the Golgi tendon organs. Though undamaged, the offset of exertion causes the muscle to enter a recovery stage that can be differentiated from the muscle at rest as it is physiologically different.

The muscle is not able to perform to the same extent during recovery. This could be short lived while the muscle is flushed with blood to supply oxygen, replenish nutrients, and remove by-products of the exertion. It could also be longer term if the muscle must be physically repaired from the damage.

For a muscle that has undergone exercise that only used ATP stored in the muscle, the recovery will be characterized by the restoring ATP. For a muscle that was exerted to the point of direct phosphorylation, recovery will also incorporate

the replenishing of PCr within the muscle. Furthermore for a muscle recovering from anaerobic respiration, in addition to the ATP and PCr replenishment, lactate must be cleared and the resultant acidic effectson the local environment must be repaired.

1.1.3   Innervation

The innervation of muscle differentiates itself from other tissues as the innervation penetrates deep into the tissue so that the entirety of the muscle contracts in synchrony. This is facilitated by the anatomy of the muscle, with deep reaching transverse tubules and sarcolemma.

1.1.4   Blood Supply/Vascularization

Muscle is a very resource intensive tissue, requiring elevated blood flow to supply resources. Each muscle is home to many capillaries; the more capillaries the lesser the diffusion distances of oxygen and nutrients. This also greatly increases the muscle's efficiency at removal of waste products into the blood stream. This is especially important when muscle is contracting. The flow of arterial blood into the muscle is restricted due to the morphological changes in muscle during contraction. This is inverse to venous flow. Skeletal muscle contraction compresses the compliant venous vasculature, increasing blood pressure. This drives blood through the body, preventing pooling of blood. The flow changes with extended contraction resulting in vasodilation, allowing increased blood flow. This extends the time a muscle can remain in the aerobic respiration regime and hastens recovery post contraction (*18.7C* 2018).
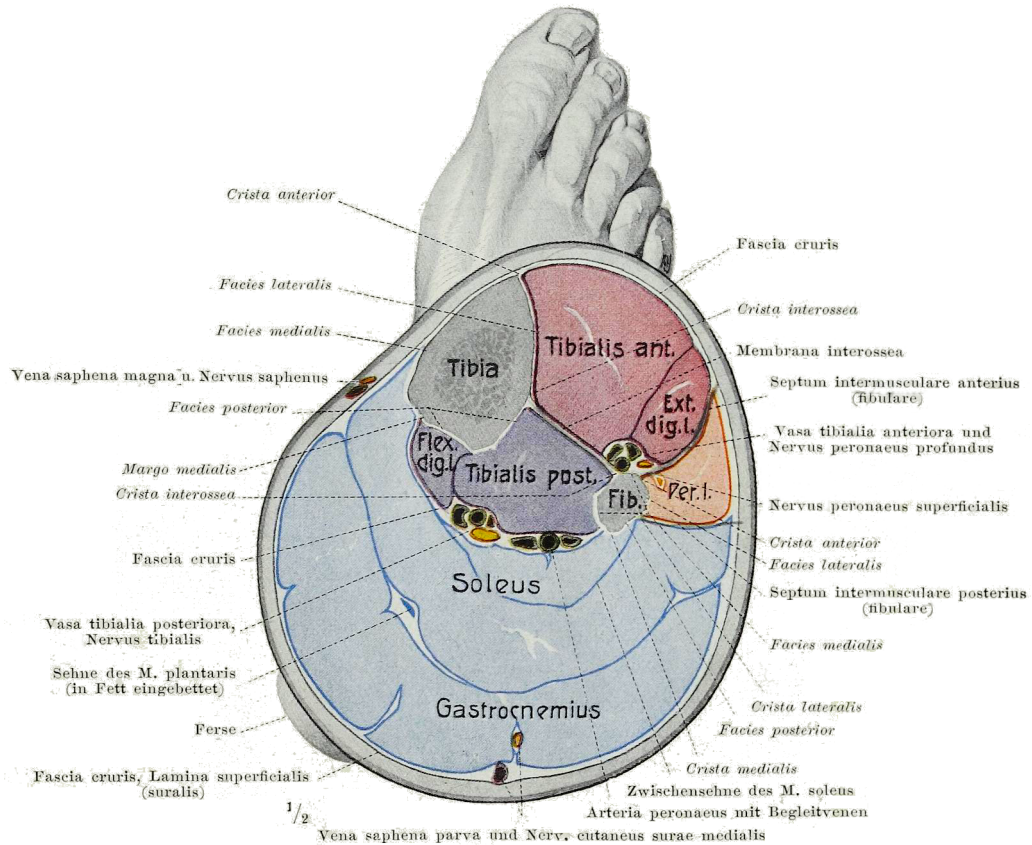
FIGURE 1.2: Cross Sectional View of Human Calf. Gastrocnemius, soleus, and tibialis anterior muscles are shown. The tibialis anterior shown lateral to the tibia. The soleus and gastrocnemius shown on posterior of the leg, with the soleus deep to the gastrocnemius. (Credits: from *commons.wikimedia.org* scanned from (Braus 1921))

1.2 Lower Leg

1.2.1 Skeletal Muscles

Anatomically, the lower leg is defined as the region between the knee and the ankle. In this area, there are a plethora of muscles necessary to move the ankle and toes through their large number of movements with limited effect on the knee.

1.2.1.0.1 Gastrocnemius

The gastrocnemius is the most superficial muscle on the posterior aspect of the lower leg. It is comprised of a medial and lateral head. It is a muscle that has a high fast-twitch fibre fraction and plays a significant role in explosive movements such as jumping. The medial and lateral heads originate from the medial and lateral femoral condyles respectively. These then insert into an aponeurosis that attaches alongside the soleus' tendon creating the Achilles tendon.

FIGURE 1.3: Gastrocnemious Muscle(Credits: Taken from *Gastrocnemius | Encyclopedia | Anatomy.app | Learn anatomy | 3D models, articles, and quizzes* 2022)

The gastrocnemius has two separate blood supplies, one for the lateral and one for the medial head. Separate as they may be, both are supplied by sural branches of the popliteal artery. The innervation of the gastrocnemius is done by the tibial nerve from the S1 and S2 levels of the spinal column (*Gastrocnemius* 2022).

1.2.1.0.2 Soleus

The soleus muscle is deep to the gastrocnemius and attaches to the Achilles tendon. Conversely to the gastrocnemius, the soleus has a high slow-twitch fraction. It plays a vital role in standing posture. The difference between the soleus and the gastrocnemius is the fibre composition differences. This difference generates huge disparities in function making the gastrocnemius more suited for quick, powerful movements and the soleus more for slow, sustained movements. Unlike the gastrocnemius, the soleus originates on the fibula, with a spread over the posterior aspect of the fibular head, posterior surface of the fibular, and to a tendon that connects the two other origin points. The soleus then joins with the gastrocnemius to insert into the Achilles tendon.

The soleus is supplied by the posterior tibial, peroneal, and sural arteries (*Soleus* 2022). Also, similar to the gastrocnemius, the soleus is innervated by the tibial nerve from the same S1 and S2 spinal levels.

1.2.1.0.3 Tibialis Anterior

The tibialis anterior is found on the anterior aspect of the lower leg, lateral to the tibia. It runs along the leg and inserts medially on the foot. Contraction of the tibialis anterior results in dorsi-flexion of the heel and inversion of the foot. The muscle also features very consistent muscle fibre orientation, making it ideal for imaging methods that are sensitive to fibres and their orientations. The tibialis anterior originates on the lateral side of the tibia, which it also runs along. The origin points include the lateral tibial condyle, the lateral surface of the tibial shaft and interosseus membrane (*Tibialis Anterior* 2022).
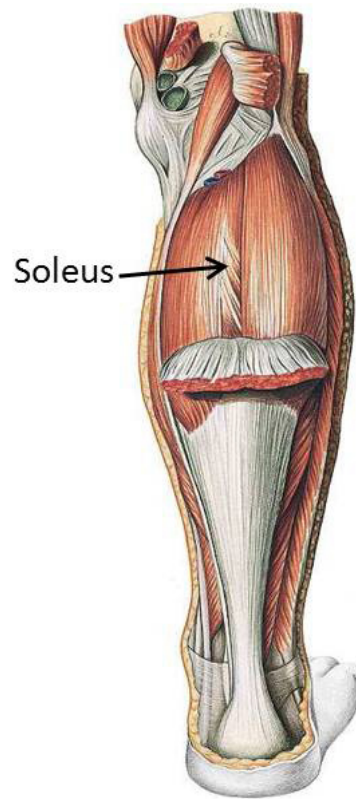
FIGURE 1.4:   Soleus   Muscle   (Credits: Taken   from *massagetherapy.com/articles/soleus-muscle-strain*

Due to the tibialis anterior being on the anterior aspect of the leg, the blood supply comes from the anterior tibial artery. The innervation differs from the gastrocnemius and soleus, and is innervated by the deep peroneal nerve from spinal levels L4, L5, and S1 (*Tibialis Anterior* 2022).

FIGURE 1.5: Tibialis Anterior Muscle (Credits: Taken from *mobilephysiotherapyclinic.in/tibialis-anterior-muscle-details/*

Chapter 2

MRI and Applications in Muscle

2.1   MR Theory

Nuclear magnetic resonance (NMR) is the fundamental basis underlying magnetic resonance imaging (MRI). It begins with the use of a large static magnetic field (B_0) to affect (align) nuclear spins. The spins are then excited using radio frequency (RF) pulses that are modeled as a tipping of nuclear gyrating axes away from the direction of the main magnetic field. As nuclei precess back into alignment with the field, they release energy which induces a voltage in an appropriately tuned RF receiver coil. Due t its abundance the proton (i.e. hydrogen, ^{1}H) is the most routinely probed atomic nucleus. The frequency at which a proton will precess is proportional B_0 and to its gyromagnetic ratio, γ the product of which is called the Larmor frequency. This is defined by the equation:

$$\omega = \gamma * B \tag{2.1}$$

The gyromagnetic ratio of hydrogen is 42.58 MHz/T. Therefore for a field strength of 3 Tesla, the Larmor frequency of hydrogen is 127.74 MHz.

2.2 MRI

For spatial localization pre-defined (in space and time) linear non-uniformities in B_0 are introduced. This is accomplished by superimposing three orthogonal linear magnetic field gradients (X, Y, Z) at specific timings and with varying amplitudes. The imaging pulse sequence manipulates these gradients in order to encode imaging space. The manipulation of these gradients also allows for different types of scans to be performed, permitting the imaging of different tissue properties. Equations 2.2 to 2.4 show the individual formulae for each of the gradients, the gradients are defined as the derivative of the field with respect to a cardinal direction. Equation 2.2 describes the X gradient as the spatial derivative of B_z along the X-axis. Any of these can be substituted into the Larmor frequency calculation, doing so replaces Equation 2.1 with Equation 2.5, creating an equation that can be used to calculate the Larmor frequency as a function of location. Furthermore Equation 2.6 describes field strength at a specific position.

$$G_x = \frac{\partial B_z}{\partial x} \tag{2.2}$$

$$G_y = \frac{\partial B_z}{\partial y} \tag{2.3}$$

$$G_z = \frac{\partial B_z}{\partial z} \tag{2.4}$$

$$\omega(x) = \gamma B(x), \omega(y) = \gamma B(y), \omega(z) = \gamma B(z) \tag{2.5}$$

$$B(x) = B_0 + x \cdot G_x \tag{2.6}$$

17

These equations describe the resultant frequency encoding of spins along those directions. This is also accompanied with phase and slice encoding directions. The phase encoding is done to create a phase gradation along a direction that is used to back-calculate the position of a proton based on its phase. Following that is the slice selection gradient that is used to determine the slice that is being imaged.MRI is capable of collecting three dimensional images, this is generally done by collecting multiple two dimensional slices. The collected two dimensional slices are in the frequency domain. The Fourier transform is a mathematical operation capable of converting spatial domain information into frequency domain information. MRI takes the collected frequency and phase data and uses the inverse Fourier transform to convert the slices into spatial domain data. Although MRI is well suited for resolving details, meaning it has fine spatial resolution, it is not suited for detecting rapid changes; in other words MRI has poor temporal resolution. Acquiring the images requires RF pulse to tip the alignment of the nuclei away from the main field. These sequences are designed to create desired tip angles and field realignment.

The two basic families of pulse sequences are spin echo and gradient echo. The Former, in the most basic sense, has a refocusing RF pulse that minimizes loss of signal due to differences in magnetic susceptibility. The latter refocuses spins with a gradient, and although faster than spin echo is more sensitive to magnetic susceptibility. Using combinations of operator set parameters echo time (TE) repeat time (TR) and flip angle 9for gradient echo, not spin echo) one can result in different contrast weightings, called T_1 and T_2 weighted images. Both types of weighting can be achieved with either spin echo or gradient echo. T_1 weighted images have bright fat and dim water as fat is fast to return to an equilibrium

state, whereas water is slower (Vadera and Jones 2009).

2.3 The BOLD Effect

Blood oxygen level dependent (BOLD) imaging is a method of acquiring functional magnetic resonance imaging (fMRI) data first described in 1990 (Ogawa et al. 1990). Its function hinges on the oxygenation state differences of hemoglobin, oxygenated hemoglobin (oxyHb) being diamagnetic with deoxygenated hemoglobin (deoxyHb) being paramagnetic (Ogawa et al. 1990; Murphy and Gaillard 2008). This means blood flowing to supply a tissue with oxyHb will exhibit diamagnetic qualities and after supplying the tissue it will gain paramagnetism as deoxyHb. In order to image this change, the MRI sequence must be capable of highlighting the hemoglobin's change in magnetic susceptibility. A T_2* weighted image is used to measure this change, it should be noted that it is also susceptible to other inhomogeneities in the field, such as those due to the structure of the subject (Murphy and Gaillard 2008). The following equations relate the change in signal T_2 with changing magnetic field inhomogeneity:

$$\frac{1}{T_{2*}} = \frac{1}{T_2} + \frac{1}{T_{2'}} \tag{2.7}$$

$$\frac{1}{T_{2*}} = \frac{1}{T_2} + \Delta B_0 \gamma \tag{2.8}$$

T_2* is the effective T_2 decay, with the change in homogeneity in the field creating a shift from the expected T_2. The difference from homogeneity of the field is due to the magnetic susceptibility of the tissues and tissue structures interacting

with the field, resulting in deflections in the field lines away from homogeneity. This is shown in Equation 2.7 with the T_2' term, which represents the shift in the expected T_2 as the product of the difference from the expected field strength and the gyromagnetic ratio.

As BOLD is dependent on blood flow and oxygenation, it is used to determine metabolic activation in the body (Ogawa et al. 1990). Blood flow to the brain is related to mental load, meaning that BOLD can be used to observe regions of brain activity. This is not limited only to the brain, BOLD can also be used to image other tissues. For example, muscle, which is highly vascularized, requires large volumes of oxygen when active (Jordan et al. 2004). Using BOLD to image muscle can glean information on muscle function and status. Carcinomas also have high levels of vascularization and oxygen use, therefore BOLD could is used to measure activity within cancerous tissue(Baudelet and Gallez 2002).

2.4   BOLD Imaging

BOLD imaging builds on the BOLD effect, which uses a gradient-echo pulse sequence that is sensitive to differences in magnetic susceptibility induced through changes in the ratio of oxyHb/deoxyHb. Using a cylindrical sample with a magnetic susceptibility model $\Delta\chi$:

$$Outside Cylinder : \frac{\omega_s}{\omega_0} = 2\pi\Delta\chi(\frac{r}{a})^2[(2cos^2\theta - 1)] \tag{2.9}$$

$$Inside Cylinder : \frac{\omega_s}{\omega_0} = \frac{-2\pi}{3}\Delta\chi \tag{2.10}$$

The model represents the frequency shift ω_s created by the magnetic susceptibility, with: r and θ being the polar coordinates of the position in respect to the center of the cylinder, and a as the radius of the cylinder(Ogawa et al. 1990). Ogawa et al. assumed the field to be homogeneous within the cylinder, and noted that the T_2 decay is quadratically related to the blood water oxygenation (Ogawa et al. 1990).

BOLD imaging in the brain, aims to measure neuronal activity by correlating neuronal activation with metabolism which, in turn, is reliant on blood oxygenation. The approach indirectly measures activation via a MR signal change that is comprised of a combination of changes in cerebral blood volume (CBV), cerebral blood flow (CBF), and the cerebral metabolic rate of oxygen consumption (CMR_{O_2}). However, this indirect measurement is closely correlated with neuronal activation (Lajoie et al. 2016; Huber et al. 2019). BOLD is an easily accessible and widely accepted technique.

2.5 Functional MRI (fMRI)

BOLD plays a tremendous role in fMRI as the foremost used technique, so much so that the terms BOLD and fMRI have colloquially become interchangeable. However as new techniques are developed, other functional imaging methods have become valid options for assessing function. Researchers have also used methods such as; arterial spin labeling (ASL), vascular space occupying (VASO) imaging, and calibrated fMRI as methods to more directly measure the underlying phenomena that BOLD indirectly measures (i.e. CBF, CBV, and CMR_{O_2} imaging)
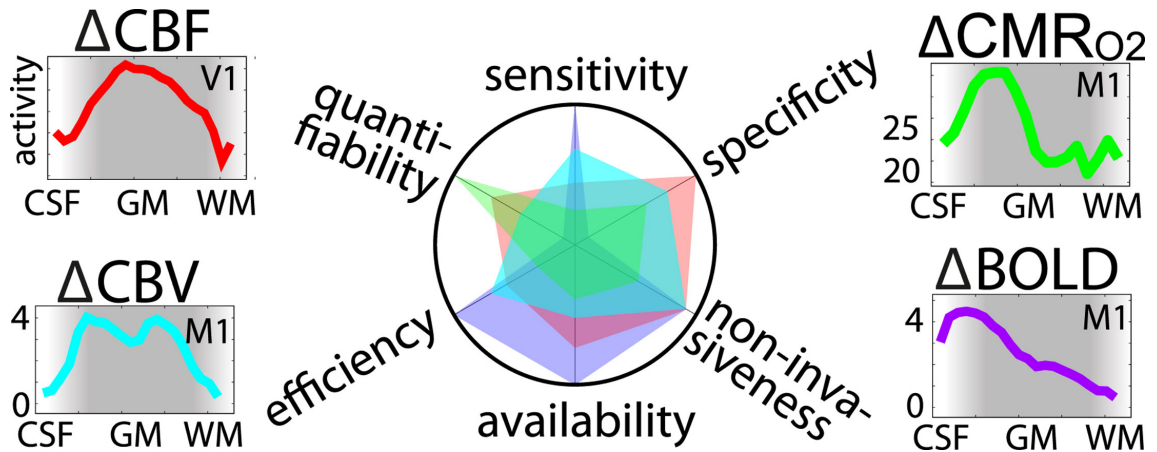
FIGURE 2.1: fMRI Alternative Options: These alternatives might be better served imaging muscle exercise and its underlying physiology than muscle BOLD. They would need to be re-calibrated for muscular tissues as opposed to grey and white matter. (Credits: Reprint with permission from (Huber et al. 2019) from Elsevier Publishing)

(Huber et al. 2019). Each method has advantages and drawbacks compared to BOLD. As seen in Figure 2.1,

Another parametric mapping technique is chemical shift imaging (CSI) where the spectroscopic amplitude of a molecular NMR peak is used. Furthermore advancements in acquisition technologies and methods have started to blur the lines between fMRI and functional magnetic resonance spectroscopic imaging (fMRSI). Being able to perform spectroscopy acquisitions on a voxel level resulting in a functional image, brings the two fields closer together. Leftin et al., as seen in Figure 2.2, has shown that fMRSI of muscle activation is possible with interleaving a stimulus (Leftin et al. 2014).
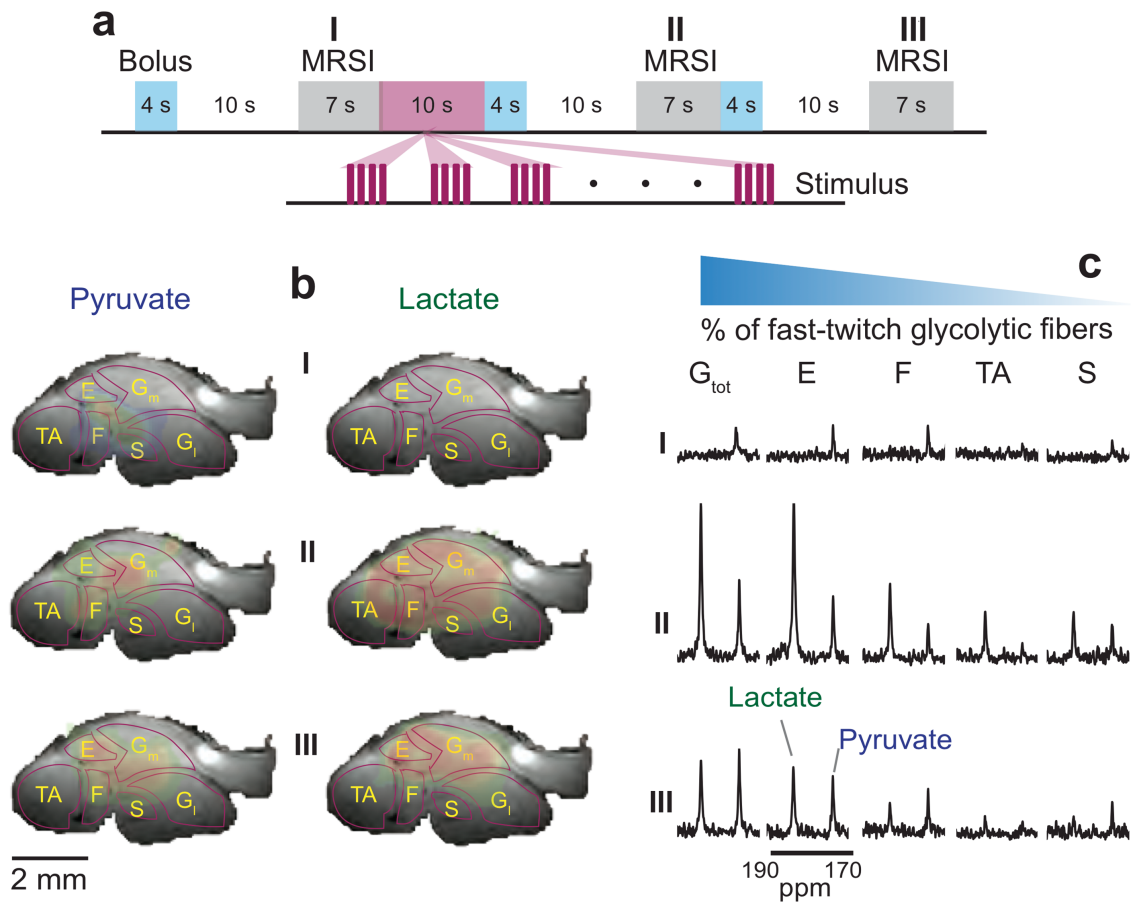
FIGURE 2.2: Functional Spectroscopy Imaging: Imaging of Pyruvate and Lactate over time in response to stimulus in murine leg. Imaging paradigm with bolus, stimulus, and imaging interleaved. Translation of this sequence to human models can be a powerful tool for imaging metabolite levels during exercise. (Credits: Reused from *doi.org/10.1371/journal.pone.0096399.g005*)

2.5.1   Muscle BOLD (mBOLD)

BOLD MRI techniques have been adapted for uses outside of the brain. Muscle BOLD (mBOLD) has become both a clinical and research tool. As oxygen exchange occurs in muscle and thus Hb paramagnetic changes, BOLD is well suited for imaging muscle. The large blood and oxygen demand of active muscle creates strong BOLD contrast. That being as it may, mBOLD has differences and confounding factors not noted in cerebral BOLD. The fibre composition, for example, plays a role in BOLD. Due to Type I, IIa, and IIb skeletal muscle fibres having different physiological and chemical properties, the BOLD effect can vary between them. This is further muddled by the fibre to fibre variations in myoglobin, distance from a capillary, or the time varying oxygenation status of the fibre. Some factors such as myoglobin, as discussed below, have a direct impact on BOLD measurement.

2.5.1.1   Myoglobin and Hemoglobin

Myoglobin (Mb) is a molecule similar to Hb. It is found throughout skeletal muscle. The half-saturation pressure of Mb is an order of magnitude lower than that of hemoglobin, resulting in a greater oxygen affinity. In skeletal muscle, unlike other tissues, myoglobin can be desaturated(dMb) when performing rigorous exercise or during ischemic bouts. That being said, the BOLD portion of myoglobin cannot be easily measured in vivo due to the presence of hemoglobin (Michel et al. 2019). "The blood oxygen level dependent (BOLD) effect of in-vitro myoglobin and hemoglobin" reaffirmed what Ogawa et al. had discussed in their seminal BOLD paper about the oxygenation effects of hemoglobin on its T_2 and T_2* values (Michel

et al. 2019). However, Michel et al. also studied the effects of oxygenation on the measured decay constants of myoglobin, observing a BOLD-like effect. This was done using equine metmyoglobin (metMb) that was converted into MbO_2. For various oxygenation levels of Mb and Hb samples; T_1, T_2, T_2*, and balanced steady-state free precession (bSSFP) mapping were done.

2.5.1.2   mBOLD and Oxygenation

As per its namesake, mBOLD fMRI has been used extensively to assess the impact of oxygen supply to muscle on its function. Many studies have induced changes in oxygen supply to study the response or to emulate musculo-vascular conditions that similarly impact muscle. For example, induced ischemia is popular as it is easy to perform via tourniquet and can gleam insight into the muscle's response to transient oxygen shortage.

The offset of induced ischemia causes reactive hyperemia as an inrush of blood is supplied to the muscle which also creates learning opportunities. Reactive hyperemia emulates the elevated blood supply of post-contractile hyperemia without the interference of muscular contraction during the scan. Be that as it may, the differences between post-contractile and reactive hyperemia have been studied. The differences determine the efficacy of reactive hyperemia as a viable emulation of post-contractile hyperemia.

As research continues, confounding factors of the mBOLD technique are discovered in addition to alternative theories and perspectives on its function. The contraction of muscle restricts the inflow of arterial blood while increasing the outflow of venous blood (*18.7C* 2018). Vasodilation of arteries results in increases in blood flow, creating a characteristic blood flow curve around contraction that can be

modelled. This hemodynamic response can be implemented to better model contraction.

The oxygen availability to the muscle and its oxygen requirements come in three flavours; hypoxia, hyperoxia, and normoxia. When there is adequate oxygen supply to a muscle it is deemed normoxia. The other two are when the supply and demand do not match up. Hypoxia is a lack of oxygen whereas hyperoxia is an excess of oxygen to the muscle. Though categorized under hypoxia and hyperoxia, there are many different causes that can result in either case. The simplest is contractile hypoxia as the oxygen demand of the muscle outpaces the available supply. This is followed by post-contractile hyperoxia as the increased blood flow lingers after contraction ends, leading to an excess supply of oxygen to the muscle. Induced hypoxia is the synthetic creation of a hypoxic environment by restricting blood flow through the use of tools such as a tourniquet. This also leads to a state of transient hyperemia when the tourniquet is removed causing a large influx of blood bringing oxygen along with it resulting in reactive hyperoxia. All of these have different physiological responses, each of which needs to be further studied to create a holistic understanding of muscle oxygenation.

Another application for BOLD-like measurements is as a metric of muscle oxygen extraction, measuring not the activation but the oxygen used. Uwano et al. investigated the oxygen extraction fraction (OEF), using a quantitative susceptibility mapping (QSM) method with a 7T scanner in brain (Uwano et al. 2017). This was done to replicate the OEF measurement done with positron emission tomogrophy (PET) and was done using T_2* weighted 3D images and a multiple dipole-inversion algorithm (Uwano et al. 2017). The OEF maps were based on differences in susceptibility seen in brain tissue and the venous structures (Uwano

et al. 2017). There is an opportunity for this QSM-OEF to be applied to muscle studies.

(Chopra et al. 2009) also contrasted BOLD R_2* and oxygen electrode measurements. R_2* is the reciprocal of T_2*, shown in Equation 2.12. The study showed promise for R_2* as a prostate cancer hypoxia quantifying metric.

$$R_2* = \frac{1}{T_2*} \tag{2.11}$$

In 2016 Lajoie et al., investigated mapping $CMRO_2$, OEF, and the BOLD calibration parameter M. Using quantitative O_2(QUO2), a calibrated BOLD methodology (Lajoie et al. 2016). Simultaneously they measured cerebral blood flow (CBF) and R_2* during rest, hypercapnia, and hypoxia. The team created multiple maps of oxygen, blood flow, and R_2*, that were then used to estimate reproducibility. Within and between subject variabilities were calculated for seven regions. The reproducibility metrics of grey-matter for O_2 delivery, M, and OEF were 3.87%, 16.8%, and 13.6% respectively(Lajoie et al. 2016), indicating more research is needed to decrease noise levels.

2.5.1.3   mBOLD and Muscle Function

The resultant BOLD image is further affected by the specific muscle in question, its fibre type composition and oxygenation status. Furthermore there are other factors such as age, athletic status, or disease.

With age, muscle conditioning and composition changes. Consequently age is a factor in mBOLD imaging that must be considered. The atrophy and loss of muscle fibres with age is not uniform within a muscle nor is it consistent with muscle

or muscle fibre type. Fast-twitch fibres are preferentially atrophied, skewing the signal (Falaschi and Marsh 2021). There is also a neurological factor involved as the force production reduction is not totally explained by the loss of muscle volume (Wilkinson et al. 2018). This is also accompanied by anabolic resistance that develops in the elderly (Wilkinson et al. 2018). Unsurprisingly athletic conditioning impacts muscle and measurements of muscle activation. Resistance exercise leads to increase muscle perfusion, increased neurological connection, increased muscle protein synthesis, and increased recovery. It is widely accepted that fibre type composition determines athletic inclinations. Sports requiring explosive power will benefit greatly from Type II fibres with their larger diameters and wide-ranging sarcoplasmic reticulum, allowing for faster and harder contraction through the rapid and perfuse release of calcium. For endurance applications, Type I fibres are more suited. The rate of recovery of athletes is higher than those with a sedentary lifestyle.

Disease can impact the muscle and imaging of the muscle. The effect of which depends on the disease and its interaction with the BOLD effect. Peripheral arterial occlusive disease (PAOD) is a form of atherosclerosis. It manifests as occlusions and stenoses within the blood vessels. This then leads to changes in muscle microvasculature and muscle composition change which ultimately affects mBOLD as the blood supply is affected (Partovi et al. 2012). Another disease that also affects muscle vasculature on the micro and macro levels is diabetes; affecting the BOLD image that is tied to the vascular function of muscle(Partovi et al. 2012).

Smoking is an activity with a plethora of deleterious impacts on the body. One such impact is a reduction of lung function. One secondary effect includes change in muscle blood flow response (MFR) which then indirectly changes the temporal

response of mBOLD data. This impacts the BOLD signal of smokers relative to non-smokers presenting as longer $T_{1/2\text{peak}}$ and time to peak (TTP) (Nishii et al. 2015).

Muscle function is unique to each muscle, as previously discussed, the fibre composition of a muscle is heavily influenced by the function. Donahue et al. used simultaneous gradient-echo and spin-echo echo planar imaging (EPI) to image graded ischemia in muscle (Donahue et al. 1998). When measuring relaxation rates for both gradient- and spin-echo the response varied between gastrocnemius and soleus muscles. This suggested that susceptibility dependent techniques may be used for mapping ratios of large and small blood vessels within muscle (Donahue et al. 1998). This can be extrapolated to map fibre type fractions in muscles, due to difference in vascularization in fast and slow twitch fibres.

2.5.1.4   mBOLD and Field Strength

The equations that govern MR imaging are dependent on the field strength and thus systems with differing field strengths will vary in response. The following equations show that T_2^* changes depending on the strength of the static field B_0, due to the T_2' term that accounts for inhomogeneities of the field. This inhomogeniety could be caused by; the homogeneity of the static field, materials within the field that are external to the tissue of interest, or the tissue itself.

$$\frac{1}{T_{2*}} = \frac{1}{T_2} + \frac{1}{T_{2'}} \tag{2.12}$$

$$\frac{1}{T_{2*}} = \frac{1}{T_2} + \Delta B_0 \gamma \tag{2.13}$$

$$M_0 = \frac{\rho_0 \gamma^2 \hbar}{4kT} B_0 \tag{2.14}$$

$$M_{\mathrm{x}}(t) = M_0 e^{\text{-t}/\mathrm{T_2}} sin(\gamma B_0 t) \tag{2.15}$$

$$M_{\mathrm{y}}(t) = M_0 e^{\text{-t}/\mathrm{T_2}} cos(\gamma B_0 t) \tag{2.16}$$

$$M_{\mathrm{z}}(t) = M_0 (1 - e^{\text{-t}/\mathrm{T_1}}) \tag{2.17}$$

Equation 2.14 shows the relation between the field inhomogeneities and the effective T_2 decay. The M_0 denotes the net magnetization, which is dependent on the target nuclei density, gyromagnetic ratio, field strength, Plank's constant, Boltzmann constant, and temperature.

Since the effective T_2 of MRI changes with field strength, the images also changes. Thus it is necessary to verify that techniques that work at one field strength are still viable at another. As seen in Equations 2.12 to 2.17, the measured T_2^* is dependent on field strength. Equations 2.16 and 2.17 specifically show the transverse magnetization components, and consequentially the measured signal is a function of T_2. Equation 2.18 shows that the longitudinal magnetization is not affected by the T_2, this is expected as T_2 is known as the transverse relaxation time. It can also be shown that the noise in the system is proportional to the strength of B_0, however the signal increases according to B_0^2 thus the signal-to-noise ratio (SNR) increases linearly with B_0(Robert et al. 2014). The larger field strength also interacts more with regions of high bulk magnetic susceptibility (BMS), meaning that field homogeneity is more easily affected by endogenous sources of magnetic susceptibility, such as the oxygenation status of hemoglobin. Therefore, for applications that make use of BMS, changes will show more distortion at higher field strengths. The magnetic susceptibility effects increase with B_0 and some that are negligible at lower field strengths must be accounted for at higher field strengths(Robert et al. 2014).

$$CylinderInternalFieldShift = \frac{\Delta\chi}{6}(3cos^2\theta - 1)B_0 + \frac{1}{3}\chi_{e}B_0 \qquad (2.18)$$

$$CylinderExternalFieldShift = \frac{\Delta\chi}{2}\frac{a^2}{\rho^2}(sin^22\phi)B_0 + \frac{1}{3}\chi_{e}B_0 \qquad (2.19)$$

The local field effects of the vessels are modelled by an infinite cylinder. This model shows part of the impact of field strength on the BOLD signal, the field inhomogeneity is modelled as linear with field strength but as shown, this is not directly linear with signal (Robert et al. 2014). Equations 2.19 and 2.20 show the field shift internal and external to a cylinder with a susceptible material composition. With χ being the susceptibility, a being the diameter of the cylinder, θ being the angle of the cylinders to the field, ρ and ϕ are the polar coordinates for the model. This model translates from brain BOLD to muscle BOLD as the structure of muscle can be modelled as cylinders, therefore there is room for the modelling of the muscle BOLD signal building on the cylindrical model already used in brain. This model is used throughout brain imaging, in muscle BOLD it is even more relevant due to the structure of muscle being comprised of hierarchical sizes of fibrous structures. From the muscle fibre down to the sarcomere, all can be modelled as cylinders with internal and external field shifts. This is also shown in the mBOLD R_2* assessments of Towse et al. discussed below (Towse et al. 2016).

2.5.1.5 Multimodal mBOLD

Imaging modalities each have their strengths and weaknesses. Pairing modalities can improve outcomes by covering the weaknesses of the combined modalities with the strengths of the others. This comes in multiple forms; compensation for spatial

or temporal resolution, redundancy in measurements, or additional dimensionality. Arm over head (AOH) is an imaging position designed to permit the BOLD imaging of brain and forearm muscle simultaneously. The study by Tang et al. focused on the connection between default brain modes and muscular activation. Finding that there may be default mode networks responsible for muscular activation, only possible by combining brain BOLD imaging and muscle BOLD imaging (Tang et al. 2020).

Ledermann et al. concurrently measured mBOLD, TransCutaneous Oxygen Pressure (TCPO$_2$), and Laser Doppler Flowmetr y(LDF). This was done to compare the mBOLD signal intensity with the more quantitative measures of blood oxygenation. Calculating the correlation of mBOLD measurements through the time course of reactive hyperemia, showing differing results for varying parameters (Ledermann et al. 2006).

Towse et al. used a multimodal approach in their efforts to quantify mBOLD viability at 7T, since the R$_2$* of muscle changes with field strength (Towse et al. 2016). Using an induced ischemic protocol in conjunction with both Doppler ultrasound and Near-InfraRed Spectroscopy (NIRS) to measure blood flow and oxygenation changes in scans at 3T and then again at 7T, they found R$_2$* at 7T was greater than at 3T by nearly a factor of 6. From this work they concluded 7T had increased sensitivity to muscle vasculature (Towse et al. 2016).

2.6 Electromyography (EMG)

Electromyography (EMG) records the electrical activity generated during muscle activation. EMG records MUAPs through electrodes, as well as amplifying, filtering, and processing the signal. EMG can be single or multi-channel, meaning singular or multiple readings can be made concurrently. In general, multi-channel recordings result in multiple concurrent parallel readings. EMG requires electrodes, be they surface electrodes or invasive. Invasive electrodes offer greater signal fidelity as they are closer to the source, at the cost of being recorded from a smaller volume of tissue and not representing the activity of the whole muscle. Surface electrodes are widely used as they are non-invasive and are more representative of the entire muscle's activity. The signals at the skin are in the microVolt to milliVolt ranges, thus amplification is needed; however amplifying such small signals results in the amplification of any noise resulting in the needed for filtering and processing. EMG can capture rapid changes, with high temporal resolution, but lacks in spatial resolution (in comparison to MR imaging). When using surface electrodes the signal passes through multiple tissues before reaching the electrode, thus pinpointing specific motor units is difficult.

2.6.1 Application

Recording MUAPs from a MU grants insight into the function of the muscle, this information can then be used to assess and diagnose the state of the MU. MUAP waveforms have distinct components that each represent a step in the MUAP generation process, variations from the norm can be inspected to determine the causes of any malfunctions.Another application of EMG is for control, since it

captures MUAPs that are meant to control muscle, the signals can also be used to control electronics. These signals can be fed to prostheses or augmentations.

2.7 Multimodal fMRI

The idea of using other modalities alongside fMRI is not new, Allen et al. published in 2000 discussing the removal of imaging artifacts introduced into EEG signals during fMRI scanning. (Allen et al. 2000) The paper addresses one of the major hurdles of multimodal systems, intermodal noise, the noise introduced into a signal due to another modality. In this case, the noise introduced into the fMRI readings are negligible unlike the impact the fMRI has on the EEG. The gradient switching of the MRI induces large amounts of noise that swamps out the EEG signal, This noise has to be removed using processing procedures. The method proposed by Allen et al. later known to be the Allen method is to have a channel measuring only the gradient noise and then subtracting that from the noisy EEG signal. This is shown to denoise the signal to a significant level. (Allen et al. 2000) This has become a staple technique for the combined use of EEG and MRI, and a starting point for more advanced techniques to be developed to better remove gradient noise.

EMG and fMRI have been used together, Behr built a system to collect the concurrent data and remove gradient artifacts from the EMG data (Behr 2016). A custom built EMG system sampling at 4kHz was utilized alongside a General Electric MR750 3T MRI scanner fitted with an extremity coil with 8 channels. The data underwent artifact removal, the method being an adaptation of the FASTR procedure outlined by Niazy et al. originally designed for EEG/fMRI (Niazy et

al. 2005). Consisting of slice timing alignment, artifact template subtraction, followed by principle component analysis (PCA) residual removal, and adaptive noise cancelling (Behr 2016). The experimental procedure consisted of two experiments; one with a phantom and one with a human participant. The main scans being EPI BOLD with parameters; TE = 35ms, TR = 250ms, flip angle = 33 degrees, 3-4 10mm thick slices. The human experiment focused on plantar flexion of the right medial gastrocnemius in a block design using 30% and 50% of the participants Maximum Voluntary Contraction(MVC).

EMG, fMRI, and Graph Theory have been explored by Piovanelli et al. using a sEMG array in concert with T_2 mapping of the right forearm, termed muscle functional MRI(mfMRI) (Piovanelli et al. 2020). The muscle currents were then modelled using graph theory using the fMRI data to segment the data and register the electrodes in space. Back calculation of the signals generated a conductance matrix throughout the forearm and also patterns for the currents within the muscles(Piovanelli et al. 2020). The team created a novel method for assessing muscular currents specific to the anatomy and function.

An alternative imaging technique to BOLD is parametric T_2 mapping (Lota et al. 2017). T_2^* mapping is also possible using gradient echo sequences. It is used in cardiomyopathy imaging for viewing iron overload (Lota et al. 2017). Physiological mechanisms for T_2 have been proposed; the earliest hypothesis is the post contraction hyperemia resulting in the increased signal intensity. It has been shown that perfusion effects alone are not enough to generate the signal increase. Oxygenation level of the tissue is another possible explanation. T_2^* does decreases along with oxygenation yet during reperfusion the T_2^* decay does not return along with the hyperperfusion. Later understanding points to muscle water moving to

the myofibrillar space (Patten et al. 2003).

Chapter 3

Graph Signal Processing, Stockwell Transform, and Spatio-Time-Frequency Representations

Graph Signal Processing (GSP) is a technique capable of replicating physical and functional connections by manner of how it constructs the dataset. It can be used to represent MRI data, by way of generating a sparse functional connectivity map of sampled points. The GSP approach to data focuses not only the specific points that were sampled but also the features between points presented as edges(Ortega et al. 2018).

The Stockwell Transform (ST) is a technique for converting time and space domain signals into signals in time, space, and frequency (Battisti and Riba 2016; Wang n.d.). It has seen use in geology, climatology, and increasingly in medical imaging. In its simplest form, the Stockwell Transform is a alternative to the Fourier Transform that is Gaussian windowed in time and space, resulting

in a spatio-temporal frequency representation. However the applications of the Stockwell Transform have been hindered by its high order dimensionality leading to infeasibly high memory usage. This makes it functionally impossible to use the Stockwell Transform on larger images and especially functional data over time(Wang n.d.).

GSP can be used to circumvent this issue by reducing the size of data transformed. Instead of transforming an entire volume-time series, singular or groups of points can be transformed and linked via Graph edges (Ortega et al. 2018). The use of GSP to compensate for this drawback is investigated in this study using muscle functional MRI (fMRI), also known as muscle BOLD (mBOL). Focused on the three muscles of Tibialis Anterior (TA), Gastrocnemius (GC), and Soleus (SOL), this study investigated the use of GSP and the ST for classifying intermuscular and intramuscular activation.

3.1 Graph Signal Processing

Graph Signal Processing(GSP) is a technique capable of replicating physical and functional connections by manner of how it constructs the dataset. Used to represent MRI data, it can generate a sparse functional connectivity map of sampled points. The GSP approach to data focuses not only on the specific points that were sampled but also features between points presented as edges (Ortega et al. 2018).

3.1.1 Graphs

Graphs are a data structure that contain data within two different forms; nodes and edges. Structurally, nodes are positions within the graph and the edges are the connections between nodes. The data is contained in both the nodes and the edges. This can be used to represent many things, most commonly for navigation where the nodes represent locations and destination while the edges represent the distance between nodes, time to travel between nodes, and traffic between the two nodes. This also takes advantage of the fact that edges can be multi-dimensional, holding information from multiple information types.

3.1.2 Graph Signals

A graph signal is a signal superimposed over the graph. This can be in the form of a time varying signal. For example the temperatures in different locations throughout the week embedded as a time varying signal overlaid onto node data. This is not specific to nodes, the edges can also be representing a changing signal. Graph signals are now a combination of data structure and a signal. This means processing methods for both are now possible. Traversal of graphs is an area of mathematics with wide ranging economic and logistical applications.

3.1.3 Graph Signal Processing

Data can be represented in multiple ways; the default is the one in which the data were acquired. The data may be grouped together in space or time; but there is no relationship defined between data points, other than the position of adjacent voxels. A Graph is defined by a set of points, named nodes or vertices,

and connections between them are called edges. Imposing a signal over the nodes and edges of a Graph is called a Graph Signal. This change in representation may seem trivial, but it allows for Graph Signal specific processing methods and visual representations, that may be more intuitive to viewers. The field of processing Graph Signals is known as Graph Signal Processing (GSP).

3.2 Stockwell Transform

3.2.1 Frequency Domain Representation

The field of signal processing depends heavily on spectral analysis; the analysis of a signal after converting it into the frequency domain. The main method of frequency domain transformation is the Fourier Transform (FT), the issue with the FT is that the generated frequency spectrum is a time averaged one. Meaning that any time dependent frequency components are indiscernible. This is not an issue with just the FT but frequency domain representations as a whole. The solution to this issue is found in joint time-frequency domain representations.

3.2.2 Time-Frequency Domain Representation

These representations simultaneously represent the data in time and frequency, so time dependent frequency components are preserved. That is not to say that all transforms for generating time-frequency domain representations are created equal. The Short-time Fourier Transform (STFT) uses a sliding window and generates multiple frequency spectra over time, outputting a spectrograph. The Wavelet Transform (WT) is another time-frequency transform, but phase information is

not absolutely referenced and amplitude response varies with frequency. These drawbacks are mitigated in using the Stockwell Transform (ST). Which uses a Gaussian window.

3.2.3 Generalized Fourier Transform

The differences between these transforms can be highlighted by first outlining the similarities (Wang n.d.). A Generalized Fourier Transform (GFT) for a single dimensional signal is described as:

$$GFT(t, f) = \int\limits_{-\infty}^{\infty} x(t)w(t - \tau, \sigma)e^{-j2\pi ft}dt \tag{3.1}$$

The aforementioned transforms can be represented using the GFT equation with differences between them shown. Firstly the Fourier Transform, is easily fit to the GFT form when the window function $w(t - \tau, \sigma)$ is a constant, more specifically 1.

Fourier Transform Equation as a GFT variant:

$$FT(f) = \int\limits_{-\infty}^{\infty} x(t)e^{-j2\pi ft}dt \tag{3.2}$$

As shown by the GFT form of the Fourier Transform, it can be considered one which has a singular time window over all time resulting in the expected time averaged spectrum. Other transforms are only minor differences away from the standard Fourier Transform. Introducing a rudimentary windowing function in place of the constant results in the STFT. The window function has σ of constant

value shifting $w(t - \tau, \sigma)$ into $w(t - \tau)$. This window can be filled using popular windows such as: Hanning, Hamming, Rectangular, etc.

STFT as GFT variant

$$STFT(t, f) = \int_{-\infty}^{\infty} x(t)w(t - \tau)e^{-j\omega t}dt \qquad (3.3)$$

The STFT window is used to create multiple frequency spectra over time, resulting in a spectrograph. This represents the change in frequency over time. The Wavelet Transform is another method of generating a time-frequency representation.

WT as GFT variant

$$WT(a, b) = \frac{1}{\sqrt{a}} \int_{-\infty}^{\infty} \overline{\Psi(\frac{t - b}{a})}x(t)dt \qquad (3.4)$$

The Wavelet Transform is inherently different from Fourier based transforms in that it is not based on the same basis function. Where the FT uses sinusoids, the WT uses a Mother Wavelet that is chosen by the user. In this case, the Fourier Transform can be considered a sub-form of the WT that uses a sinusoid as its Mother Wavelet in place of another such as: Haar, Daubechies, Morlet, or others. This is observed in Equation (3.4); the sinusoid basis otherwise known as the kernel of the GFT, $e^{-j2\pi ft}$ and the window function $w(t - \tau, \sigma)$ have been combined into $\overline{\Psi(\frac{t-b}{a})}$. Where a and b are the scaling and time shifting factors respectively. In contrast to the STFT, the WT window both translates and scales. The scaling term a is analogous to the σ in the GFT window, and is non-constant when compared to the STFT. To this effect, the Stockwell Transform can be considered

a mix of the STFT and the WT. Retaining the sinusoidal kernel of the STFT and having a scaling window function that is explicitly a Gaussian with $\sigma = f$.

3.2.4 Stockwell Transform

ST as a GFT variant:

$$ST(\tau, f) = \int\limits_{-\infty}^{\infty} x(t)\frac{|f|}{\sqrt{2\pi}}e^{-\frac{(t-\tau)^2 f^2}{2}}e^{-j2\pi ft}dt \tag{3.5}$$

Classic description of the ST:

$$ST(\tau_x, \tau_y, \tau_t, f_x, f_y, f_t) = \int\limits_{-\infty}^{+\infty}\int\limits_{-\infty}^{+\infty}\int\limits_{-\infty}^{+\infty} h(x, y, t)\frac{|f_x||f_y||f_t|}{(\sqrt{2\pi})^3}\cdot$$
$$e^{-\frac{(x-\tau_x)^2 f_x^2 (y-\tau_y)^2 f_y^2 (t-\tau_t)^2 f_t^2}{2}}\cdot \tag{3.6}$$
$$e^{-j2\pi(f_x x + f_y y + f_t t)}dxdydt$$

The Stockwell Transform Gaussian window is generated over all dimensions of the input signal. This creates a multidimensional space that contains temporal, spatial, and spectral information.

The Stockwell Transform was used in this investigation due to the its benefits over the Wavelet Transform. In comparison to the WT, the ST retains information about phase in respect to the input signal. That is not to say it does not come with its drawbacks. The main drawback is the sheer size of the output, the number of dimensions is double that of the input as seen in Equation (3.6).

This can quickly balloon out of hand, as the output becomes less and less manageable as the size of the input grows, limiting large images or higher sampling frequencies. A small volume-time series of size 256x256x4x1024 can be stored

in memory using 256MB, after transforming using the ST in four dimensions it becomes size 256x256x4x1024x256x256x4x1024 requiring size 65536TB. As regions or time spans of interest increase, the amount of memory needed to work with the ST can become unruly or impossible to compute, greatly impeding the feasibility of the ST for image processing. This can be circumvented by using small regions of interest.

Nyquist, Redundancy, and the DOST: When sampling in digital systems, discrete data is collected and discrete transforms are used. The discretized form of the ST, DST is available, but another form is better used.

The Nyquist-Shannon sampling theorem outlines the relationship between the frequency content of a signal and the necessary sampling rate to capture that signal. This implies that for a given frequency content, sampling frequencies higher than the Nyquist sampling rate prove less necessary and increasingly redundant. In the case of a time-frequency representation, the lower frequency components require less resolution than the higher frequency components. Thus a constant sampling frequency is redundant; this also applies to the Stockwell Transform, leading to the use of the Discrete Orthogonal Stockwell Transform(DOST). The DOST creates a more Nyquist-Shannon efficient output compared to the standard DST.

3.3 Stockwell Transform + Graph Signal Processing

Using a Graph Signal, containing multiple nodes within regions of interest can greatly reduce the effective region of interest and thus make the use of the Stockwell Transform without running into computational roadblocks. This method creates an opportunity for multi-resolution analysis of data features at and between points and anatomical regions. Expanding on the concept of nodes, the establishment of layers of nodes can provide more insight. Renaming the single voxels so far called nodes as micronodes, and the 3x3x3 block centered around the micronode as a macronode. The information contained between micronode and macronode can show local changes in the time-frequency representation. This sparse-ST generation will reduce the aforementioned example image data from 256x256x4x1024 to 3x3x3x1024 (256MB to 27kB/macronode) and the post-ST size from $(256x256x4x1024)^2$ to $(3x3x3x1024)^2$ (65536TB to 729MB/macronode). The total amount of memory required for the macronode subsampling method will depend on the number used, but is drastically less than that needed for the entire volume series.

Chapter 4

Problem, Hypothesis, and Objectives

4.1 Problem Definition

The proper function of muscle is vital in the maintenance of walking and sitting posture, mobility, individual autonomy, among others. Studying the activation of muscle pre, during, and post-voluntary contraction is pivotal in understanding how to maintain normal muscle function through disease, injury, and aging. Analysis of muscle function and physiology is a field that is rapidly expanding. Various techniques have been adapted from other areas to analyze muscle. The use of GSP, not used previously with muscle, has been used in the analysis of brain images. Just as brain GSP has allowed for the observation of network activation trends and other unique metrics, muscle GSP could show promise for illuminating new understanding in muscle. To date, there is no methodology for modelling muscle activation using a GSP approach nor for the multimodal representation of muscle in a single data structure.

4.2 Proposed Solution

The proposed solution aimed to use a GSP approach to assess mBOLD data collected from calf muscles of healthy males. An exercise paradigm was used that had muscles contracting and resting in intervals. The data was acquired concurrently with electromyography scans. The study was approved by the local research ethics board.

To improve computational memory efficiency the use of the node sub-sampling method, outlined in chapter 3, was used. The nodes were analyzed without the macronode structure due to the imaging parameters. The graph signals were constructed with coherence and fractility to assess two features within one structure. This was then fit and statistically analyzed to determine efficacy in representing the data with a goal of being a building block for further studies into muscle physiology with GSP.

4.2.1 Hypothesis

Muscle BOLD has been used as a measure of muscle activation to assess activation and function. Work in the brain has demonstrated the applicability of GSP to functional data. This investigation hypothesizes that the application of GSP to both mBOLD and EMG/mBOLD will result in a deeper comprehension of the physiology of muscle during voluntary contraction.

The objectives of this work were:

- To generate coherence and fractility graph signals for mBOLD signals derived from calf muscles with and without an accompanying EMG signal;

- To analyze generated graph signals with a Generalized Linear Mixed Effect (GLME) model as a statistical test to determine which feature-set is most suited to modelling voluntary plantar flexion;

- To create a processing pipeline that can be expanded upon in future explorations of muscle GSP.

Chapter 5

Methods

5.1 Experimental Subjects

The studies described below were all performed on 10 healthy volunteers aged 23 to 31 (10 male, mean age $= 25.6 \pm 5.4$). The research was funded from a Natural Sciences and Engineering Research Council (NSERC) Discovery Grant to Dr. Michael Noseworthy and was approved by our local research ethics board (Hamilton Integrated Research Ethics Board, HiREB).

5.2 EMG

The EMG system consisted of 6 parts; the electrodes, leads, extension cable, EMG amplifier, Analog to Digital Converter (ADC), and acquisition computer. The electrodes shown in Figure 5.22 were not EMG specific but MR compatible electrocardiogram (ECG) electrodes by ConMed (ConMed ClearTrace Radiolucent Electrode2700-003 adult ECG electrode, Utica, New York). The electrode featured the following specifications: MR safe, conductive gel adhesive, carbon snap, Ag/Ag chloride, and a waterproof membrane. These were used as they were easily

accessible within the lab with prior proof of viability for use with EMG (Behr 2016). Similarly, the leads for the EMG system were also MR compatible and designed for ECG. The leads were composed of non-ferrous carbon-fibres, and reduced the impact of the MR gradient fields on the acquired signal. The extension cable was used to extend the lead cable out to the 5 Gauss line within the MR room. It was also made of carbon fibre. The EMG amplifier was designed and assembled in house, with the PCB manufactured by JLCPCB (https://jlcpcb.com). The power supply(Analog Discovery 2 by Digilent, 1300 NE Henley Ct. Pullman, WA, USA) and ADC(NI USB-6221 by National Instruments, 11500 North MoPac Expressway Austin, TX, USA) were off-the-shelf systems sandwiching the amplifier.

5.2.1 EMG Amplifier Construction

The EMG amplifier was designed and built in house, with the printed circuit board sent out for manufacturing by JLCPCB. This was done using the free to use software EasyEDA (https://easyeda.com), to lay out both the circuit schematic and PCB routing. The amplifier was split into stages; pre-amplifier, amplification and filtering, and a variable amplification stage.

5.2.1.1 Electronics Design

Pre-Amplifier Design

The pre-amplifier was centered around the use of an instrumentation amplifier. Specifically the INA128. Instrumentation amplifiers are a component class used widely in bio-signal acquisition, due to the highly matched input impedances, high gain, and high CMRR. The instrumentation amplifier can be defined as an

operational amplifier with matched high impedance input buffer. This device also allows for the recording of a differential signal with regards to a reference signal. This stage also has programmable gain through resistor R1 shown in Figure 5.1. The gain resistor is calculated through the Equation 5.1.

$$G = 1 + \frac{50k\Omega}{R_{\mathrm{G}}} \tag{5.1}$$
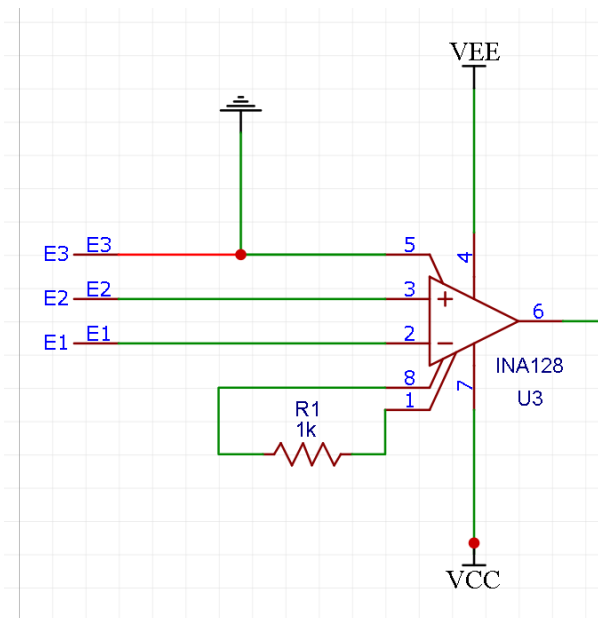
FIGURE 5.1: Instrumentation Amplifier Implementation: INA128 preamplifier stage, with 1kΩgain programming resistor. Reference electrode tied to reference voltage.

Filter Design

The filtering stage was a higher order cascade filter-amplifiers. The majority of which, were second order Sallen-Key filters with set gains. The Sallen-Key architecture was chosen for properties such as; stability, ease of design, filtering characteristics, and ability to be cascaded. The first filtering stage was a 2nd

order high pass filtering stage, this was chosen as the first stage as it removes low frequency components in the signal. This included the Direct Current (DC) portion of the signal so that it is not also amplified by the rest of the system. This allowed for more head room in amplifying the much smaller Alternating Current (AC) component. The high pass filtering also removed signal artifacts associated with movement which had a high fraction of low frequency components.
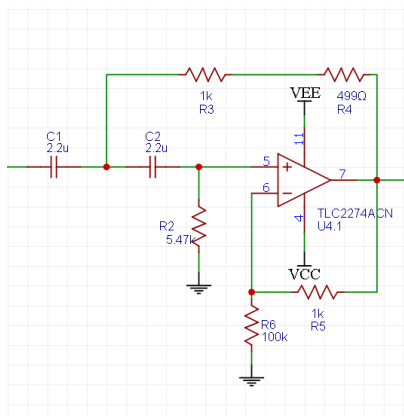
(A) High pass filter stage, 2nd order Sallen Key with frequency cut off of 25Hz and gain of 1.01
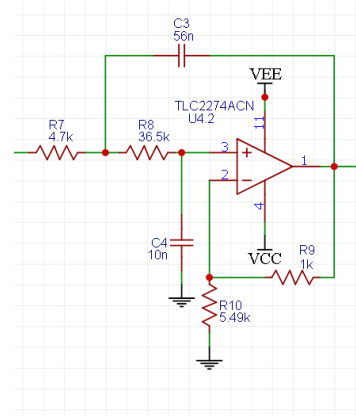
(B) Low pass filter stage, 2nd order Sallen Key with frequency cut off of 513Hz and gain of 1.18

FIGURE 5.2: FilterStages 1 and 2

The second filtering stage was also a 2nd order filter, however this stage was a low pass filter; responsible for removing high frequency components associated with stochastic noise. This noise was caused by sources such as resistor thermal noise, changing fields, ElectroMagnetic Interference (EMI), and some of the gradient noise from the MRI and from the cold-head.

The third stage was a multiple feedback low pass filter and the fourth was another Sallen Key low pass filter. With a fifth and final filter being low pass filters, identical to stages 2 and 4, to further improve the noise rejection characteristics.This creates a higher order filter resulting in sharper bandwidth cutoffs
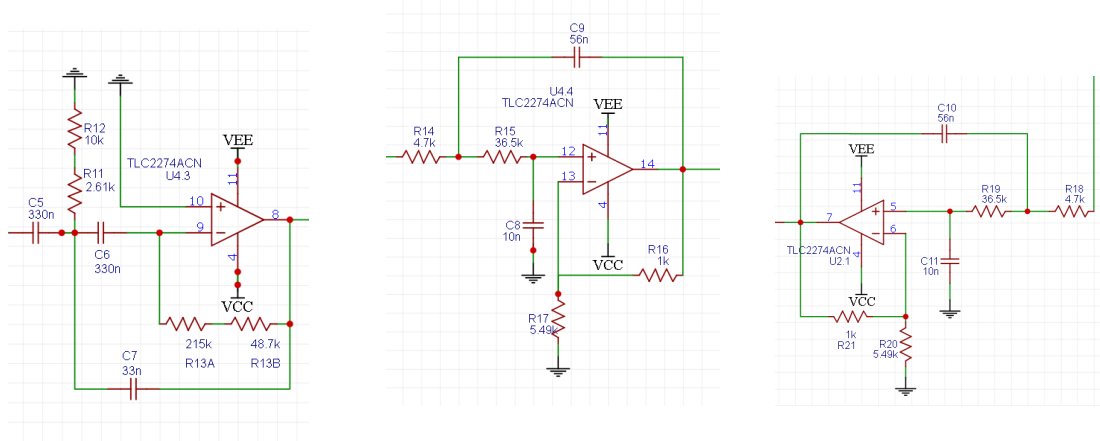
(A) High pass filter stage, 2nd order Multiple Feedback with frequency cut off of 26Hz and gain of 1

(B) Low pass filter stage, 2nd order Sallen Key with frequency cut off of 513Hz and gain of 1.18

(C) Low pass filter stage, 2nd order Sallen Key with frequency cut off of 513Hz and gain of 1.18

FIGURE 5.3: FilterStages 3,4, and 5

and higher rejection of unwanted frequencies.

Variable Gain Amplifier

The variable gain amplifier was the final stage before the ADC, it was responsible for a final bout of signal amplification however runs the risk of clipping to the supply rails if the gain is too large.

It was designed as an inverting amplifier with a manually switchable resistor bank to determine the gain, gain settings are given in Table 5.1.

Power Supply

The power for the system is provided by the Analog Discovery Kit 2, a multi-purpose electronics tool by Agilent. The device was used in DC output mode to provide a power supply of differential +-5V to the positive and negative external
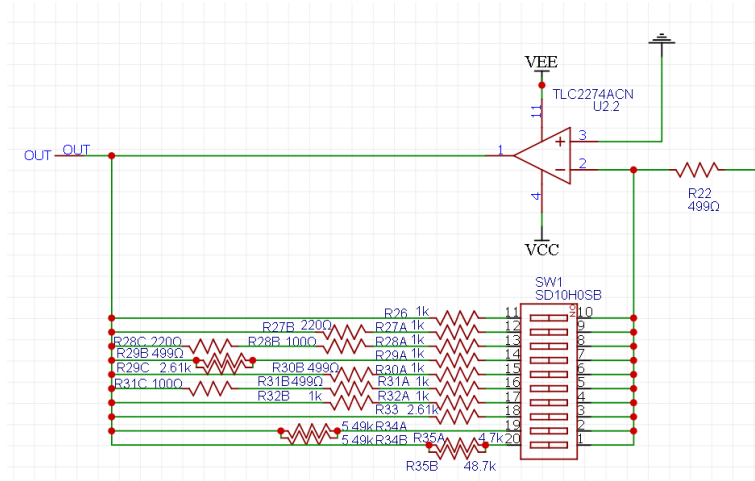
FIGURE 5.4: Variable Gain Amplifier: Dip switch programmable gain, 10 different gain values. Adapting gain to adapt to participant EMG and gradient artifact amplitudes.

TABLE 5.1: Variable Gain Stages

Position	Gain
1	2.00
2	2.44
3	2.65
4	2.85
5	3.00
6	3.20
7	4.00
8	5.23
9	5.51
10	8.57

rails, shown in Figure 5.6. However this does not provide the necessary ground reference voltage. This was remedied with a floating ground generator.

This was comprised of a simple resistor voltage divider to create a voltage point of 0V between the two power rails. This divider was kept more stable from power supply noise with smoothing capacitors between each rail and the generated floating ground. This was then buffered with a unity gain buffer so
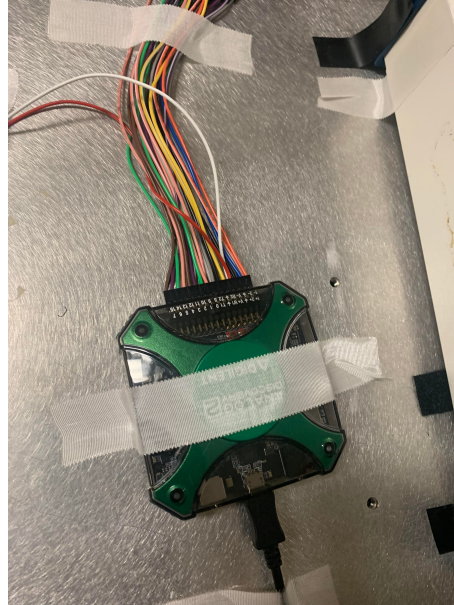
FIGURE 5.5: Analog Discovery 2 by Agilent: Connected to host computer via USB and supply dual power rail to amplifier circuitry.

that the voltage divider was not effected by the amplification circuit which would change the reference voltage as the load changes.
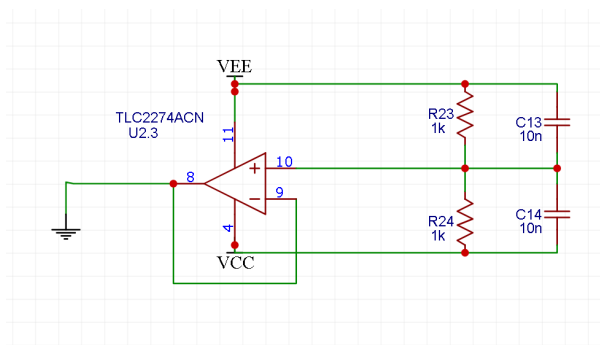
FIGURE 5.6: Virtual Ground Circuitry: Take input dual power rail supply and output midpoint. Generate ground between the ±5V rails.

TABLE 5.2: Analog to Digital Converter Specifications

Model	NI USB-6221
Analog Inputs	8
Analog Output	2
Sampling Rate	250 kSps
Digital I/O	8

Analog to Digital Converter

ADC was a NI USB-6221 by National Instruments. The technical specifications are shown in Table 5.2.

The data was acquired using a custom interface through LabView by National Instruments. Sampling was done at 5kHZ. This sampling frequency was determined as it sufficiently samples the frequency bandwidth of the EMG signal. The highest frequency component of the EMG power spectrum is 500Hz as per the Nyquist-Shannon criterion, a 1kHz sampling rate is sufficient to avoid aliasing but a 5kHz will be able to better recreate the signal(Boxtel et al. 1998).

5.2.1.1.1 Construction

The EMG was assembled within the IRC. Using both a soldering iron and hot air soldering station. The components were assembled in order of the signal path; this was done so that each stage could be tested one by one.

Verification

The EMG system was verified outside of the MR scanner, attached to the the biceps muscle of the upper limb. This was done as a preliminary step to ensure that the prototype worked as intended as well as for the final device after assembled on a

FIGURE 5.7: National Instruments USB-6221 Analog to Digital Converter: Convert analog output from amplifier into 16-bit digital signal computer logging.
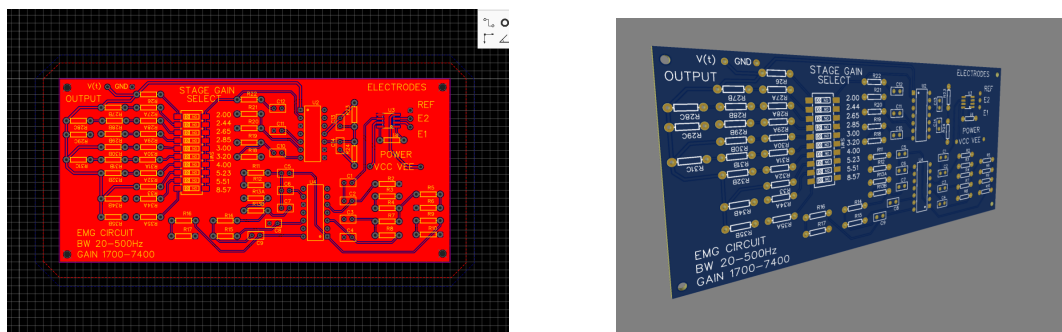
FIGURE 5.8: PCB Renders: Models of deisgned PCB prior to manufacturing.

PCB. This was then repeated within the MR room with and without the scanner acquiring an image. Both scenarios showed the EMG working as intended.
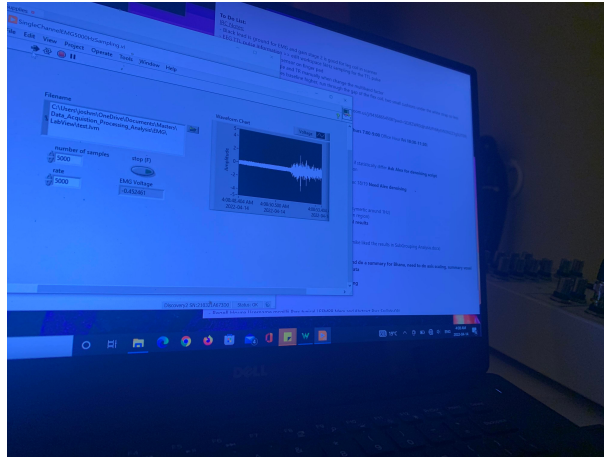
FIGURE 5.9: Testing of EMG Prior to Beginning Scan: Verifying the that the EMG system is able to record the EMG signal within the MR scanning room.

Usage Precautions

When in use with the MR scanner, a number of precautions must be observed for optimal performance and safety of the EMG system. The first is to avoid any looping of the lead cables, this can act as an inductive antenna leading to unaccounted currents. When in the scanning room, the cable should come out along the field lines of the bore until passing the 5 Gauss line denoted on the ground to minimize the induced noise along the length of the cable. Another cable precaution to be taken into account is the power supply of the ADC. The EMG cable should be kept away from the power cable of the ADC, as it uses a Switch Mode Power Supplies (SMPS) that achieves its efficiency by chopping up the power from the wall. As efficient as it is, it generates a lot of chopping noise that can couple to the EMG cable and induce very significant noise.

5.2.1.2   EMG Filtering

A major hurdle in multimodal MR imaging is the noise induced into other modalities. The magnetic field changes induce signals in electrodes and cables. EMG is not excluded from this effect, the EMG signal is swamped by the induced noise. This is seen in Figure 5.10 For the recorded EMG data to be usable, it must first be filtered to remove the gradient induced artifact.

Wavelet Denoising and Impulse Train Filtering

The filtering of the EMG data in order to remove the gradient noise in addition to other sources of noise was done with a custom filtering pipeline. The figures shown below are of surface EMG recordings of the tibialis anterior muscle during a block exercise paradigm of alternating 30 second blocks of rest and plantar flexion.
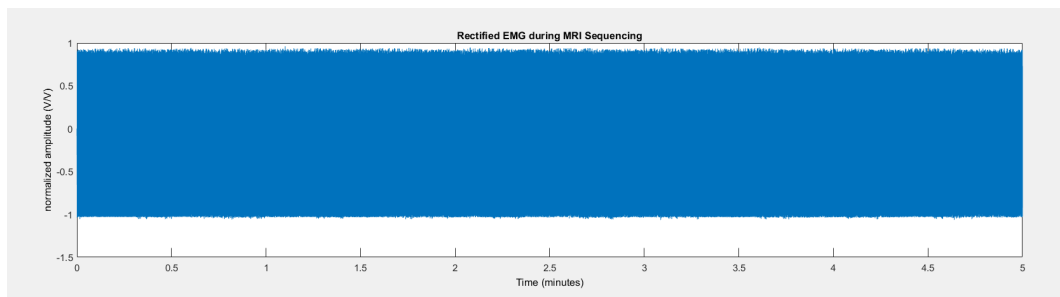
FIGURE 5.10: Raw EMG Signal: Waveform of the EMG signal corrupted with MR gradient artifact, prior to filtering processing.

This was built on prior work within the lab and the work done by Ganesh et al. (Ganesh et al. 2007). The technique takes advantage of the repetitive TR of the scan and the consistency of the gradient artifact. Since the induced artifact was self-similar and repeating, it can be modelled as a signal that had a characteristic waveform and was repeating at some interval τ_R. It is known that for a given
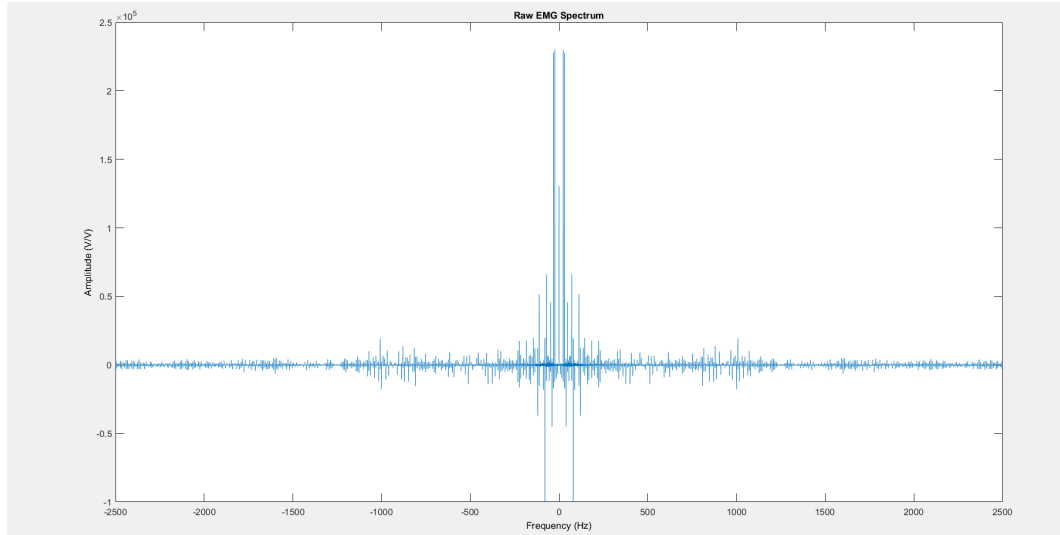
FIGURE 5.11: Raw EMG Spectrum: Frequency spectrum of EMG signal, MR gradient artifact seen as impulse train of 4Hz spacing with silhouette of Sinc function.

continuous temporal waveform, it will have a continuous frequency representation. If that same waveform is then repeated periodically, the frequency representation will then become a discrete impulse train with a matching envelope to that of the continuous form. The property of interest is: the frequency spacing, f_R of the impulse train is consistent and reciprocal to τ_R. This property is simply explained as the resulting convolution of the original waveform with a impulse train.

Applying this to gradient noise leads to an interesting insight, the τ_R was equal to the TR of the scanning sequence. Meaning the spacing of impulse train, otherwise known as a comb function, was the MR scanning frequency. As done by Ganesh et al., a comb filter tuned to $\frac{1}{TR}$ can then be used to remove the gradient noise. The method used in this thesis used a power line noise removal tool, the intended purpose of which was to remove 50 and 60Hz noise and their harmonics, caused by the power supply. In this case however, for a TR of 250ms, a frequency of 4Hz was used as the spacing of the impulse train. Figure 5.11, shows this 4Hz

spacing throughout the bandwidth of the spectrum.

This is shown in the Figures 5.12 and 5.13. This greatly reduces the gradient noise, the harmonic filtering is repeated for 60Hz as the power supply for the ADC induces large amounts of noise into the signal.
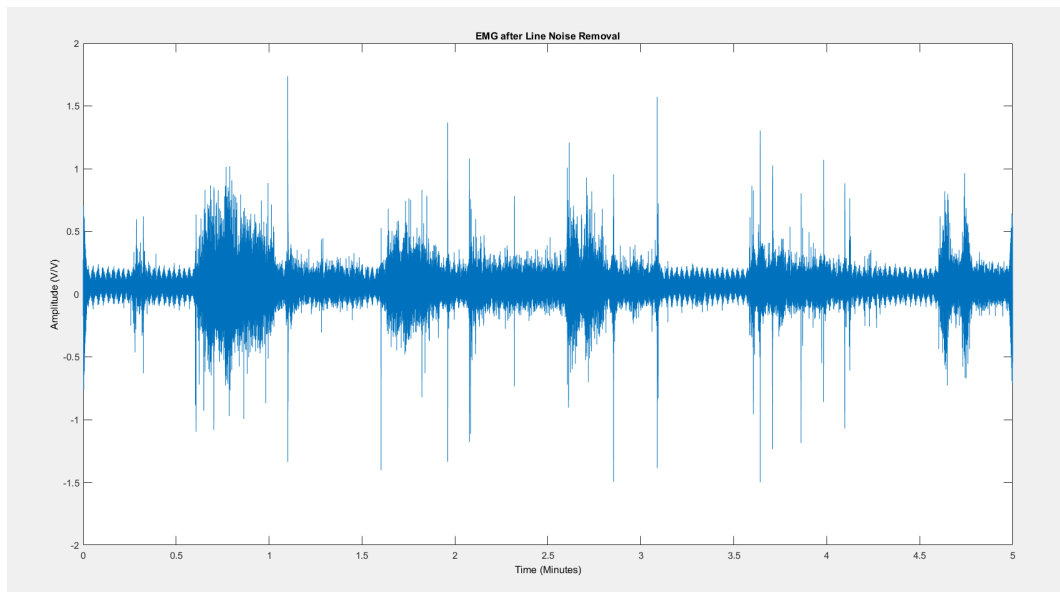
FIGURE 5.12: EMG After Line Removal: Resultant EMG waveform after dampening 4Hz harmonics from the spectrum. The harmonics of the of the 4Hz initial impulse span the entirety of the spectrum.

The remaining signal was a mix of the desired EMG signal and unwanted noise sources such as; motion, cold head noise, and left over gradient noise. This was tackled using wavelet denoising. The chosen wavelet is the Bior6.8 wavelet, see Figure 5.14, this was chosen due to the topological similarities to the MUAP waveform.

This made it a good fit for extracting the desired EMG waveform while rejecting the background noise. 64 scales were generated with only the higher 48 used, this works as a high pass filter, removing noises sources such as motion. Figure 5.15
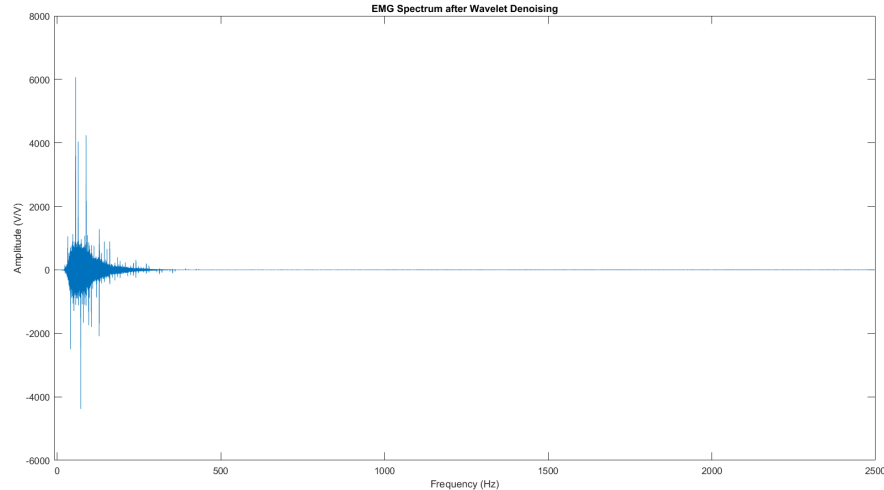
FIGURE 5.13: EMG Spectrum After Line Removal: EMG spectrum post 4Hz harmonic suppression. 4Hz is the frequency corresponding to the repetition time of 250ms. The artifact spanning the spectrum being suppressed results in suppression of the artifact.

shows the EMG after the wavelet denoising. The output still contained noise from multiple sources. During the rest portions of the exercise paradigm, the subject's foot was resting against a pedal, consequentially there may be postural activation of the tibialis anterior raising the baseline of the resting signal this can be seen in Figure 5.21. The signal was then filtered with a digital Finite Impulse Response(FIR) bandpass filter of order 500. The cutoff frequencies of the filter being 20Hz and 500Hz, the output of which is shown in Figures 5.16 and 5.17, all frequency components outside of the frequency band of interest have been removed.

The Teager-Kaiser Energy Operator (TKEO) was calculated for the signal, making it easier to determine the onset and offset of contraction. Finally the filtered signal was downsampled, using a linear interpolation, to match the time sampling of the mBOLD data. The downsampling was performed because the processing pipeline requires that the EMG signal match the time span and number
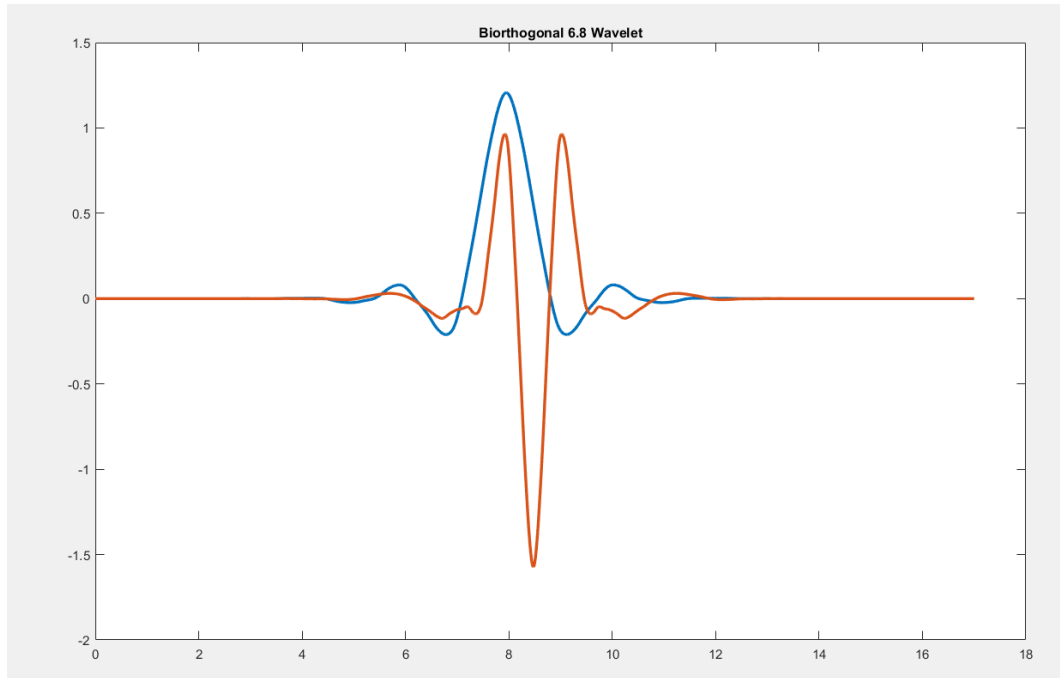
FIGURE 5.14: Bior6.8 Wavelet: Wavelet topology resembling that of the fundamental waveform of the EMG signal. Corresponding to the motor unit action potential sent from the motor unit nerve to the muscle. The blue line representing the mother biorthogonal 6.8 wavelet and the red line representing the scaling function.

of samples as the mBOLD data.

The greatest strength of this methodology is that it is widely applicable to MR scanning with a sensor. This is because the requirements are that the gradient noise be a repetitive and self similar, and that the TR is known. A prior model for the waveform of the MR noise is not required. Figure 5.21 hows the ability of the process to recover the EMG signal that can then be further processed with conventional EMG techniques. Another large benefit of this technique, as Ganesh et al. showed in their work, is its ability to be used real time, as data is streaming in, a comb filter can be applied via hardware digital signal processing. Meaning that it can be used to analyze signal quality during scanning and direct subjects
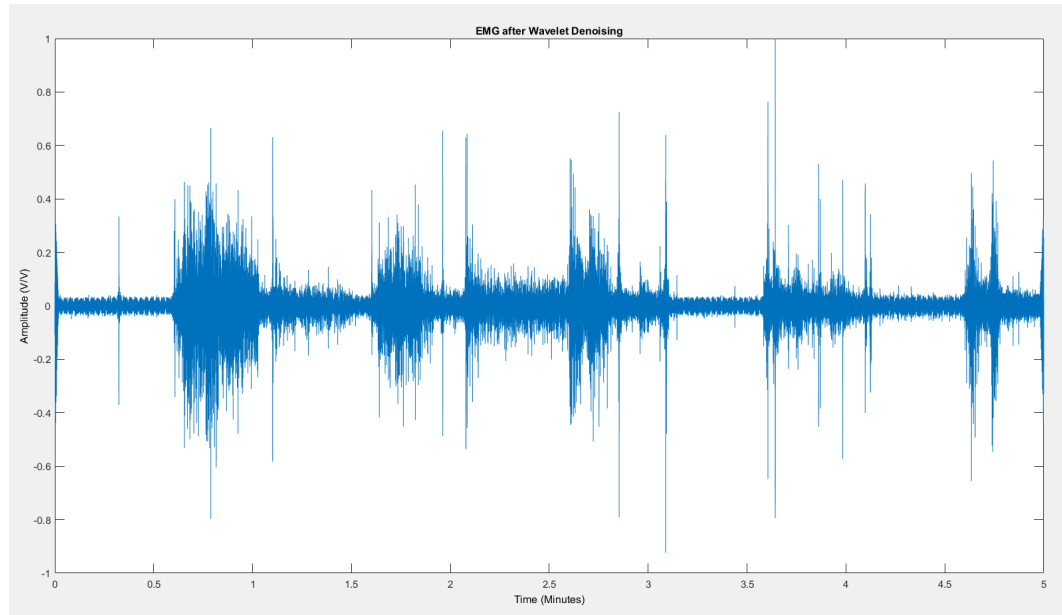
FIGURE 5.15: EMG After Wavelet Denoising: Waveform of the EMG signal after wavelet denoising. High pass filtering behaviour of wavelet denoising as lower scales are omitted. 64 scales were generated, signal reconstructed using only top 48 scales. Omission of lower wavelet scale removes motion artifacts and low frequency noise.

accordingly(Ganesh et al. 2007).

5.3 Scanning Setup

The scanning setup begins with the participant changing into MR compatible gowns. They were then asked to rest in the supine position, this was done to normalize blood flow in the leg prior to scanning. This rest lasts for 30 minutes prior to scanning begin. During the rest period, the leg was prepped for EMG acquisition.
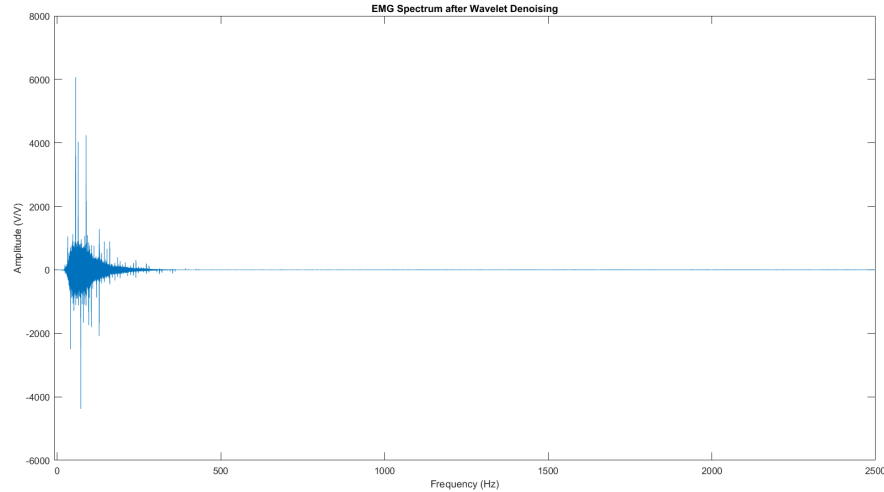
FIGURE 5.16: EMG Spectrum After Wavelet Denoising: Signal frequency spectrum after wavelet denoising. High pass filtering behaviour of wavelet denoising as lower scales are omitted. 64 scales were generated, signal reconstructed using only top 48 scales. Omission of lower wavelet scale removes motion artifacts and low frequency noise.

5.3.1 EMG Preparation

The first step in the EMG preparation was to clean the region with an AllKare Protective Barrier wipe by ConvaTec. Subsequently, the area was abraded using NuPrep cream and a towelette. The abrasion was done in order to remove the outermost layer of skin so as to reduce the impedance seen by the EMG amplifier. The participant was then asked to move their ankle in plantar- and dorsi- flexion to locate the tibialis anterior muscle. The three surface EMG electrodes are then placed. The first signal electrode was placed over the muscle belly, the second 7.0cm distal to the first towards the insertion of the muscle.

The third reference electrode, was placed on the tibia, electrodes along the 3.5cm midline between the other electrodes. Tape was then used to reinforce
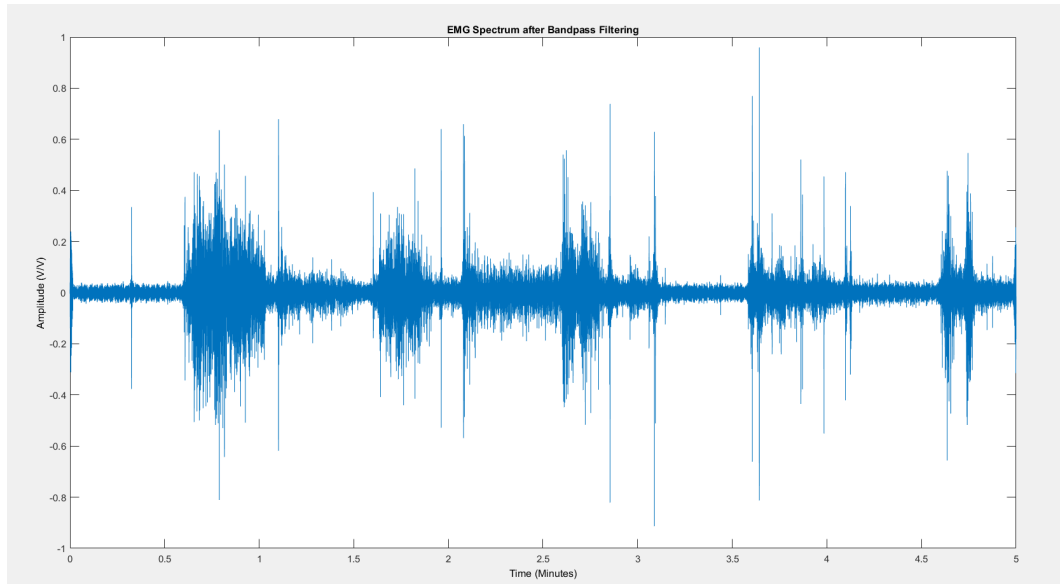
FIGURE 5.17: EMG After BPF: Digital finite impulse response band pass filter with order 500 implemented with frequency cut offs of 20Hz and 500Hz to match bandwidth of the EMG signal. Band pass filtering removes high frequency noise from signal.
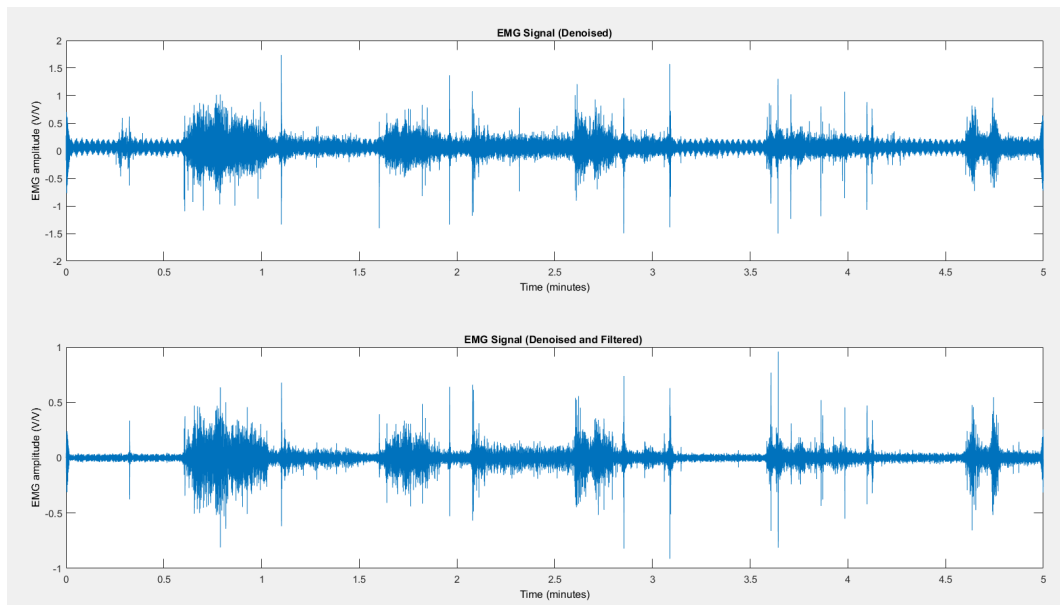
FIGURE 5.18: EMG Before and After Denoising: Impact of digital band pass filtering and wavelet denoising of the signal, increasing quality of signal at baseline thus increasing SNR.
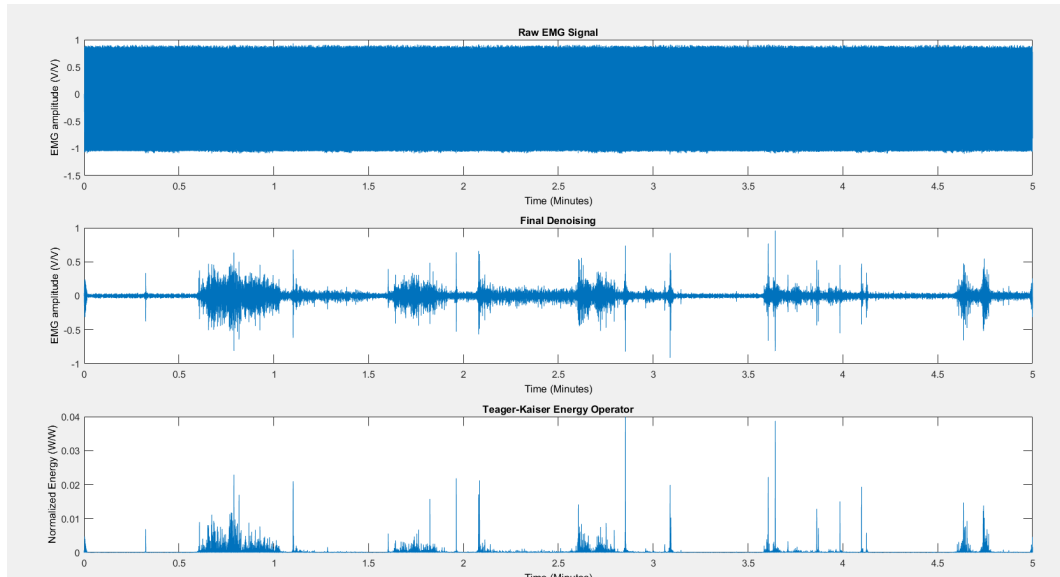
FIGURE 5.19: EMG Signal Raw(top), After Line Removal(middle), and Energy Operator output(bottom). Highlighting the ability of the proposed filtering technique to remove gradient noise and condition EMG signal. Done without modelling the gradient artifact with only TR known.

the adhesion of the electrodes to the leg. When developing the protocol it was found that the adhesive on the electrodes was not sufficient to keep the electrodes attached throughout the entirety of the scanning procedure, thus necessitating the tape.

5.3.2 Determination of Maximal Voluntary Contraction (MVC)

In order to standardize foot flexion, a percentage of the participant's Maximum Voluntary Contraction (MVC) was used. In order to achieve this, a wooden mechanism was constructed by Joshua E. McGillivray. This provides resistance for both dorsi- and plantar- flexion for both legs. The data for this thesis were collected with only plantar-flexion of the right leg. The handcrafted device sports boxes that are for adding weights, in this case lead scuba diving weights, to add resistance
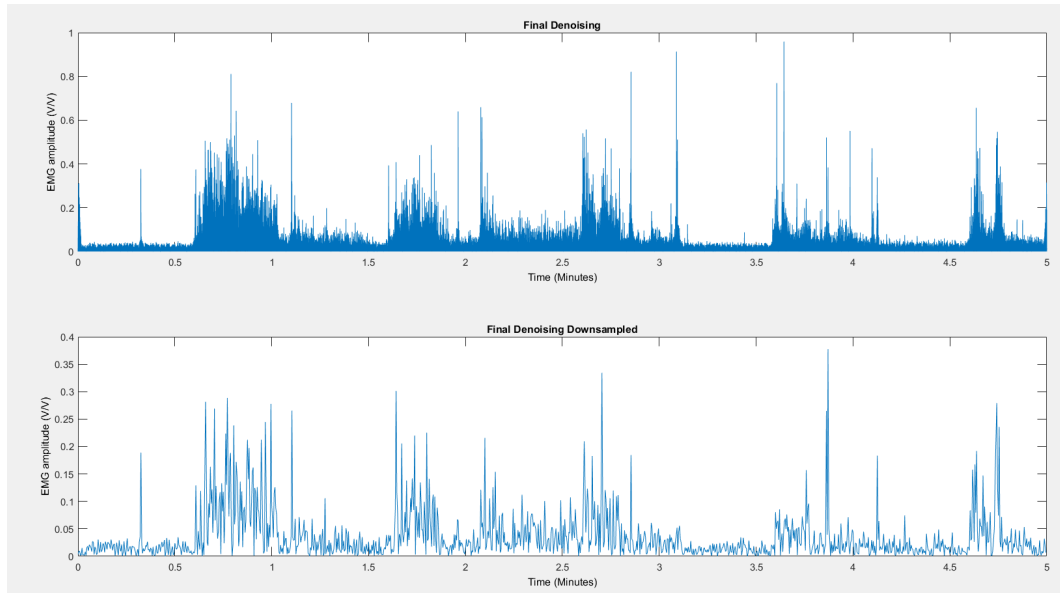
FIGURE 5.20: EMG Downsampling: The resultant EMG signal is of too high sampling frequency to be matched to the mBOLD signal. Interpolating the 5000Hz EMG signal down(top) to the 4Hz signal(bottom) to match the fMRI sampling rate.

to the ankle flexion. The amount of weight is determined by measuring the MVC of the participant, with 40% used for the scanning protocol. It was designed to fit onto the bed of the MRI and slot into the notches found under the bed covers. The top half of then registers on top of the bottom half with alignment dowels. The right side weight box was added followed by the required lead weights for the participants. The left side box was not added, instead the Flex Coil used comes in two parts; the coil and the and the transceiver. The transceiver was placed in the spot of the left side box, this was done as it was the only way to have the coil along the calf and still be able to plug the transceiver into the MR scanner.
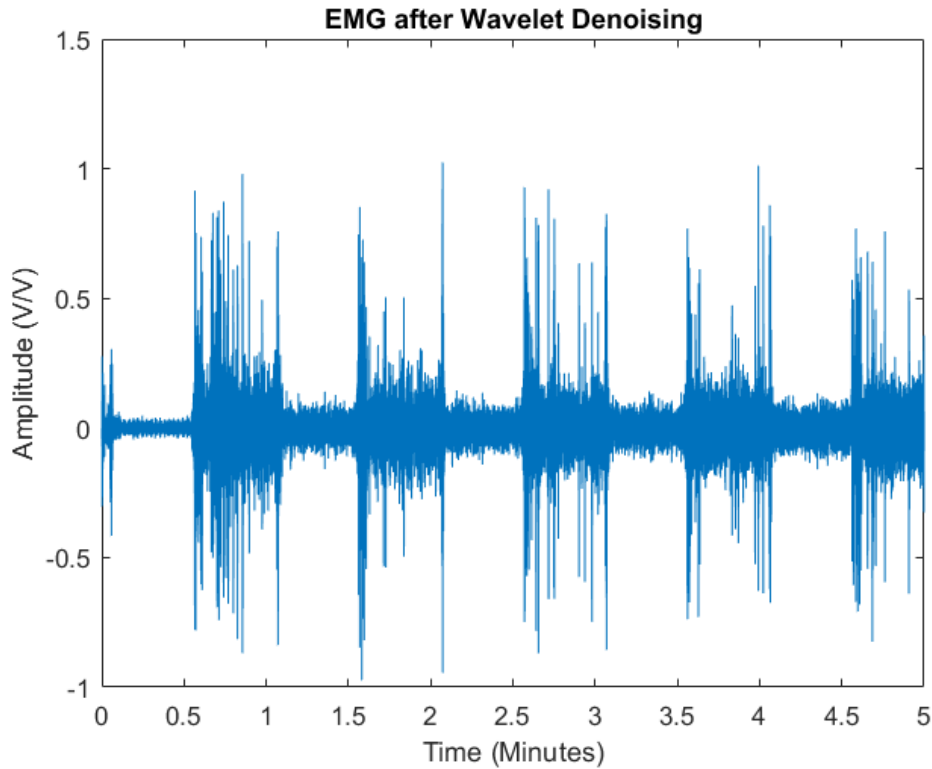
FIGURE 5.21: Cleaned EMG Signal: Signal outputting after performing the filtering pipeline. Showing the ability of the pipeline to remove gradient artifact without template of artifact waveform. The cleaned signal is ready to be processed with traditional EMG techniques now that gradient noise has been removed.

5.4 Scanning Protocol

The scanning protocol contained sequences not relevant to this investigation but for others, only those pertinent to this investigation are mentioned below. Sequences omitted also include locator scans at start of scanning session, meant for alignment of ROI for the subsequent scans.

(A) Spacing between readout electrodes: Electrodes placed 7cm apart from edge to edge, distance maintained across all subjects.

(B) All 3 EMG electrodes placed on participant: Reference electrode placed superficial to tibia.

FIGURE 5.22: Placement of EMG electrodes

FIGURE 5.23: Skin Preparation Products: Area wiped first by AllKare wipe, then NuPrep applied to clean towel which is then used to abrade the skin, the electrodes were then adhered.

5.4.1 Anatomical Scan

The anatomical scan is a Proton Density scan that creates a high resolution image that was used to outline the anatomy, specifically to determine the bounds of muscles and their fascia. This was important to place ROIs for the rest of the scan

FIGURE 5.24: Subject Leg While Attaching Electrode Leads: Electrodes connected to leads with tape restraining movement of connections. Flex coil padded to distance leg slightly from coil surface. Leg propped up with padding to properly position leg within the lab designed MRI compatible ergometer. Ergometer has been loaded with weight corresponding to subject's 40% MVC.

and for binary masks of the muscles used in the data analysis.

The anatomical scan has the parameters outlined below:

TABLE 5.3: Anatomical Scan Parameters

Sequence	Fat Suppressed Proton Density Weighted
Slices	15
Slice Size	512x512
Voxel Size	0.625mmx0.625mmx4mm
Slice Thickness	4mm
Slice Spacing	1mm
TE	30ms
TR	3000ms
Flipping Anlge	111 °
Time	4:51
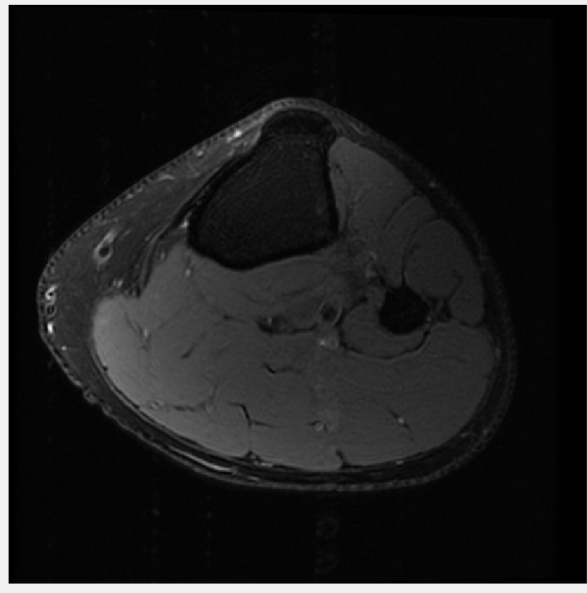
FIGURE 5.25: Anatomical Scan of Leg: Cross sectional view of calf, region encapsulating the electrodes. Fat Suppressed Proton Density scan, used to determine separation of muscles within the leg and functional slice placement. Slices for functional scan are selected based on muscle separation seen in anatomical scan.

5.4.2 mBOLD Scans

The muscle BOLD scans are done across two slices, encompassing the entirety of the cross section of the leg. The slices are chosen to be between the top electrode and the reference electrode. The scan was also repeated with a saturation band, both done at rest and with an exercise paradigm. The parameters of the scan feature a TE of 35 ms, TR of 110 ms, across 2 slices. The full parameter set is shown in Table 5.4. The resting state mBOLD scans lasted 4:29 minutes whereas the exercise scans lasted 8:50 minutes. During the exercise paradigm, the subjects were asked to plantar flex within woody for periods of 66 seconds. The scan was started at rest, the subject was asked to switch states from rest to flexion or vice versa. This timeline generated the ground truth activation vector later used in the

TABLE 5.4: Resting BOLD Scan Parameters: Sequence parameters of standalone mBOLD scan.

Sequence	BOLD (EPI)
Slices	2
Slice Size	64x64
Voxel Size	2.5mmx2.5mmx10mm
Slice Thickness	10mm
Slice Spacing	0mm
TE	35ms
TR	110ms
Flipping Anlge	70 °
Time	4:29 or 8:50

analysis as seen in Figure 7.1.

5.4.2.1 Saturation Band Impact

A 50mm saturation band superior to the slices of interest was added to suppress the impacts of arterial blood flow into the leg. The effect of the blood flow is hyper intensities in the acquired mBOLD images. The difference in the scans is pronounced, the saturation bands heavily reduced ghosting artifacts that were present in some participants. The severity of the artifact was participant dependent. For those that were scanned on multiple occasions, the effect varied scan to scan. This artifact being reduced by the addition of saturation bands was also observed by Robinson et al. as early as 1998, stating: "... SE[Spin Echo] images showed small intense features that were eliminated by application of outer slice saturation bands, eliminate the effect of in-flow signal enhancements." (Robinson et al. 1998). They further went on to perform histological testing showing the effects were caused by large blood vessel (Robinson et al. 1998). Figure 5.26 shows the placement of the saturation band in the protocol, a 50mm saturation band

was placed directly above the most superior slice of the scan. This was done to reduce the impact of the in-flow effects on the image.
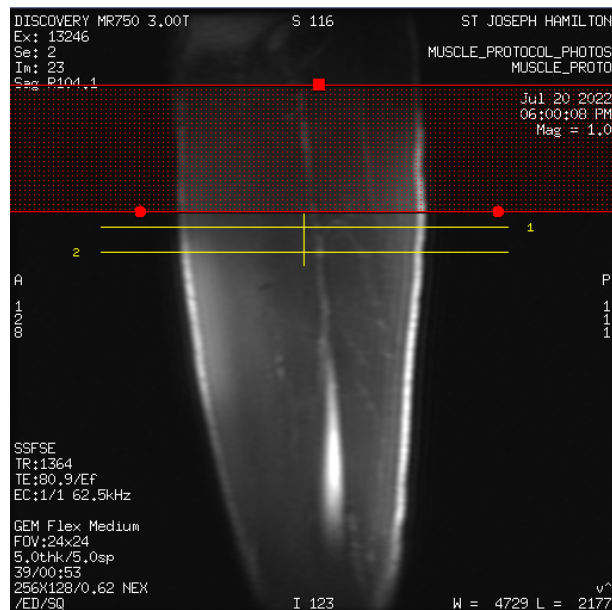
FIGURE 5.26: Placement of the Saturation Band: 50mm band placed superior to slices to reduce impact of inflowing blood. Slice selection shown overlaid locator scan images, slices placed between EMG electrodes with the saturation band placed afterwards.

5.4.3 Concurrent EMG/fMRI

The next scan performed was another exercise paradigm that recorded both EMG and mBOLD data from the participant with scan parameters shown in Table 5.5. The paradigm differed from the previous in the length of the exercise blocks, 30 seconds of alternating rest and plantar flexion, starting at rest similarly to the mBOLD standalone scans. The mBOLD scan was first prepped and shimming was performed. Once that was over, then both the mBOLD and EMG begin recording at approximately the same time. This was done by having one person

TABLE 5.5: EMG BOLD Scan Parameters: Parameters of BOLD sequence for concurrent mBOLD and EMG acquisition. Exercise paradigm changed to 30 second blocks of contraction and rest.

Sequence	BOLD (EPI)
Slices	2
Slice Size	64x64
Voxel Size	2.5mmx2.5mmx10mm
Slice Thickness	10mm
Slice Spacing	0mm
TE	29ms
TR	250ms
Flip Angle	70 °
Time	5:05

in the MR room, while wearing hearing protection, start the LabView script while coordinating with the person operating the MR scanner.

Chapter 6

Data Analysis

6.1 Pre-Processing

The pre-processing of the data was done in FSL. Motion correction was performed on the functional data to compensate for the movement of subjects throughout the scan and during contraction. Smoothing was not performed so that complexity components pertinent to the fractility measure were not removed.

6.1.1 Hardware Specifications

The computation and analysis of the data was performed on a computer with the specifications shown in Table 6.1.

TABLE 6.1: Computer Specifications

Model	HP Spectre x360 15-bl0XX
Processor	Inter(R) Core(TM) i7-7500U CPU @ 2.70-2.90GHz
RAM	16 GB DDR4
GPU	Intel(R) HD Graphics 620 & NVIDIA GeForce 940MX

6.1.2 Masking

For each of the participants' scans, a binary mask was drawn for each of the muscles of interest. This was done by using the high resolution anatomical scans as reference to create the masks with the same resolution as the mBOLD images. The initial masks, seen in Figure 6.2, were created by Joshua McGillivray.

In the process of making the masks over the mBOLD scans, seen in Figure 6.1, vasculature and fascia were avoided. Another factor considered when generating the masks was the angle of the leg. Due to the slice thickness of the functional scans being 10mm, depending on the angle of the leg, the position of the muscle fibres can cross voxel boundaries. This results in voxel-voxel cross talk due to the difference between the laboratory frame and the leg orientation.
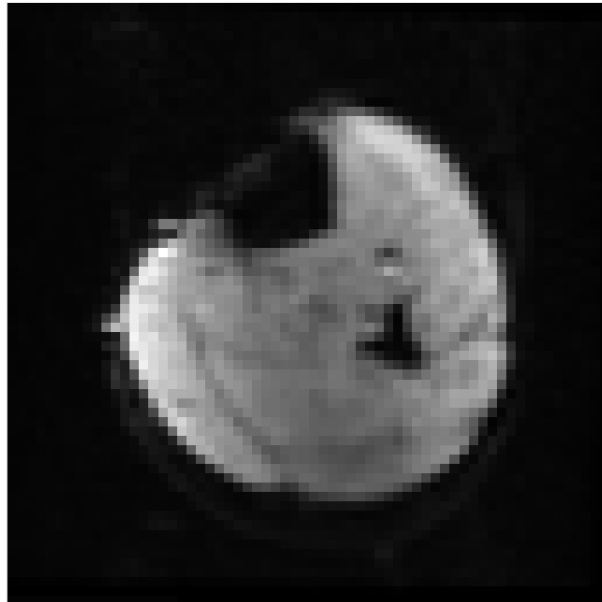
FIGURE 6.1: Functional mBOLD Scan: Image acquired during mBOLD sequence. The functional data is extracted from the image concatenated over time.

(A) Gastrocnemious Mask

(B) Soleus Mask

(C) Tibialis Anterior Mask
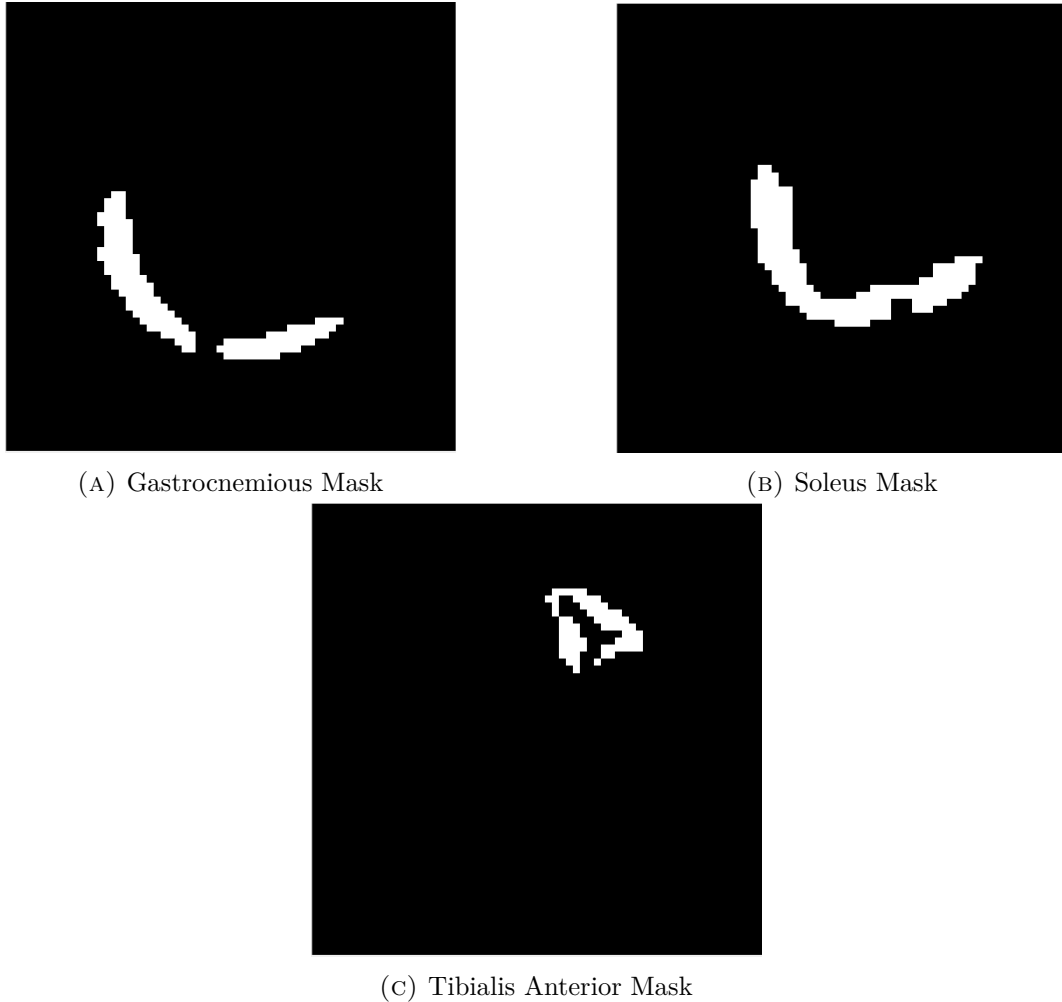
FIGURE 6.2: mBOLD Muscle Masks: The binary masks outline the muscles of interest; gastrocnemius, soleus, and tibialis anterior. The masks are used in the analysis to extract only information from the intended muscle. Masks were created using high resolution anatomical images as reference with resolution of the masks matching the 64x64 size of the functional scans. The masks were created using FSL and Matlab to pixel by pixel match the muscle groups while also avoiding blood vessels, fascia, and partial volume effects. Masks were made smaller than bounds of the muscles to compensate for movement during contration.

6.2 Generated Graph Signal

The masks were then used to create a point cloud of nodes, the process of creating the nodes is shown in Figure 6.3. There was an equal number of nodes created

within each muscle. These were created using the binary masks created specifically for each subject, the nodes were randomly seeded within the bounds of each mask without any seeds sharing the same location. This generated point cloud was the graph that signals were superimposed onto. The time series data of the voxel corresponding to each node was then registered onto those nodes. Thresholding of the time signal was performed so that any voxels that showed no activation were rejected and another sampling was performed. Figure 6.3 shows the selected points overlaying the mBOLD image in the top left. These same points are shown in a three dimensional space, the graph space, in the top right image. The time series response of a single voxel is also shown. Overall the figure shows the generation of the graph signal from the mBOLD data.
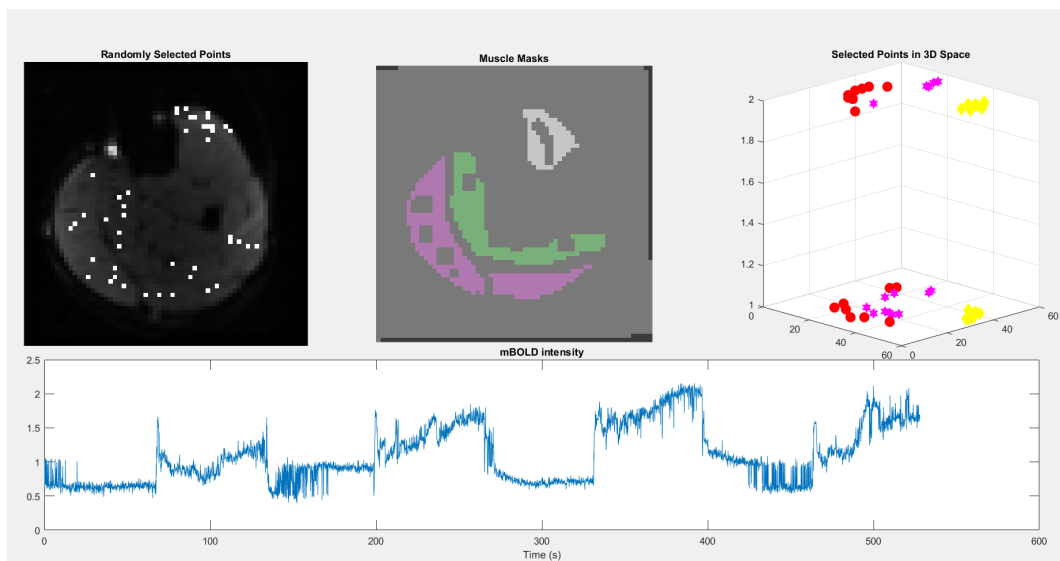
FIGURE 6.3: Point Cloud Generation: Visualization of functional scan with selected points overlaid(top left), the three muscle masks used to select points within(top center), 3 dimensional space with representation of placed nodes(top right), and the normalized time series data from the last placed node(bottom).

6.3 Spatio-Time-Frequency Transformation

The data was converted into a sparse spatial representation via the node sub-sampling. The time-series data of the nodes was then transformed using the Stockwell Transform, more specifically the Discrete Orthogonal Stockwell Transform (DOST)(*FFT-fast S-transforms* 2022; Battisti and Riba 2016). This generated a Graph Signal that contained information in three domains; spatial, temporal, and frequency. The representation in this case was encoded in time and frequency for each node position. The frequency-time charts are then correlated along time between each node pair; resulting in a coherence vector over time for each edge. Coherence being the correlation in the frequency domain, further defined as the measure of the covariance between two signals as a function of frequency. This was encoded onto the edges of the graph to complete the coherence dimension of the graph signal.

6.4 Feature Extraction

On top of coherence, other features can be extracted between the nodes and used to fill another dimension of the graph signal. In this case, the fractal dimension also known as the fractility, of a signal was used. For this to match with the size of the coherence layer, the signal was windowed and the fractility was calculated for each window(Sumanth 2022), thus creating the second feature layer for the graph, a time-varying fractility measure between nodes. This is expandable for multiple other features, this investigation focused on the coherence and temporal fractility. Figures 6.5 and 6.6 show constructed connectomes for the coherence and fractility
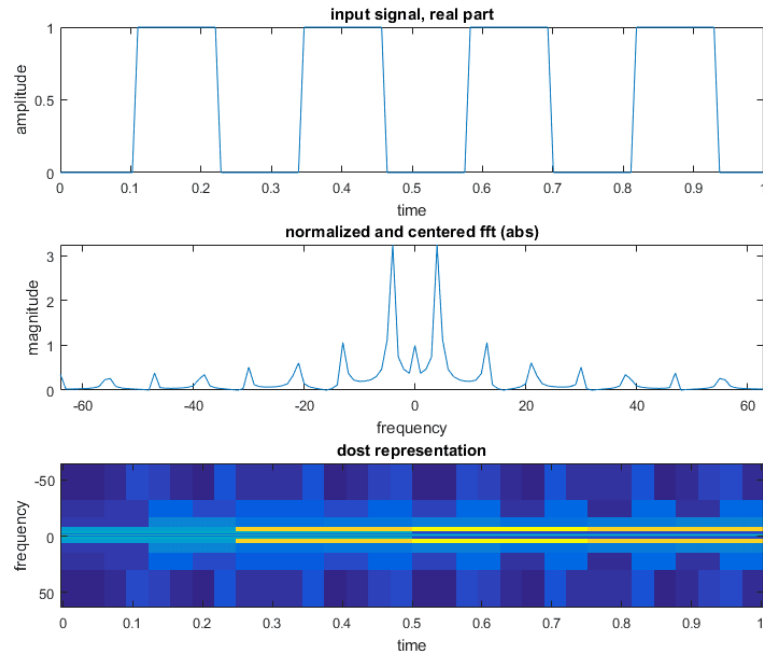
FIGURE 6.4: Activation Function Transformation: Visualization of times series activation function(top), frequency spectrum of activation function(middle), and time-frequency representation of activation function(bottom).

domains respectively. The connectomes display the edge metrics as dotted lines between nodes. The greater the value of the metric, the thicker the lines. The colours of the lines denote whether the line represents a positive or negative value. In Figure 6.5, green edges stand for positive coherences between two nodes at that time point, likewise for red edges and negative coherences. For fractility, the differences between fractility measures were used. To highlight the edges of greatest strength, the connectomes in the figures were thresholded. The same goes for the node radii and colours; the greater the correlation of the node to the activation function. Meanwhile the colour represents the sign of the correlation magnitude, again red for negative and green for positive. The edge connections can also be

shown as an adjacency matrix; these are also presented in the figures. As the connection between two hypothetical nodes A and B are isometric, the connection A to B was the same as B to A. Meaning the adjacency matrix was symmetric along the identity axis. This is true for the feature dimensions of coherence and fractility, but may not be the case for others, an an-isometric feature would lead to a non-redundant adjacency matrix.
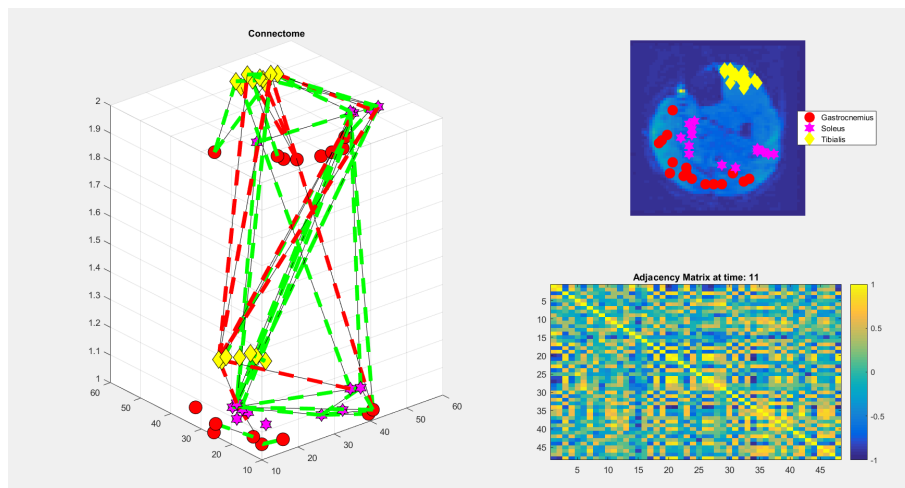
FIGURE 6.5: Constructed Coherence Connectome: Nodes with edge connections thresholded to Coherences above 0.85, edges visualizing coherence magnitude by diameter and sign by colour(left). The node positions in the functional scan(top right) and connectome connections shown as a matrix(bottom right).

6.5 Statistical Analysis

The statistical testing of any data analysis is vital to determining the efficacy of said analysis. Otherwise it becomes a tool without a metric for its use. The standard statistical test is the Analysis of Variance(ANOVA) used to determine if two populations, or more, have equal population means. It is widely used but
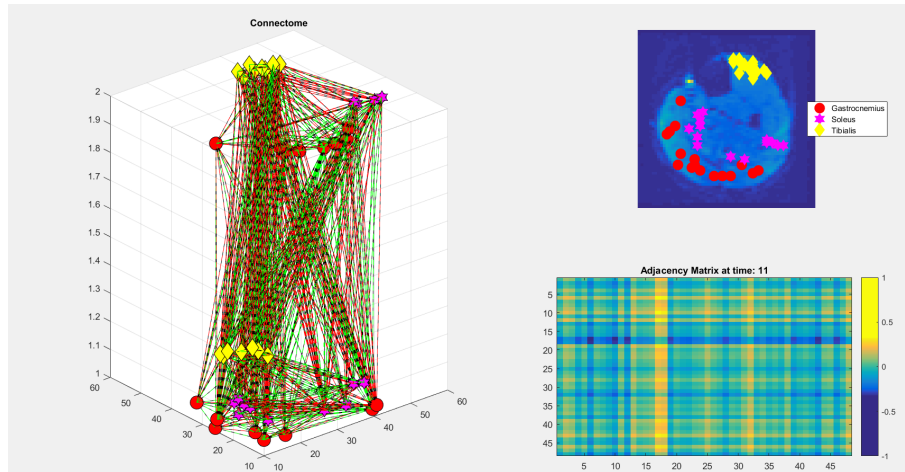
FIGURE 6.6: Constructed Fractality Connectome: Nodes with edge connections thresholded to Fractility values above 0.5, edges visualizing coherence magnitude by diameter and sign by colour(left). The node positions in the functional scan(top right) and connectome connections shown as a matrix(bottom right).

it cannot be used for all analyses as it has underlying assumptions for its use; if a data-set does not meet those assumptions, the test is invalid. The data-set generated in this study, the graph signal, was one for which the ANOVA is not valid. The reasons it is so were multi-fold; the data was not normally distributed, the data was inherently not comprised of independent observations, and an N-way analysis was necessary. Due to these reasons other tests such as the Kruskal-Wallis test, which cannot perform N-way analysis, were also not viable.

6.5.1 Statistical Model

When exploring the possibilities, there were only a few viable options. Possibilities considered include; Multivariate ANOVA(MANOVA), Friedman's Test, Wilcoxon

Signed-Ranked Test, Aligned Rank Transform(ART), and machine learning approaches. The two most viable options were a Generalized Model(GM) or a machine learning approach. This investigation used a Generalized Linear Mixed Effect(GLME) model which is a subset of a Generalized Linear Model(GLM). This allowed for all of the testing needing for graph signals as a GLM can model a non-normal response variable. This is possible as a distribution that is not normal can be represented as an equation with regression coefficients that are linear. This decision was reinforced by referencing the CONN toolbox that uses a similar method to analyze graph signals.

The difference between this methodology of analyzing the data and others tests such as an ANOVA, is that it requires a model to which to fit the data. It is the generated fit that is statistically analyzed. In reality this is not inherently different from the standard analyses as, at their simplest, they measure the ability to fit a data set to a normal distribution.

In the case of the GLME tool built into MATLAB, the model to fit the data was input by the user. This is done by providing the model in Wilkinson notation. This notation models the output as the interaction of inputs and groups with the ability to specifically outline which interactions are to be included and which to be excluded. The equations are written in the form $Responses \sim Predictors + (Random|Groupings)$. The variables responses and predictors are the outputs and inputs that the model is trying to fit. These are represented as a linear combination of individual response and predictor variables. Random variables are those that are random and not predictors with groupings being variables that represent groups within the data. This allows for the tuning of the model to specific applications and variables.

Chapter 7

Results and Discussion

7.1 Results

7.1.0.1 Subjects

A total of 12 subjects were scanned to collect data. However only 10 were used in the final analysis due to the collected data being unusable. Reasons for removing a subject were; intolerable levels of movement during the scans, signal dropout within the leg, or failure to comply with the protocol. Due to such sources of error, certain subjects were removed from the analysis. In this case only two subjects were not used, others were re-scanned to remedy the anomalies.

7.1.1 Analyses

For the two feature dimensions of coherence and fractility, the outputs of the generated models are shown below. The model was fit with user input of an equation based on response, predictor, and grouping variables. Multiple permutations were attempted and shown below.

As the DOST transformation is built on the FFT for efficiency, the data lengths must be a power of 2. For the exercise paradigm, 4800 volumes were acquired meaning 4096 is the largest number that fit within the dataset. Figure 7.1 shows a time truncated series. Meaning 704 volumes had been discarded; these volumes were from the beginning of the acquisition so contractile volumes were preserved.
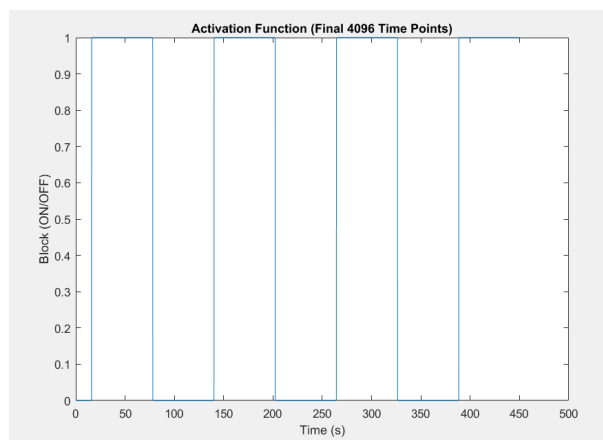
FIGURE 7.1: Activation Function: The ideal activation function of the exercise paradigm corresponding to the time periods subjects were asked to contract and relax. Cropped to a power of 2 to be used with the analysis, as non-power of 2 signal lengths are not compatible with DOST function.

The largest hurdle to processing all of the data was lack of sufficient compute power. The amount of RAM required to run the Stockwell transform time-frequency transformation was mitigated with the GSP subsampling but other steps during analysis were also memory intensive. The two culprits were the edge connection calculations as they were on the order of N^3 with data size and the statistical modelling as it performed multiway analysis of the aggregate data. Steps were taken to minimize the memory needed; however this led to trade-offs, not complete solutions. The trade-offs to the analysis were a limitation to the number of

nodes and time points that could be analyzed. For this investigation those numbers were 18 nodes, 19 in the EMG model, and 1024 as the largest power of 2 that was possible for said number of nodes. This was a drawback of the pipeline that can be improved in future work.

Below are the model formulae of the coherence and fractal models for both the standalone mBOLD and the EMG and mBOLD models. The model output parameters and goodness of fits are seen in Appendix A.

7.1.1.1 Exercise mBOLD Model Equations

7.1.1.1.1 Coherence

```
───────────────── mBOLD Coherence Formula ─────────────────
  Coherence ~ 1 + Time_Point + Edge_Eucl

  + Edge_Dijkstra_C + Node_Type_N:Edge_Type_N

  + (1 | Activation)

  + (1 + Node_Type_N:Edge_Type_N | Subject_Number)
```

Model output shown in Appendix A.1.

7.1.1.1.2 Fractility

```
───────────────── mBOLD Fractal Formula ─────────────────
  Fractal ~ 1 + Time_Point + Edge_Eucl + Edge_Dijkstra_C

  + Node_Type_N:Edge_Type_N

  + (1 | Activation)

  + (1 + Node_Type_N:Edge_Type_N | Subject_Number)
```

Model output shown in Appendix A.2.

7.1.1.2   EMG Results

7.1.1.2.1   Coherence

```
───────────────────── EMG Coherence Formula ─────────────────────
 Coherence ~ 1 + Time_Point + Edge_Eucl + Edge_Dijkstra_C

   + Node_Type_N:Edge_Type_N:EMG

   + (1 | Activation)

   + (1 + Node_Type_N:Edge_Type_N:EMG | Subject_Number )
```

Model output shown in Appendix A.3

7.1.1.2.2   Fractility

```
─────────────────────── EMG Fractal Formula ───────────────────────
 Fractal ~ 1 + Time_Point + Edge_Eucl + Edge_Dijkstra_C

   + Node_Type_N:Edge_Type_N:EMG

   + (1 | Activation)

   + (1 + Node_Type_N:Edge_Type_N:EMG | Subject_Number)
```

Model output shown in Appendix A.4

7.2   Discussion

7.2.1   Comparisons

Exercise mBOLD

When comparing the coherence and fractility models, the feature better fit was evident when contrasting the significance of fit values. The two models are shown

in Appendices A.1 and A.2. The coherence model boasts a statistically significant value of 1.3245×10^{-05} whereas the fractility model had a non-significant value of 0.06466. This shows a drastic difference in fit between the two models suggests that the coherence dimension of the graph is a better metric to use in modelling the activation of the leg. It can be said that the fractility measure is close to significant, nearly missing the 5% significance mark. This may indicate that the measure is better omitted in the analysis to speed up analysis and reduce size of the data.

EMG

mBOLD vs. EMG

With the addition of the EMG signal to the data, creating a multimodal dataset, the models show different levels of fit. The two model are shown in Appendices A.3 and A.4. The coherence significance of fit was $2.3109 \times ^{-06}$ and 0.0014799 for the fractility. This difference pushed the fractility measure into the realm of significance, indicating that the fractility of the connection between the mBOLD signal and the EMG signal was better suited to being modelled than the mBOLD alone. This also applied to the coherence model as the model fit was also better in that model as well. Compared to the model with solely the mBOLD signal, the measures that showed promise may shift with the introduction of new modalities. The underlying fundamentals of the modalities and their interactions will dictate which features and measures are most appropriate; showing reasoning for further explorations of the multimodal applications of muscle GSP.

7.2.2 Alternatives

In this thesis, the hypothesis focused on modelling the coherence and fractility with the GSP approach; the statistical analysis also followed this approach. However, the modelling can be done in the reverse direction with the activation function of the exercise protocol being the response. The function for such a model is shown below with the output shown in Appendix A.5. The purpose of such a model would be to estimate an activation pattern of the muscle from the measured mBOLD and EMG data. The applications of such a model might include recovering the activation pattern of involuntary contraction.

```
───────────────── Alternative Formula ─────────────────
 Activation ~ 1 + Time_Point + Edge_Dijkstra_C

 + Edge_Dijkstra_CL + Coherence*Fractal

 + Node_Type_N:Edge_Type_N:Edge_Eucl

 + (1 + Node_Type_N*Edge_Type_N + Coherence*Fractal | Subject_Number)
```

Chapter 8

Future Work and Conclusions

8.1 Future Work

8.1.1 EMG Improvements

Moving forward, redesigning and rebuilding the EMG system should be done to improve both signal quality and system usability. The first step would be to replace the through hole components with surface mount components to be able to drastically reduce the footprint of the device; reducing the loop lengths of the board in the process. The next improvement would be to replace the Analog Discovery 2 as a power supply with a battery and a non-switching voltage regulator to keep noise to a minimum. The schematic for such a rail splitting and conditioning circuit is shown in Figure 8.2. The current instrumentation amplifier pre-amplifier can be expanded for better performance with AC decoupling and boosting the signal integrity with noise return paths as shown in Figure 8.1. Following that, the removal of the external ADC and adding an onboard chip that will run off the same battery as the amplifier, thus drastically reducing the footprint. Designing the system with connectors for future expansion means that multiple channels can

91

be used in the future. This would allow for techniques such as calculating the inverse source calculation of muscle currents by creating an EMG mesh network. Finally, the EMG system should be integrated into the MR system so that starting the acquisition can be automated. Figure 8.3 shows what such a revision would look like, being much more compact while also adding and improving functionality.
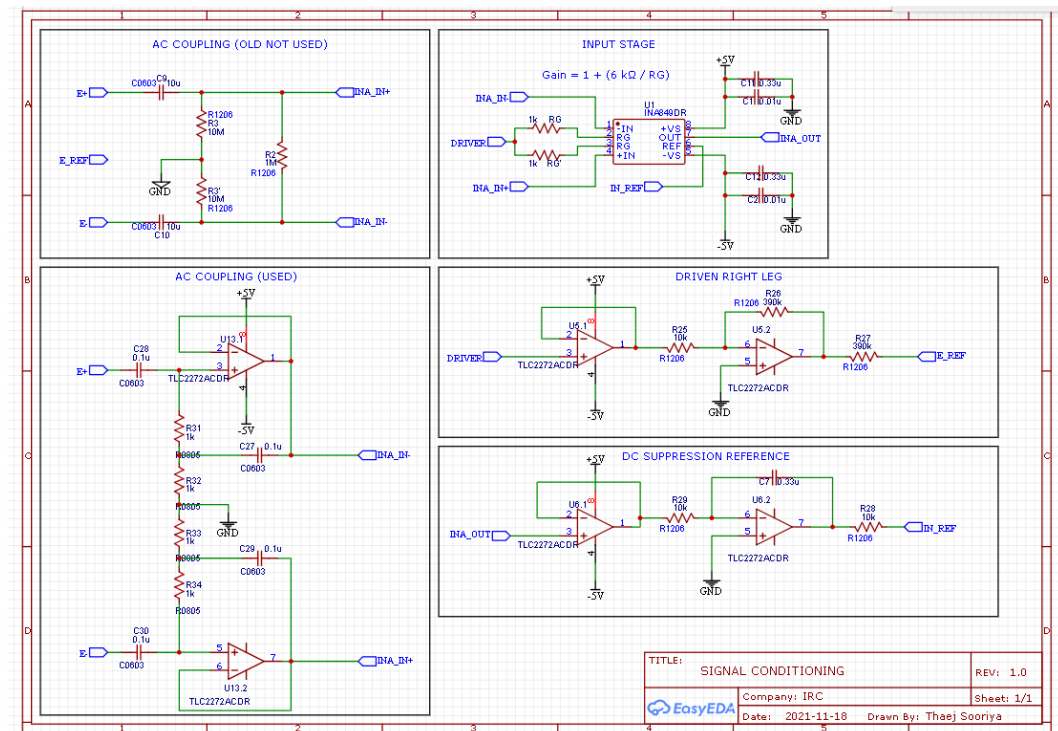
FIGURE 8.1: Compact EMG System: Pre-Amplifier stages showing blocks for different portions of the circuit. AC coupling to improve the impedance matching of the signal. Driven leg return paths to compensate for rejection loss caused by AC coupling stage. DC suppression of the reference electrode to drive ground noise to low values.

8.1.2   Calf Atlas

One source of variance in this investigation was the inter-participant differences in calf morphology. This can be remedied going forward by creating a calf atlas
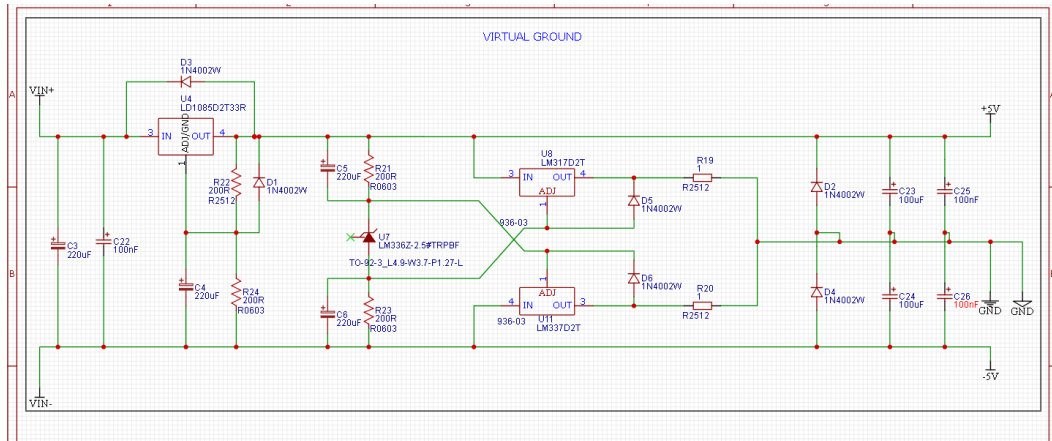
FIGURE 8.2: Compact EMG System: Virtual ground circuitry. Using battery supply as opposed to an active supply to remove wall outlet noise. The proposed circuit works with the help of a singular voltage regulator to clamp the battery output as it discharges to a constant 12V level. This is followed by a complementary pair of ± 5V regulators to generate and clamp the positive supply rails. These two regulators are also part of a network that is then used to create the virtual ground exactly half the potential of the two rails.

similar to those used in brain analyses to tether all scans to one brain. This would also make expanding the data-set to more practical. Adding participants would become easier as a single set of masks could be used for all new legs. In contrast, manually generating masks for each incoming leg would both be tedious and add unnecessary subjectivity to the masks.

It should also be noted that there are other anatomical properties of the calf that are distinctively different from the head. The leg is more likely to store fat than the human head, meaning that there are signal impacts that can be induced due to the fat. One such artifact that can arise is the dielectric effect artifact, which causes signal intensities and losses due to the creation of a standing wave within the anatomy. When standardizing scans, phenomena like the dielectric effect must be either compensated- or accounted-for.
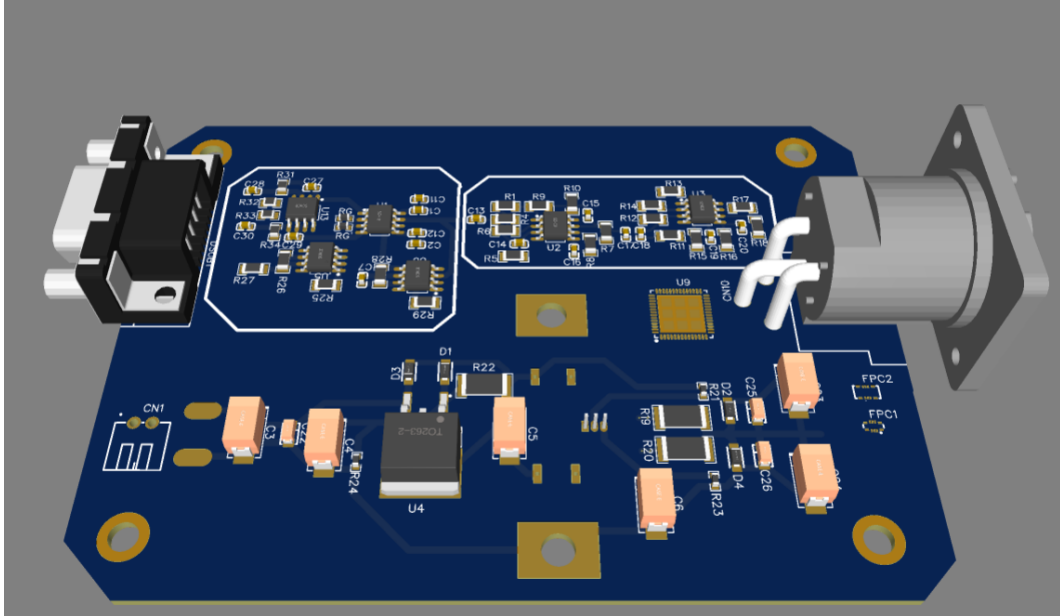
FIGURE 8.3: Compact EMG System: Rendering showing the proposed system. With a much smaller footprint than the current EMG amplifier while also containing the power supply and sampling circuitry. This would drastically reduce the effort needed in moving the system into the scanner room.

8.1.3 Graph Signal Operations

One benefit for transforming data into a graph signal representation is that there are operations that are exclusive to graphs and graph signals. One example of this is Djikstra's algorithm for finding the shortest path of traversal through the nodes. There is merit to this metric as the metric changed over time with the continued exertion of the muscle. There exist other functions from the graph theory field that are prime candidates for further investigation. An example of this determining the energy within a network. The scope of this field is large and diverse; application-specific operations can be extremely useful in modelling data.
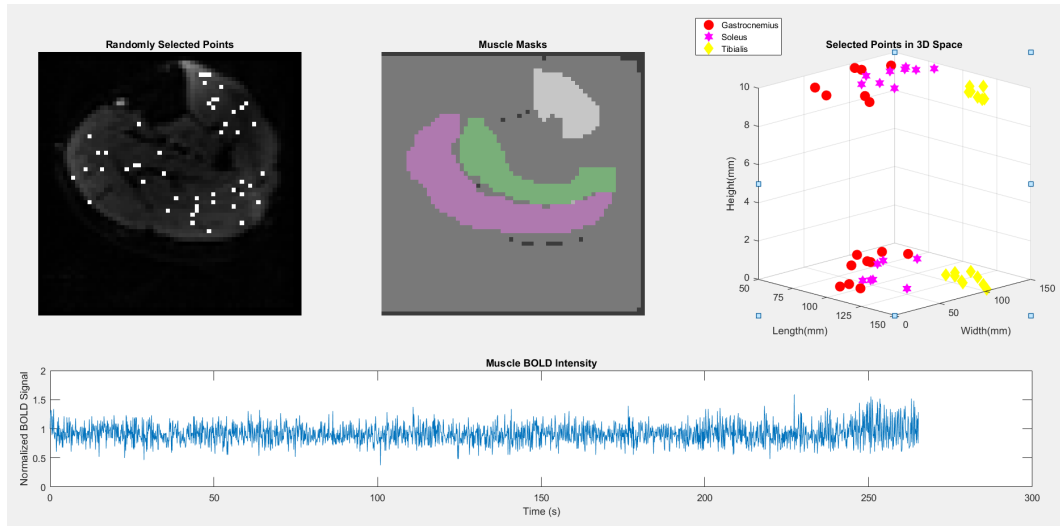
FIGURE 8.4: Functional mBOLD Data Sampling: Depending on the chosen voxel position, there may not be any activation recorded even within the bounds of the muscle. This could be remedied with the creation of a calf atlas space so voxel selection does not require random sampling.

8.1.4 Scanning Protocol

To improve the accuracy of the pipeline, the acquired data must have the resolution to do so. Due to the coarse spatial resolution of the mBOLD imaging, fibre level analysis is not possible and is a partial volume effect. Improving the spatial resolution would allow for much finer analysis of the muscle. This can be done with multi-band acquisition to retain the temporal resolution. The protocol can also be adapted to use isometric contractions to minimize the motion artifact and to ensure muscle fibres remain within the same voxel during rest and contraction.

8.1.5 Processing

As discussed previously, the processing pipeline developed in this thesis is very resource intensive. Further optimization of the code and a transition away from

MATLAB to a more resource efficient framework will be vital in making the pipeline more efficient.

Additionally, incorporating the modelling of the underlying physiological phenomena will improve the correlation between the analysis and bodily function. Similarly to the cerebral blood flow which has been modelled in response to a stimulus. The addition of a muscle blood flow response to the analysis will improve determination of contraction onset.

Another factor to be added in future endeavours is the inclusion of fibre-tracking diffusion imaging. This would allow for a fibre directional weighting to be added to the analysis, so that any directional effect of the muscle fibre directions can be incorporated into the model.

8.1.6   Co-Acquisition brain and muscle BOLD

The concurrent acquisition of both brain and muscle functional data would allow for the analysis of both brain and muscle networks at rest, exercise onset, fatigue onset, exercise offset, and recovery. Overall it would push forward the understanding of cortico-muscular connections and how they respond to exercise. Currently this is not easy to do, the arm over head technique allows for such imaging (Tang et al. 2020). However the AOH is hindered by distortion and is not applicable to other muscles in the body. Before this can be implemented into this pipeline, the ability to image both types of BOLD concurrently must be further developed.

8.2 Conclusions

This investigation collected mBOLD and concurrent EMG/mBOLD data, generated a pipeline for creating graph signal representations of the data, and assessed the generated models for significance. The results of this project highlight the promise GSP as a tool for human muscle analysis; for assessing exercise in a muscle BOLD functional scan, and in a multimodal form with the addition of an EMG signal.

Further refinement and adaptations would create a more robust framework that could be used for other muscles throughout the body. The analysis could also be used for those outside of the healthy range, to model progression of muscle activation for various pathologies. Examples being neurogenic myopathies present differently than diabetic myopathies. These differences may be better represented with a GSP approach. In conclusion, this investigation showed the viability of graph signal processing approaches to muscle analysis, warranting further exploration in the pursuit of representing and understanding muscular function.

Appendix A

Model Results

A.1   Exercise mBOLD Coherence Model

```
──────────────────── Coherence ────────────────────


  Generalized linear mixed-effects model fit by PL


  Model information:

   Number of observations          1566720

   Fixed effects coefficients            5

   Random effects coefficients          22

   Covariance parameters                 5

   Distribution                     Normal

   Link                             Identity

   FitMethod                        MPL


  Formula:

   Linear Mixed Formula with 7 predictors.


  Model fit statistics:

   AIC          BIC          LogLikelihood    Deviance

   2.6266e+06   2.6267e+06   -1.3133e+06      2.6266e+06

  Fixed effects coefficients 95% CIs:

   Name                      Estimate      SE          tStat      DF

   'Intercept'                0.19698      0.045221    4.356      1.5667e+06

   'Time_Point'              -4.0499e-06   1.5126e-06  -2.6775    1.5667e+06
```

'Edge_Eucl'	-0.0063962	4.801e-05	-133.22	1.5667e+06
'Edge_Dijkstra_C'	-0.016332	0.00017762	-91.954	1.5667e+06
'Node_Type_N:Edge_Type_N'	-0.034511	0.013434	-2.5689	1.5667e+06

pValue	Lower	Upper
1.3245e-05	0.10835	0.28562
0.0074168	-7.0145e-06	-1.0854e-06
0	-0.0064903	-0.0063021
0	-0.016681	-0.015984
0.010201	-0.060841	-0.0081811

Random effects covariance parameters:

Group: Activation 2 Levels

Name1	Name2	Type	Estimate
'Intercept'	'Intercept'	'std'	0.0051318

Group: Subject_Number 10 Levels

Name1	Name2	Type	Estimate
'Intercept'	'Intercept'	'std'	0.14208
'Node_Type_N:Edge_Type_N'	'Intercept'	'corr'	-0.89169
'Node_Type_N:Edge_Type_N'	'Node_Type_N:Edge_Type_N'	'std'	0.042473

Group: Error

Name	Estimate
'sqrtDispersion'	0.55948

A.2   Exercise mBOLD Fractal Model

———————— Fractal ————————

Generalized linear mixed-effects model fit by PL

Model information:

Number of observations	1566720
Fixed effects coefficients	5
Random effects coefficients	22
Covariance parameters	5
Distribution	Normal

```
Link                    Identity

FitMethod               MPL


Formula:

  Linear Mixed Formula with 7 predictors.


Model fit statistics:

  AIC           BIC           LogLikelihood    Deviance

  -2.6363e+06   -2.6362e+06   1.3182e+06       -2.6363e+06

Fixed effects coefficients 95% CIs:

  Name                        Estimate     SE           tStat      DF

  'Intercept'                 0.007983     0.0043207    1.8476     1.5667e+06

  'Time_Point'                -8.694e-06   2.8194e-07   -30.836    1.5667e+06

  'Edge_Eucl'                 -0.00014854  8.9514e-06   -16.594    1.5667e+06

  'Edge_Dijkstra_C'           0.00048586   3.3116e-05   14.672     1.5667e+06

  'Node_Type_N:Edge_Type_N'   -0.0030606   0.0012904    -2.3718    1.5667e+06


  pValue      Lower         Upper

  0.06466     -0.00048548    0.016451

        0     -9.2465e-06   -8.1414e-06

        0     -0.00016608   -0.00013099

        0      0.00042096    0.00055077

  0.017701    -0.0055897    -0.00053145

  Random effects covariance parameters:

Group: Activation 2 Levels

    Name1             Name2            Type        Estimate

    'Intercept'       'Intercept'      'std'       0.00021591

Group: Subject_Number 10 Levels

    Name1                     Name2                     Type        Estimate

    'Intercept'               'Intercept'               'std'       0.013612

    'Node_Type_N:Edge_Type_N' 'Intercept'               'corr'      -0.51741

    'Node_Type_N:Edge_Type_N' 'Node_Type_N:Edge_Type_N' 'std'       0.0040773

Group: Error

    Name              Estimate

    'sqrtDispersion'  0.10432
```

A.3   EMG and mBOLD Coherence Model

──────────────────── EMG Coherence Results ────────────────────

```
Generalized linear mixed-effects model fit by PL


Model information:

    Number of observations          1751040

    Fixed effects coefficients         5

    Random effects coefficients       22

    Covariance parameters              5

    Distribution                   Normal

    Link                           Identity

    FitMethod                      MPL


Formula:

    Linear Mixed Formula with 8 predictors.


Model fit statistics:

    AIC         BIC        LogLikelihood   Deviance

    2.8096e+06  2.8097e+06  -1.4048e+06    2.8095e+06
```

Fixed effects coefficients 95% CIs:

Name	Estimate	SE	tStat	DF
'Intercept'	0.10825	0.022914	4.7242	1.751e+06
'Time_Point'	-3.801e-05	1.3805e-06	-27.534	1.751e+06
'Edge_Eucl'	-0.0070176	3.0562e-05	-229.62	1.751e+06
'Edge_Dijkstra_C'	-0.022023	0.00014997	-146.85	1.751e+06
'Node_Type_N:Edge_Type_N:EMG'	0.0011258	0.0043495	0.25883	1.751e+06

pValue	Lower	Upper
2.3109e-06	0.063339	0.15316
0	-4.0716e-05	-3.5305e-05
0	-0.0070775	-0.0069577
0	-0.022317	-0.021729
0.79577	-0.007399	0.0096506

```
Random effects covariance parameters:

Group: Activation 2 Levels
```

Name1	Name2	Type	Estimate
'Intercept'	'Intercept'	'std'	0.0068923

Group: Subject_Number 10 Levels

Name1	Name2	Type	Estimate
'Intercept'	'Intercept'	'std'	0.069587
'Node_Type_N:Edge_Type_N:EMG'	'Intercept'	'corr'	-0.23966
'Node_Type_N:Edge_Type_N:EMG'	'Node_Type_N:Edge_Type_N:EMG'	'std'	0.013747

Group: Error

Name	Estimate
'sqrtDispersion'	0.53971

A.4   EMG and mBOLD Fractal Model

——————————— EMG Fractal ———————————

Generalized linear mixed-effects model fit by PL

Model information:

Number of observations	1751040
Fixed effects coefficients	5
Random effects coefficients	22
Covariance parameters	5
Distribution	Normal
Link	Identity
FitMethod	MPL

Formula:

   Linear Mixed Formula with 8 predictors.

Model fit statistics:

AIC	BIC	LogLikelihood	Deviance
-2.8859e+06	-2.8858e+06	1.443e+06	-2.8859e+06

Fixed effects coefficients 95% CIs:

Name	Estimate	SE	tStat	DF

'Intercept'	0.015664	0.0049279	3.1786	1.751e+06
'Time_Point'	-7.5004e-06	2.7168e-07	-27.608	1.751e+06
'Edge_Eucl'	-0.00053071	6.0101e-06	-88.302	1.751e+06
'Edge_Dijkstra_C'	0.0012603	2.9491e-05	42.736	1.751e+06
'Node_Type_N:Edge_Type_N:EMG'	0.00050386	0.0004326	1.1647	1.751e+06

pValue	Lower	Upper
0.0014799	0.0060053	0.025322
0	-8.0329e-06	-6.9679e-06
0	-0.00054249	-0.00051893
0	0.0012025	0.0013181
0.24414	-0.00034403	0.0013517

```
 Random effects covariance parameters:
Group: Activation 2 Levels
```

Name1	Name2	Type	Estimate
'Intercept'	'Intercept'	'std'	0.0045252

```
Group: Subject_Number 10 Levels
```

Name1	Name2	Type	Estimate
'Intercept'	'Intercept'	'std'	0.011209
'Node_Type_N:Edge_Type_N:EMG'	'Intercept'	'corr'	-0.64762
'Node_Type_N:Edge_Type_N:EMG'	'Node_Type_N:Edge_Type_N:EMG' 'std'		0.0013653

```
Group: Error
```

Name	Estimate
'sqrtDispersion'	0.10614

A.5   EMG and mBOLD Alternative Model

```
──────────────────── EMG Fractal ────────────────────


Generalized linear mixed-effects model fit by PL


Model information:
    Number of observations          1575936
    Fixed effects coefficients           12
```

```
    Random effects coefficients        0

    Covariance parameters              1

    Distribution               Normal

    Link                       Identity

    FitMethod                  MPL
```

```
Formula:

    Linear Mixed Formula with 7 predictors.
```

```
Model fit statistics:

    AIC          BIC          LogLikelihood

    -6.4528e+06   -6.4526e+06   3.2264e+06
```

```
    Deviance

    -6.4528e+06
```

```
Fixed effects coefficients 95% CIs:

    Name                       Estimate

    'Intercept'                0.00087627

    'Node_Type_N'              -3.2569e-07

    'Edge_Type_N'               2.2963e-06

    'Coherence'                -1.6456e-05

    'Fractal'                   0.0008106

    'Edge_Eucl'                 4.1213e-08

    'Edge_Dijkstra_C'          -1.7393e-05

    'EMG'                      -3.3151e-05

    'Coherence:Fractal'        0.00028756

    'Coherence:EMG'            0.00014129

    'Fractal:EMG'              9.4086e-05

    'Coherence:Fractal:EMG'    -0.0016887
```

```
    SE           tStat        DF          pValue

    8.8167e-05    9.9387      1.5759e+06   2.8296e-23

    1.1047e-05   -0.029482    1.5759e+06    0.97648

    7.1826e-05    0.03197     1.5759e+06    0.9745

    4.7757e-05   -0.34459     1.5759e+06    0.73041

    0.0002458     3.2979      1.5759e+06    0.00097419

    2.2059e-06    0.018683    1.5759e+06    0.98509

    8.5721e-06   -2.029       1.5759e+06    0.042459
```

0.00012433	-0.26664	1.5759e+06	0.78975
0.00047108	0.61043	1.5759e+06	0.54158
0.00014596	0.96801	1.5759e+06	0.33304
0.00088047	0.10686	1.5759e+06	0.9149
0.0016501	-1.0234	1.5759e+06	0.30611

```
 Random effects covariance parameters:
Group: Error
    Name                  Estimate
    'sqrtDispersion'      0.031235
```

Appendix B

Code

B.1 Point Cloud and Table Generation

```matlab
1  %% 1a. Load in data; an anatomical and functional data
       set
2
3  filepath = 'C:\Users\sstje\Desktop\Schtough\School\GRAD\
       Signal Processing\FINAL_DATA\';
4
5  warning('off', 'all')
6  addpath(genpath(pwd))
7
8  %% 1b. Load in data; an anatomical and functional data
       set
9
10 victims= {'ALEX', 'BHANU', 'CALVIN', 'CAM', 'ESTEBAN', '
       ETHAN', 'JOSH', 'KONRAD', 'TJ', 'YVES'};
11 for qqq = 1 : size(victims,2)
```

```matlab
12  victim = char(victims(qqq))
13  V_anat = load_nii([filepath victim '\Niftis\Anat.nii']);
14  vol_anat = V_anat.img;
15
16  V_act = load_nii([filepath victim '\Niftis\
        BOLD_Block_SAT_MC_AL.nii.gz']);
17  V_rst = load_nii([filepath victim '\Niftis\
        BOLD_Rest_SAT_MC_AL.nii.gz']);
18  vol = V_act.img;
19
20  dt = V_act.hdr.dime.pixdim(5);
21
22  imshow(rot90(vol_anat(:,:,1,1)),[])
23
24
25  %% 1c. Load in masks for the leg muscles
26
27  mask_gas= load_nii([filepath victim '\Niftis\
        BOLD_mask_gas_consrv_less.nii.gz']);
28  mask_sol= load_nii([filepath victim '\Niftis\
        BOLD_mask_sol_consrv_less.nii.gz']);
29  mask_tib= load_nii([filepath victim '\Niftis\
        BOLD_mask_tib_less.nii.gz']);
30  V_mask_gas = mask_gas.img;
31  V_mask_sol = mask_sol.img;
```

```matlab
32  V_mask_tib = mask_tib.img;
33
34  %% 1d. Load in downsampled EMG data
35
36  EMG = load([filepath victim '\EMG_ds.mat']);
37  emg = EMG.yds';
38  clear EMG
39
40  %% 2. Generate Point cloud and visualize time series
        from points and point cloud
41  % Number of points, must be a multiple of the number of
        masks, in this case
42  % 3
43  % Was 48
44  N = 18;
45
46  set = 30; % Time of exercise block
47  % Get volume-series size data
48  [length, width, depth, time_points] = size(vol);
49
50  nt = 1024;
51  ns = 2^11;
52  dt = 0.250;
53  sess = 30;
54
```

```matlab
55
56 sesst = nt/(sess*dt);
57 t = 0:dt:(nt-1)*dt;
58 % Generate activation function
59 act = 1-flip(mod( floor( t(end-nt+1:end)/(sesst*dt) )
       ,2));
60
61 plot(t, act)
62 title('Activation Function')
63 xlabel('Time (s)')
64 ylabel('Block (ON/OFF)')
65
66 emgc = emg(end-nt+1:end);
67 % hold on
68 % plot(t,emgc)
69 % hold off
70 %
71
72 %%
73 % Time series holding varible
74 T = zeros(N+1, nt);
75
76 % Slices to visualize point cloud
77 x = vol(:,:,1,1);
78
```

```matlab
% Point cloud
%First list points by the axes
X = zeros(1,N);
Y = zeros(1,N);
Z = zeros(1,N);


%Generate truth vectors for point positions
M_gas = zeros(1,N);
M_sol = zeros(1,N);
M_tib = zeros(1,N);

i     = 1;
valid = 0;

for (i = 1:N)


    if (i >= 1 && i <= N/3)
        [x_co, y_co, z_co] = ind2sub(size(V_mask_gas),
            find(V_mask_gas));
        M_gas(i) = 1;
    elseif (i > N/3 && i <= 2*N/3)
        [x_co, y_co, z_co] = ind2sub(size(V_mask_sol),
            find(V_mask_sol));
```

```
102             M_sol(i) = 1;
103         elseif (i > 2*N/3 && i <= N)
104             [x_co, y_co, z_co] = ind2sub(size(V_mask_tib),
                    find(V_mask_tib));
105             M_tib(i) = 1;
106         end
107
108         while (valid == 0)
109
110             xyz_rand = randperm(size(x_co,1),1);
111             X(i) = x_co(xyz_rand);
112             Y(i) = y_co(xyz_rand);
113             Z(i) = z_co(xyz_rand);
114
115             vv = (double(squeeze(vol(Y(i),X(i),Z(i),end-nt
                    +1:end)))./double(squeeze(vol(Y(i),X(i),Z(i),
                    end-nt+1)))));
116
117             plot(vv)
118
119             if (max(vv) > 1.5 || (qqq==8))
120                 valid = 1;
121             end
122
123 %           pause(1)
```

```matlab
124         end
125         valid = 0;
126 end
127
128 %%check if equal number of points in each mask region
129
130 for ( i = 1:N )
131     if (i == (N))
132         if ( ~( (sum(M_gas) == N/3) && (sum(M_sol) == N
                /3) && (sum(M_tib) == N/3) ) )
133             disp('Not equal')
134         elseif ( (sum(M_gas) == N/3) && (sum(M_sol) == N
                /3) && (sum(M_tib) == N/3) )
135             disp('Equal')
136         end
137     end
138 end
139
140
141 %Aggregate points into point cloud
142 % P = [X;Y;Z]; Reorder due to MATLAB matrix notation
143 P = [Y;X;Z];
144
145
146 % Subplot positions
```

```matlab
147  pos1 = [0.01 0.4 0.3 0.5];

148  pos2 = [0.35 0.4 0.25 0.5];

149  pos3 = [0.7 0.4 0.25 0.5];

150  pos4 = [0.05 0.075 0.9 0.3];

151

152  %  h=figure;

153  h=gcf;

154  clf(h);

155  % set(h, 'Position', get(0, 'Screensize'));

156  imshow(x,[])

157  filename = 'PointACQ.gif';

158  % Show point and time series corresponding to the point

159

160  Legend = cell(3,1);

161  lg = legend();

162

163  for i = 1:N

164      x( X(i) , Y(i) ) = 5000;

165

166      T(i,:) = squeeze(vol(P(1,i),P(2,i),P(3,i),end-nt+1:
             end));

167      subplot('Position',pos1)

168      imshow(rot90(x),[],'InitialMagnification', 'fit')

169      title('Randomly Selected Points')

170
```

```matlab
171     subplot('Position',pos2)
172     ha = imshow(rot90(vol(:,:,1,1)),[]);
173     ha.AlphaData = 0.5;
174     hold on
175     hc = imshow(rot90(imfuse(V_mask_sol(:,:,2),
            V_mask_gas(:,:,2))));
176     hc.AlphaData = 0.3;
177
178     hb = imshow(rot90(V_mask_tib(:,:,1)),[]);
179     hb.AlphaData = 0.3;
180     title('Muscle Masks')
181     hold off
182
183     hd = subplot('Position',pos3);
184     hold on
185         if (M_gas(i) == 1)
186             hd1 = plot3(P(1,i),P(2,i),P(3,i),'ro', '
                    MarkerSize', 10, 'MarkerFaceColor', 'r');
187 %           lg = legend(hd, {'Gastrocnemius'})
188         elseif (M_sol(i) == 1)
189             hd2 = plot3(P(1,i),P(2,i),P(3,i),'mh', '
                    MarkerSize', 10, 'MarkerFaceColor', 'm');
190 %           lg = legend(hd, {'Soleus'})
191         elseif (M_tib(i) == 1)
```

```matlab
192                hd3 = plot3(P(1,i),P(2,i),P(3,i),'yd', '
                       MarkerSize', 10, 'MarkerFaceColor', 'y');
193 %               lg = legend(hd, {'Tibialis'})
194          else
195              plot3(P(1,i),P(2,i),P(3,i),'ko', 'MarkerSize
                     ', 10);
196          end
197          view( 45, 15)
198          grid on
199
200 %    legend(hd, {'Gastrocnemius', 'Soleus', 'Tibialis
       '}, 'Location', 'northwest')
201     title('Selected Points in 3D Space')
202
203 %    Legend{1} = '1';
204 %    Legend{2} = '2';
205 %    Legend{3} = '3';
206 %    legend(Legend)
207     hold off
208
209
210
211 %    imshow(rot90(z),[],'InitialMagnification', 'fit')
212 %    truesize([1024 512])
213 %    subplot(2,1,2)
```

```matlab
214        subplot('Position',pos4)
215        plot(t,T(i,:)./(T(i,1)))
216        title('mBOLD intensity')
217        xlabel('Time (s)')
218        pause(0.1)
219 %      set(h, 'Position', get(0, 'Screensize'));
220 %      frame = getframe(h);
221 %      im = frame2im(frame);
222 %      [imind,cm] = rgb2ind(im,256);
223
224 %      if i==1
225 %          imwrite(imind,cm,filename,'gif','Loopcount',
        inf);
226 %      else
227 %          imwrite(imind,cm,filename,'gif','WriteMode','
        append');
228 %      end
229 end
230
231 subplot('Position', pos3)
232 legend([hd1, hd2, hd3], {'Gastrocnemius','Soleus','
        Tibialis'}, 'Location' , 'northeast')
233
234 %%
235
```

```matlab
236  N = N+1;
237  T(end,:) = emgc;
238
239
240  %% 3. Run Pipeline
241
242  % Add Mask Truth Vectors to Point Cloud
243  P = [Y;X;Z;M_gas;M_sol;M_tib];
244  P = padarray(P,[1 1], 'post');
245  P(end,end) = 1;
246  P(1:3,end) = 1;
247  vol_pipe = double(vol(:,:,:,end-nt+1:end));
248  vol_pipe(1,1,1,:) = (emgc);
249
250  %%
251  gr = Pipeline_EMG( vol_pipe, act, N, P, nt );
252
253  %% 4. Visualize Generated Graph
254  %
255  % thres1 = 0.1;
256  % disp('Viewing Dimension 1: DOST Coherence,')
257  % disp('Threshold: ')
258  % disp(thres1);
259  % Visualize_Graph_EMG(gr , thres1 , 1 , vol_pipe);
260  %
```

```matlab
261  %%
262  % thres2 = 0.05;
263  % disp('Viewing Dimension 2: Fractal (HFD) Difference,')
264  % disp('Threshold: ')
265  % disp(thres2);
266  % Visualize_Graph_EMG(gr , thres2 , 2 , vol_pipe);
267
268  %% 5. Extract Statistical Information
269  %% 5a. Extract Edge Connection Types
270
271  % Edge Types (6 Total)
272  %    - Gas--Gas
273  %    - Gas--Sol
274  %    - Gas--Tib
275  %    - Sol--Sol
276  %    - Sol--Tib
277  %    - Tib--Tib
278
279  % 1 = GG | 2 = GS | 3 = GT | 4 = SS | 5 = ST | 6 = TT
280
281
282  %%
283
284  Mask_Type_Enum = {'Gas' 'Sol' 'Tib' 'EMG'};
285
```

```matlab
286  Edge_Type_Enum = cell(1,factorial(size(Mask_Type_Enum,2)
        ));
287  Conn_Type_Enum = zeros(size(Edge_Type_Enum));
288
289  idx = 1;
290
291  for i = 1:size(Mask_Type_Enum,2)
292      for ii = i:size(Mask_Type_Enum,2)
293          if(idx > size(Edge_Type_Enum,2))
294              break
295          end
296          Edge_Type_Enum(idx) = strcat(Mask_Type_Enum(i),
                 '-', Mask_Type_Enum(ii));
297          if (i == ii)
298              Conn_Type_Enum(idx) = 0;
299          else
300              Conn_Type_Enum(idx) = 1;
301          end
302          idx = idx + 1;
303      end
304  end
305
306
307  %% 5b. Generate Table
```

```matlab
NV = N*(N-1)/2; % Number of Non-Repeated Values in a
    Symmetric Matrix
Subject_Number = qqq*ones(NV,1);

tbl = table(Subject_Number, 'VariableNames', {'
    Subject_Number'});
tbl.Time_Point          = ones(NV,1);
tbl.Node_Type           = cell(NV,1);
tbl.Node_Type_N         = zeros(NV,1);
tbl.Edge_Type           = cell(NV,1);
tbl.Edge_Type_N         = zeros(NV,1);
tbl.Coherence           = zeros(NV,1);
tbl.Fractal             = zeros(NV,1);
tbl.Edge_Eucl           = zeros(NV,1);
tbl.Edge_Dijkstra_C     = zeros(NV,1);
tbl.Edge_Dijkstra_CL    = zeros(NV,1);
tbl.Edge_Dijkstra_F     = zeros(NV,1);
tbl.Edge_Dijkstra_FL    = zeros(NV,1);
tbl.Activation          = zeros(NV,1);
tbl.EMG                 = zeros(NV,1);


%
```

```matlab
% tbl = table( vert_frac, vert_edges, vert_node,
    vert_edge_type, 'VariableNames' , {'Fractal', '
    Coherence', 'EdgeType', 'NodeType'});
%


idx = 1;
for i = 1:N
    for j = i+1:N


        a = Mask_Type_Enum(find(gr.Node_Positions(4:end,
            i)));
        b = Mask_Type_Enum(find(gr.Node_Positions(4:end,
            j)));


        if ((i == 7) || (j == 7))
            %disp(i )
            tbl.Edge_Type(idx) = {'2EMG'};
            tbl.Edge_Type_N(idx) = 2;
            tbl.EMG(idx) = 1;
        else
            if isequal(a,b)
                tbl.Edge_Type(idx) = {'0Intra'};
                tbl.Edge_Type_N(idx) = 0;
            else
                tbl.Edge_Type(idx) = {'1Inter'};
```

```matlab
350                    tbl.Edge_Type_N(idx) = 1;
351                end
352            end
353
354
355        tbl.Node_Type(idx)  = strcat(a, '-', b);
356
357        for ii = 1:size(Edge_Type_Enum,2)
358            if isequal(tbl.Node_Type(idx),Edge_Type_Enum(ii)
                    )
359                tbl.Node_Type_N(idx) = ii;
360            end
361        end
362
363
364        tbl.Coherence(idx)  = gr.Edge_Weights(1,i,j,1);
365        tbl.Fractal(idx)    = gr.Edge_Weights(2,i,j,1);
366        tbl.Edge_Eucl(idx)  = sqrt( (gr.Node_Positions(1,i)-
                gr.Node_Positions(1,j))^2 + ...
367            (gr.Node_Positions(2,i)-gr.Node_Positions(2,j))
                    ^2 + ...
368            (gr.Node_Positions(3,i)-gr.Node_Positions(3,j))
                    ^2);
369        [costC routeC] = dijkstra(squeeze( gr.Edge_Weights
                (1,:,:,1)), i, j);
```

```matlab
370         tbl.Edge_Dijkstra_C(idx)  = costC;
371         tbl.Edge_Dijkstra_CL(idx) = size(routeC,2);
372         [costF routeF] = dijkstra(squeeze( gr.Edge_Weights
               (2,:,:,1)), i, j);
373         tbl.Edge_Dijkstra_F(idx)  = costF;
374         tbl.Edge_Dijkstra_FL(idx) = size(routeF,2);
375         tbl.Activation(idx) = act(1);
376         idx = idx + 1;
377         end
378 end
379
380
381
382 temptbl       = tbl(1:NV,:); % Will  copy  over  the
       Node_Type  and  Edge_Type  values  over  so  only  need  to
       change  the  metrics
383 tempCoherence = zeros(NV,1);
384 tempFractal   = zeros(NV,1);
385
386 for tt = 2:nt
387     temptbl.Time_Point(:) = tt*ones(NV,1);
388     idx = 1;
389     for i = 1:N
390         for j = i+1:N
```

```matlab
391                tempCoherence(idx) = gr.Edge_Weights(1,i,j,
                      tt);
392                if (isinf(gr.Edge_Weights(2,i,j,tt)))
393                    tempFractal(idx) = 0;
394                else
395                    tempFractal(idx) = gr.Edge_Weights(2,i,j
                          ,tt);
396                end
397                [costC, routeC] = dijkstra(squeeze( gr.
                      Edge_Weights(1,:,:,tt)), i, j);
398                tbl.Edge_Dijkstra_C(idx)  = costC;
399                tbl.Edge_Dijkstra_CL(idx) = size(routeC,2);
400                [costF, routeF] = dijkstra(squeeze( gr.
                      Edge_Weights(2,:,:,tt)), i, j);
401                tbl.Edge_Dijkstra_F(idx)  = costF;
402                tbl.Edge_Dijkstra_FL(idx) = size(routeF,2);
403                tbl.Activation(idx) = act(tt);
404                idx = idx+1;
405            end
406        end
407        temptbl.Coherence = (tempCoherence);
408        temptbl.Fractal = (tempFractal);
409        tbl = vertcat(tbl, temptbl);
410  end
411
```

```matlab
412 %%
413 save([filepath, '\FINAL_verts_long\EMG\', victim ,'
       _verts.mat'], 'tbl')
414 %%
415
416 disp('done')
417
418
419 end
420
421 %
```

B.2   Pipeline

```matlab
function [ graph ] = Pipeline_EMG( vol, act, N, PC, tp )
%% Function to perfom Graph Theory/S-Transform Pipeline
% Inputs:
%        fMRI BOLD Volume-Time Series {vol}
%        Activation Function          {act}
%        Number of points             {N}  %Redundant,
    can use length(PC)
%        instead
%        Point Cloud Coordinates      {PC}
%        Number of Time Points (2^N)  {tp} %Redundant,
    can use 4th dimension
%        length of vol
%
%Outputs:
%        Graph structure              {graph}
%

disp('PIPELINE STARTED')
tic
%% 0. Graph Structure
%   Create data structure to store graph:
%        Node weights }--> function of time?
%        Edge weights }--> is a function of time
```

```matlab
22  %        Number of Nodes
23  %        Edge connections
24
25
26  graph = struct('Nodes', {}, ...
27      'Node_Weight_dim', {}, 'Node_Weights', {}, ...
28      'Node_Positions', {}, ...
29      'Edge_Weight_dim', {}, 'Edge_Weights', {}, ...
30      'Time_Points', {}, 'Data_Points', {},  ...
31      'Basis', {});
32
33  %% 1. Extract time series from Points
34
35  T = zeros(N, tp);
36
37  for i = 1:N
38      %If you want the first tps
39  %    T(i,:) = squeeze( vol( PC(2,i) , PC(1,i) , PC(3,i)
        , 1:tp ) );
40      %If you want the last tps
41      T(i,:) = squeeze( vol( PC(2,i) , PC(1,i) , PC(3,i) ,
          end-tp+1:end ) );
42
43  end
44
```

```matlab
45  %% 2. Generate DOST Spectrographs for each Time Series
46
47  ns = tp;
48  t = linspace(0,1,ns); % signal of 1s (0 to 1) sampled ns
        -times
49  f = linspace(-ns/2,ns/2 -1,ns); % frequencies
50
51  disp('Generating DOSTs')
52
53  % Generate DOST of the activation function
54  in = act(1:ns); % crop data to given power of 2
55  % fftIn = ST.fourier(in);
56  % fftIn(f==0) = 1;
57  dostIn = ST.dost(in);
58  recdostIn = ST.idost(ST.dost(in));
59
60  readableDostIn = ST.rearrangeDost(dostIn);
61  readableDostIn((f==-1),:) = readableDostIn((f==-1),:)./
        max(max(readableDostIn));
62
63  act_DOST = readableDostIn;
64
65  Out = zeros( N , tp , tp );
66
67  % Generate DOST of the data points from the Point Cloud
```

```matlab
68  for i = 1:N
69
70      in = T(i,1:ns);
71
72  %     fftIn = ST.fourier(in);
73  %     fftIn(f==0) = 1;
74      dostIn = ST.dost(in);
75      recdostIn = ST.idost(ST.dost(in));
76
77      readableDostIn = ST.rearrangeDost(dostIn);
78      readableDostIn((f==-1),:) = readableDostIn((f==-1)
            ,:)./max(max(readableDostIn));
79
80      Out( i , : , : ) = readableDostIn;
81
82  end
83  disp('Done DOST Generation')
84
85  %% 3. Correlation Time Series with Activation Function
86
87  % c_act = zeros(N, 2*tp-1, 2*tp-1);
88  g_act = zeros(N,2,2);
89  G     = zeros(N,1);
90
91  disp('Correlating Activation Function')
```

```matlab
92  for i = 1:N
93
94  %      c_act(i,:,:) = xcorr2( ( squeeze( Out(i,:,:) ) ) ) ,
        act_DOST );
95      g_act(i,:,:) = corrcoef( (squeeze( Out(i,:,:) ) ),
            act_DOST );
96      G(i)          = g_act(i,1,2);
97  end
98  disp('Done Activation Function Correlation')
99  %% 4. Column-wise Correlation of the DOST
100 % disp('Columns')
101 R = zeros(N,N,tp);
102 clf
103 disp('Starting Column-wise Correlation')
104 for i = 1:N
105     for ii = i:N
106         for j = 1:tp
107             A = squeeze( real( Out(i,:,j) ) );
108             B = squeeze( real( Out(ii,:,j) ) );
109             R (i,ii,j) =  corr( A' , B' );
110             R (ii,i,j) =  R (i,ii,j);
111         end
112     end
113 end
114 disp('Done Columin-wise Correlation')
```

```matlab
%% 5. Populate Graph

graph(1).Nodes                  = N;
graph.Node_Positions            = PC;
graph.Node_Weights(1,:)         = G;
graph.Edge_Weights(1,:,:,:)     = R;
graph.Node_Weight_dim           = 1;
graph.Edge_Weight_dim           = 1;
graph.Time_Points               = tp;
graph.Data_Points(1,:,:)        = T;
graph.Basis                     = act;


%%
%% 6. Generate Second Dimension of Graph (Node and Edge
    Weights)

%% 6a. Fractal Dimension of Nodes

disp('Extracting Fractal Dimension')
Gf = zeros(N,1);

Window_Size = 128; %Window Size
Overlap_Window = 127; %Window Overlap

in = T(1,1:ns);
```

```matlab
[wdata] = SWG(in, Window_Size , Overlap_Window );
[r , ~] = size(wdata);% r gives the number of windows
% disp(r)
FD = zeros(N,r);
% disp(size(FD))


for i = 1:N


    % Extract (truncated) Data from Node i
    in = T(i,1:ns);
    % Generate windows for Time Series from Node i
    [wdata] = SWG(in, Window_Size , Overlap_Window);


    % Calculate Fractal Dimension
    for j=1:r
        % Fill Nxr (r=tp-Overlap) array with 1x1 fractal
              dimensions
        FD(i,j)=HFD_LCALC(wdata(j,:));
    end


    Gf(i) = HFD_LCALC(in);


end


disp('Done Extracting Fractal Dimension')
```

```matlab
163
164 %% 6b. Windowed Fractal Dimension of Nodes
165
166 disp('Correlating Fractal Dimension')
167 Rf = zeros(N,N,tp);
168 clf
169 for i = 1:N
170     for ii = i:N
171         for j = 1:r %tp
172 %             A = FD(i,:);
173 %             B = FD(ii,:);
174             A = FD(i,j);
175             B = FD(ii,j);
176 %             Rf (i,ii,j) =  corr( A' , B' );
177             Rf(i,ii,j) = A-B;
178             Rf(ii,i,j) = B-A;
179         end
180     end
181 end
182
183 disp('Done Fractal Correlation')
184
185 %% 5. Populate Graph
186
187 % graph(1).Nodes                   = N;
```

```matlab
% graph.Node_Positions          = PC;
graph.Node_Weights(2,:)         = Gf;
graph.Edge_Weights(2,:,:,:)     = Rf;
graph.Node_Weight_dim           = 2;
graph.Edge_Weight_dim           = 2;
disp('Fractal Dimension Data Zero Padded with 31 zeros')
graph.Data_Points(2,:,:)        = padarray(FD, [0
    Overlap_Window], 0,'post');
% graph.Basis                   = act;


%%
disp('PIPELINE DONE')
toc
end
```

```
212
213
214
215
216
217
218
219  %% Code Graveyard
```

B.3   EMG Filtering

```matlab
1
2  filepath = 'C:\Users\sstje\Desktop\Schtough\School\GRAD\
      Signal Processing\FINAL_DATA\';
3  Fs = 5000;
4  T = 5*60;
5  lpf = 200;
6  hpf = 20;
7  TR = 0.250;
8  LF = 1/TR; % 4
9
10 N = T*Fs; %Retrieve size of data
11 t = 0:1/Fs:(N-1)/Fs; %Reconstruct time vector
12 f = (-N/2:1:(N-1)/2)*Fs/N; %Construct frequency vector
13 victims= {'ALEX', 'BHANU', 'CALVIN', 'CAM', 'ESTEBAN', '
      ETHAN', 'JOSH', 'KONRAD', 'TJ', 'YVES'};
14
15 for qqq = 1 : size(victims,2)
16
17     %%
18     victim = char(victims(qqq));
19
20     direc = dir(fullfile([filepath victim '\'], '*.lvm')
          );
```

```matlab
Data = lvm_import(direc.name);

y = Data.Segment1.data(1:T*Fs,2);

y = y./max(y);

clear Data direc


%% Plot raw data


plot(t./60,y) %Plot data with time

xlabel('Time (minutes)')

ylabel('normalized amplitude (V/V)')

title('Rectified EMG during MRI Sequencing')


HpFilt = designfilt('highpassfir', 'FilterOrder',
    500, 'CutoffFrequency', 3, ...
     'SampleRate', Fs);


bpFilt = designfilt('bandpassfir', 'FilterOrder',
    500, 'CutoffFrequency1', hpf, 'CutoffFrequency2',
     lpf, ...
     'SampleRate', Fs);


%%


plot(f, real(fftshift(fft(y))))

title('Raw EMG Spectrum')
```

```matlab
43    xlabel('Frequency (Hz)')
44    ylabel('Amplitude (V/V)')
45
46    %%
47
48    plot(t,y)
49    hold on
50
51    y = filter(HpFilt, y);
52    plot(t,y)
53    hold off
54
55    %% Wavelet denoising
56
57    yt = removeLineNoise_SpectrumEstimation(y', Fs, ['LF
          = ' num2str(LF) ', NH = 625'])';
58    yt = removeLineNoise_SpectrumEstimation(yt', Fs,'LF
         = 56, NH = 5, HW = 4')';
59
60
61    plot(t./60, yt);
62    title('EMG after Line Noise Removal')
63    xlabel('Time (Minutes)')
64    ylabel('Amplitude (V/V)')
65    %%
```

```matlab
66      plot(f, real(fftshift(fft(yt))))
67      title('EMG after Line Noise Removal')
68      xlabel('Frequency (Hz)')
69      ylabel('Amplitude (V/V)')
70      %%
71      coefs = cwt(yt,16:64,'bior6.8');
72      %%
73      yw    = sum(coefs(16:end,:));
74      ywr   = yw./max(yw);
75      clear coefs
76      plot(t./60,ywr)
77      title('EMG after Wavelet Denoising')
78      xlabel('Time (Minutes)')
79      ylabel('Amplitude (V/V)')
80 %     plot(t,abs(ywr))
81 %%
82      plot(f,real(fftshift(fft(ywr))))
83      title('EMG Spectrum after Wavelet Denoising')
84      xlabel('Frequency (Hz)')
85      ylabel('Amplitude (V/V)')
86
87      %%
88
89      ywr = removeLineNoise_SpectrumEstimation(ywr, Fs,['
           LF = ' num2str(LF) ', NH = 625'])';
```

```matlab
90      plot(t,ywr)

91

92      %%

93

94      ywrt = filter(bpFilt, ywr);

95      ywrt = removeLineNoise_SpectrumEstimation(ywrt', Fs
            ,['LF = ' num2str(LF) ', NH = 625'])';

96

97      plot(t./60,ywrt)

98      title('EMG Spectrum after Bandpass Filtering')

99      xlabel('Time (Minutes)')

100     ylabel('Amplitude (V/V)')

101

102

103     %%

104     % clear coefs

105

106     % figure

107     subplot(2,1,1)

108     plot(t./60, yt)

109     xlabel('Time (minutes)')

110     ylabel('EMG amplitude (V/V)')

111     title('EMG Signal (Denoised)')

112

113     subplot(2,1,2)
```

```matlab
114     plot(t./60, ywrt)
115     xlabel('Time (minutes)')
116     ylabel('EMG amplitude (V/V)')
117     title('EMG Signal (Denoised and Filtered) ')
118
119
120     %% Frequency plots
121     figure
122     subplot(3,1,1)
123     plot(f, real(fftshift(fft(yt))))
124     xlabel('Frequency (Hz)')
125     ylabel('EMG amplitude (V/V)')
126     title('Raw EMG Signal (60 Hz Removed)')
127
128     subplot(3,1,2)
129     plot(f, real(fftshift(fft(ywr))))
130     xlabel('Frequency (Hz)')
131     ylabel('EMG amplitude (V/V)')
132     title('Wavelet Denoised Signal')
133
134     subplot(3,1,3)
135     plot(f, real(fftshift(fft(ywrt))))
136     xlabel('Frequency (Hz)')
137     ylabel('EMG amplitude (V/V)')
```

```matlab
138        title('Wavelet Denoised - 16 Hz Line Noise Removed
              Signal')

139

140     %%

141

142 %     [u,v] = envelope(abs(ywrt)); %Detect top and
      bottom envelopes of the data
143 %     j = u; %Copy upper envelope
144 %     j = j - min(u);
145     j = ywrt;
146     k = j(2:end-1).*j(2:end-1) - j(1:end-2).*j(3:end); %
              Teager-Kaiser Discrete Time Energy Operator

147

148     %%
149     % figure
150     subplot(3,1,1)
151     plot(t./60, y)
152     xlabel('Time (Minutes)')
153     ylabel('EMG amplitude (V/V)')
154     title('Raw EMG Signal')

155

156     subplot(3,1,2)
157     plot(t./60, ywrt)
158     xlabel('Time (Minutes)')
159     ylabel('EMG amplitude (V/V)')
```

```matlab
160        title('Final Denoising')
161
162        subplot(3,1,3)
163        plot(t(2:end-1)./60,abs(k))
164        title('Teager-Kaiser Energy Operator')
165        xlabel('Time (Minutes)')
166        ylabel('Normalized Energy (W/W)')
167
168
169    %%
170        save([filepath victim '\EMG.mat'], 'ywrt')
171
172    %%
173        yds = abs(downsample((real(ywrt)), Fs*TR));
174        subplot(2,1,1)
175        plot(t./60, abs(ywrt))
176        xlabel('Time (Minutes)')
177        ylabel('EMG amplitude (V/V)')
178        title('Final Denoising')
179        subplot(2,1,2)
180        tds = 0:300/1200:300-1/4;
181        plot(tds./60,yds)
182        xlabel('Time (Minutes)')
183        ylabel('EMG amplitude (V/V)')
184        title('Final Denoising Downsampled')
```

```
185
186        %%
187        save([filepath victim '\EMG_ds.mat'], 'yds')
188
189    end
```

B.4 Graph Visualization

```matlab
1  function [  ] = Visualize_Graph_EMG( graph , thres , dim
       , anat )
2
3  %% Extract Data from Graph
4
5  tp   = graph.Time_Points;
6  Data = graph.Data_Points;
7  PC   = graph.Node_Positions;
8  N    = graph.Nodes;
9  Nnw  = graph.Node_Weight_dim;
10 New  = graph.Edge_Weight_dim;
11 GT   = graph.Node_Weights;
12 RT   = graph.Edge_Weights;
13 act  = graph.Basis;
14
15 [size_p ~] = size(PC);
16 % disp(PC)
17 disp(size_p)
18
19
20 %% 6. Visualize Graph
21 disp('Visualizing')
22 % thres = 0.8;
```

```matlab
lim = 0.5;
scale = 5;

G = squeeze(GT(dim,:,:,:));
R = squeeze(RT(dim,:,:,:));


h = gcf;
clf
hold off



%For each time point
for k = 1:10:tp

    h1 = subplot(1,2,1);
    cla(h1)



    plot3( PC(1,:), PC(2,:), PC(3,:), 'ko', 'MarkerSize'
        , 10);
    title('Connectome');
    hold on

    for i = 1:N

```

```matlab
47         if (size_p > 3) % If masks have been packaged with
              PC
48            for j = 1:size_p-3 % For each mask vector
49                if (PC(j+3,i) == 1) % If mask vector is a 1
                      at given point
50                    if (j == 1)
51 %                        disp('gas')
52                        plot3(PC(1,i),PC(2,i),PC(3,i),'ko',
                              'MarkerSize', 15 , '
                              MarkerFaceColor' , 'r');
53                    elseif (j == 2)
54                        plot3(PC(1,i),PC(2,i),PC(3,i),'kh',
                              'MarkerSize', 15 , '
                              MarkerFaceColor' , 'm');
55 %                        disp('sol')
56                    elseif (j == 3)
57                        plot3(PC(1,i),PC(2,i),PC(3,i),'kd',
                              'MarkerSize', 15 , '
                              MarkerFaceColor' , 'y');
58 %                        disp('tib')
59                    elseif (j == 4)
60                        plot3(PC(1,i),PC(2,i),PC(3,i),'k+',
                              'MarkerSize', 15 , '
                              MarkerFaceColor' , 'bl');
61                    end
```

```
62                    end
63                end
64            else
65  %     For correlation with the activation function
66            if ( G(i) < 0)
67                plot3(PC(1,i),PC(2,i),PC(3,i),'ko', '
                      MarkerSize', 50*abs( G(i) ) , '
                      MarkerFaceColor' , 'r');
68            else
69                plot3(PC(1,i),PC(2,i),PC(3,i),'ko', '
                      MarkerSize', 50*abs( G(i) ) , '
                      MarkerFaceColor' , 'g');
70            end
71        end
72  %        view(-45,30)
73        view (130, -20)
74        grid('on')
75  %        view(0,-90)
76    end
77
78    for i = 1:N
79        for j = i+1:N
80
81            if ( abs( R(i,j,k) ) < thres  )
82                continue
```

```matlab
83                end
84
85                if ( R(i,j,k) > thres )
86                    plot3([PC(1,i) PC(1,j)],[PC(2,i) PC(2,j)
                            ],[PC(3,i) PC(3,j)],'k-', 'LineWidth'
                            , 0.5)
87                    plot3([PC(1,i) PC(1,j)],[PC(2,i) PC(2,j)
                            ],[PC(3,i) PC(3,j)],'g--', 'LineWidth
                            ', R(i,j,k)*scale)
88                elseif ( R(i,j,k) < -thres )
89                    plot3([PC(1,i) PC(1,j)],[PC(2,i) PC(2,j)
                            ],[PC(3,i) PC(3,j)],'k-', 'LineWidth'
                            , 0.5)
90                    plot3([PC(1,i) PC(1,j)],[PC(2,i) PC(2,j)
                            ],[PC(3,i) PC(3,j)],'r--', 'LineWidth
                            ', abs(R(i,j,k))*scale)
91                end
92
93            end
94        end
95
96    h2 = subplot(2,2,2);
97
98    if (size_p == 3)
99        plot( act(1:tp), 'LineWidth', 3)
```

```
100            title( ['Activation Function: ', num2str(k)] )
101            hold on
102            plot(k,act(k),'.', 'MarkerSize', 50)
103            hold off
104        elseif (size_p > 3)
105 %         for i = 1:N
106 %                    plot(squeeze(Data(1,i,:)))
107 %          %             pause(0.00001)
108 %         end
109            imshow((squeeze(anat(:,:,14))), []);
110            hold on
111            anat_scale = 1;
112            for i = 1:N
113                if (size_p > 3) % If masks have been
                       packaged with PC
114                    for j = 1:size_p-3 % For each mask
                           vector
115                        if (PC(j+3,i) == 1) % If mask vector
                               is a 1 at given point
116                            if (j == 1)
117                                hd1 = plot(anat_scale*PC(1,i
                                   ),anat_scale*PC(2,i), 'ro
                                   ', 'MarkerSize', 10, '
                                   LineWidth', 2, '
                                   MarkerFaceColor', 'r');
```

```
118                        elseif (j == 2)
119                            hd2 = plot(anat_scale*PC(1,i
                               ),anat_scale*PC(2,i), 'mh
                               ', 'MarkerSize', 10, '
                               LineWidth', 2, '
                               MarkerFaceColor', 'm');
120                        elseif (j == 3)
121                            hd3 = plot(anat_scale*PC(1,i
                               ),anat_scale*PC(2,i), 'yd
                               ', 'MarkerSize', 10, '
                               LineWidth', 2, '
                               MarkerFaceColor', 'y');
122                        elseif (j == 4)
123                            hd4 = plot(anat_scale*PC(1,i
                               ),anat_scale*PC(2,i), 'b+
                               ', 'MarkerSize', 10, '
                               LineWidth', 2, '
                               MarkerFaceColor', 'b');
124                        end
125                    end
126                end
127            end
128        end
129    hold off
```

```
130              legend([hd1, hd2, hd3, hd4], {'Gastrocnemius','
                    Soleus','Tibialis', 'EMG'}, 'Location', '
                    east')
131
132          view(270,90)
133      end
134
135
136      h3 = subplot(2,2,4);
137      colormap('default')
138      imagesc(R(:,:,k))
139 %    Add colour bar
140      title( ['Adjacency Matrix at time: ', num2str(k)] )
141      h = colorbar;
142      set(h, 'ylim', [-1 1])
143      set(h, 'location', 'eastoutside')
144
145
146 %    h4 = subplot(2,4,4);
147
148
149      pause(0.1)
150
151
152
```

```matlab
153    end

154    hold off

155

156    disp('Visualize DONE')

157

158

159

160

161    end
```

B.5   Pipeline

```
%% Load in "Verticalized" Data from all Subjects and
    Assign Subject Numbers

% victims= {'Alex', 'Bhanu', 'Calvin', 'Cam', 'Ethan', '
    Josh', 'Neil', 'Sam', 'TJ'};
victims= {'ALEX', 'BHANU', 'CALVIN', 'CAM', 'ESTEBAN', '
    ETHAN', 'JOSH', 'KONRAD', 'TJ', 'YVES'};
% victim = 'ALEX';


filepath = 'C:\Users\sstje\Desktop\Schtough\School\GRAD\
    Signal Processing\FINAL_DATA\FINAL_verts_long\EMG\';

tbl_all_EMG = load([filepath char(victims(1)) '_verts.
    mat']);
% tbl_all.tbl.SubjectNo = ones(height(tbl_all.tbl),1);


%%
i = 2;
for i = 2:length(victims)
    tbl2 = load([filepath  char(victims(i)) '_verts.mat'
        ]);
    %tbl2.tbl.SubjectNo = i*ones(height(tbl2.tbl),1);

```

```
18
19      tbl_all_EMG.tbl = [tbl_all_EMG.tbl; tbl2.tbl];
20      disp(['Loaded: ' char(victims(i))])
21  end
22
23  clear tbl2 victims victim i filepath
24  clearvars -except tbl_all
25
26  %% Run a Fit on the Coalesced Data
27  %{
28  Variables
29  Subject_Number
30  Time_Point
31  Node_Type_N
32  Edge_Type_N
33  Coherence
34  Fractal
35  Edge_Eucl
36  Edge_Dijkstra_C
37  Edge_Dijkstra_CL
38  Edge_Dijkstra_F
39  Edge_Dijkstra_FL
40  EMG
41
42  %}
```

```matlab
43
44 % Cglme = fitglme( tbl_all.tbl, 'Coherence ~ 1 +
      Edge_Eucl + Edge_Dijkstra_C  + EMG + (1|Activation) +
      (1|Subject_Number) ',...
45 %     'DummyVarCoding', 'effects', 'FitMethod', 'mpl')
46
47 Cglme = fitglme( tbl_all_EMG.tbl, 'Coherence  ~ 1 +
      Node_Type_N:Edge_Type_N:EMG + Edge_Eucl +
      Edge_Dijkstra_C + Time_Point + (1|Activation) + (
      Node_Type_N:Edge_Type_N:EMG| Subject_Number)',...
48     'DummyVarCoding', 'effects', 'FitMethod', 'mpl')
49
50
51
52 %%
53 Fglme = fitglme( tbl_all_EMG.tbl, 'Fractal  ~ 1 +
      Node_Type_N:Edge_Type_N:EMG + Edge_Eucl +
      Edge_Dijkstra_C + Time_Point + (1|Activation) + (
      Node_Type_N:Edge_Type_N:EMG| Subject_Number)',...
54     'DummyVarCoding', 'effects', 'FitMethod', 'mpl')
55
56 %%
57
```

```matlab
58  Nglme = fitglme(tbl_all_EMG.tbl, 'Node_Type_N ~ 1 +
        Coherence + Fractal + Edge_Type_N + Edge_Eucl +
        Edge_Dijkstra_C + Edge_Dijkstra_CL + Edge_Dijkstra_FL
         + Time_Point + (1|EMG) + (1|Activation) + (1|
        Subject_Number)',...
59          'DummyVarCoding', 'effects', 'FitMethod', 'mpl')
60
61
62  %%
63
64  Eglme = fitglme(tbl_all_EMG.tbl, 'Edge_Type_N ~ 1 +
        Coherence + Fractal + Node_Type_N + Edge_Eucl +
        Edge_Dijkstra_C + Edge_Dijkstra_CL + Edge_Dijkstra_FL
         + Time_Point + (1|EMG) + (1|Activation) + (1|
        Subject_Number)',...
65          'DummyVarCoding', 'effects', 'FitMethod', 'mpl')
66
67  %%
68
69  diary('Cglme.txt')
70  diary on
71  disp(Cglme)
72  diary off
```

Appendix C

Figures, Rights, and Permissions

Figure 2.2: This figure was published in Plos One, April 2014. With open-access status. **Figure 2.1:** This figure was published in NeuroImage Volume 197, August 2019, Pages 742-760. Copyright Elsevier Inc., 2022.

ELSEVIER LICENSE
TERMS AND CONDITIONS

Aug 04, 2022

This Agreement between McMaster University -- Thaejaesh Sooriyakumaran ("You") and Elsevier ("Elsevier") consists of your license details and the terms and conditions provided by Elsevier and Copyright Clearance Center.

License Number	5361460284631
License date	Aug 03, 2022
Licensed Content Publisher	Elsevier
Licensed Content Publication	NeuroImage
Licensed Content Title	Non-BOLD contrast for laminar fMRI in humans: CBF, CBV, and CMRO2
Licensed Content Author	Laurentius Huber,Kâmil Uludağ,Harald E. Möller
Licensed Content Date	Aug 15, 2019
Licensed Content Volume	197
Licensed Content Issue	n/a
Licensed Content Pages	19
Start Page	742
End Page	760
Type of Use	reuse in a thesis/dissertation
Portion	figures/tables/illustrations
Number of figures/tables/illustrations	1
Format	electronic
Are you the author of this Elsevier article?	No
Will you be translating?	No
Title	An Investigation of Graph Signal Processing Applications to Muscle BOLD and EMG
Institution name	McMaster University
Expected presentation date	Aug 2022
Portions	Graphical Abstract, from Elsevier webpage, not found within paper itself.
Requestor Location	McMaster University 1280 Main Street West

Hamilton, ON L8S4L8 Canada Attn: McMaster University |
Publisher Tax ID	GB 494 6272 12
Total	**0.00 CAD**
Terms and Conditions	

INTRODUCTION

1. The publisher for this copyrighted material is Elsevier. By clicking "accept" in connection with completing this licensing transaction, you agree that the following terms and conditions apply to this transaction (along with the Billing and Payment terms and conditions established by Copyright Clearance Center, Inc. ("CCC"), at the time that you opened your Rightslink account and that are available at any time at http://myaccount.copyright.com).

GENERAL TERMS

ELSEVIER LICENSE
TERMS AND CONDITIONS

This Agreement between McMaster University -- Thaejaesh Sooriyakumaran ("You") and Elsevier ("Elsevier") details and the terms and conditions provided by Elsevier and Copyright Clearance Center.

License Number	5361460284631
License date	Aug 03, 2022
Licensed Content Publisher	Elsevier
Licensed Content Publication	NeuroImage
Licensed Content Title	Non-BOLD contrast for laminar fMRI in humans: CBF, CBV, and CMRO2
Licensed Content Author	Laurentius Huber,Kâmil Uludağ,Harald E. Möller
Licensed Content Date	Aug 15, 2019
Licensed Content Volume	197
Licensed Content Issue	n/a
Licensed Content Pages	19
Start Page	742
End Page	760
Type of Use	reuse in a thesis/dissertation
Portion	figures/tables/illustrations
Number of figures/tables/illustrations	1
Format	electronic
Are you the author of this Elsevier article?	No
Will you be translating?	No
Title	An Investigation of Graph Signal Processing Applications to Muscle BOLD
Institution name	McMaster University
Expected presentation date	Aug 2022
Portions	Graphical Abstract, from Elsevier webpage, not found within paper itself.
Requestor Location	McMaster University 1280 Main Street West
	Hamilton, ON L8S4L8 Canada Attn: McMaster University
Publisher Tax ID	GB 494 6272 12
Total	**0.00 CAD**
Terms and Conditions	

INTRODUCTION

Bibliography

18.7C (July 21, 2018) 18.7C: Blood Flow in Skeletal Muscle Medicine Libre-Texts URL: https://med.libretexts.org/Bookshelves/Anatomy_and_Physiology/Book%3A_Anatomy_and_Physiology_(Boundless)/18%3A_Cardiovascular_System%3A_Blood_Vessels/18.7%3A_Blood_Flow_Through_the_Body/18.7C%3A_Blood_Flow_in_Skeletal_Muscle (visited on 07/16/2022).

Allen, P., Josephs, O., and Turner, R. (Sept. 2000) A Method for Removing Imaging Artifact from Continuous EEG Recorded during Functional MRI *NeuroImage* 12, 230–9.

Baker, J. S., McCormick, M. C., and Robergs, R. A. (2010) Interaction among Skeletal Muscle Metabolic Energy Systems during Intense Exercise *Journal of Nutrition and Metabolism* 2010, 905612 ISSN: 2090-0724.

Battisti, U. and Riba, L. (2016) Window-dependent bases for efficient representations of the Stockwell transform *Applied and Computational Harmonic Analysis* 40.(2), 292–320 ISSN: 1063-5203.

Baudelet, C. and Gallez, B. (2002) How does blood oxygen level-dependent (BOLD) contrast correlate with oxygen partial pressure (pO2) inside tumors? *Magnetic Resonance in Medicine* 48.(6), 980–986.

Behr, M. (2016) Simultaneous Electromyography and Functional Magnetic Resonance Imaging of Skeletal Muscle.

Boxtel, A. van, Boelhouwer, A. J., and Bos, A. R. (Nov. 1998) Optimal EMG signal bandwidth and interelectrode distance for the recording of acoustic, electrocutaneous, and photic blink reflexes *Psychophysiology* 35.(6), 690–697 ISSN: 0048-5772.

Braus, H. (1921) Anatomie des Menschen: ein Lehrbuch für Studierende und Ärzte Berlin , Heidelberg [u.a.]

Chopra, S., Foltz, W. D., Milosevic, M. F., Toi, A., Bristow, R. G., Ménard, C., and A. Haider, M. (Jan. 1, 2009) Comparing oxygen-sensitive MRI (BOLD R2*) with oxygen electrode measurements: A pilot study in men with prostate cancer *International Journal of Radiation Biology* 85.(9), 805–813 ISSN: 0955-3002.

Donahue, K. M., Van Kylen, J., Guven, S., El-Bershawi, A., Luh, W.-M., Bandettini, P. A., Cox, R. W., Hyde, J. S., and Kissebah, A. H. (1998) Simultaneous gradient-echo/spin-echo EPI of graded ischemia in human skeletal muscle *Journal of Magnetic Resonance Imaging* 8.(5), 1106–1113 ISSN: 1522-2586.

Falaschi, P. and Marsh, D., eds. (2021) *Orthogeriatrics: The Management of Older Patients with Fragility Fractures* Cham (CH): Springer ISBN: 9783030481254 9783030481261.

FFT-fast S-transforms (2022) FFT-fast S-transforms: DOST, DCST, DOST2 and DCST2 URL: https://www.mathworks.com/matlabcentral/fileexchange/53910-fft-fast-s-transforms-dost-dcst-dost2-and-dcst2 (visited on 08/03/2022).

Ganesh, G., Franklin, D. W., Gassert, R., Imamizu, H., and Kawato, M. (Jan. 2007) Accurate Real-Time Feedback of Surface EMG During fMRI *Journal of Neurophysiology* 97.(1), 912–920 ISSN: 0022-3077.

Gastrocnemius (2022) UW Radiology URL: https : / / rad . washington . edu / muscle-atlas/gastrocnemius/ (visited on 07/05/2022).

Gastrocnemius | Encyclopedia | Anatomy.app | Learn anatomy | 3D models, articles, and quizzes (2022) URL: https://anatomy.app/encyclopedia/gastrocnemius (visited on 08/04/2022).

Huber, L., Uludağ, K., and Möller, H. E. (Aug. 15, 2019) Non-BOLD contrast for laminar fMRI in humans: CBF, CBV, and CMRO2 *NeuroImage* 197, 742–760 ISSN: 1053-8119.

Human Skeletal Muscle Fiber Type Classifications | Physical Therapy | Oxford Academic (2022) URL: https://academic.oup.com/ptj/article/81/11/1810/2857618?login=false (visited on 07/29/2022).

Institute, N. C. (n.d.) Muscle Tissue URL: https://training.seer.cancer.gov/anatomy/cells_tissues_membranes/tissues/muscle.html.

Jordan, B. F., Kimpalou, J. Z., Beghein, N., Dessy, C., Feron, O., and Gallez, B. (2004) Contribution of oxygenation to BOLD contrast in exercising muscle *Magnetic Resonance in Medicine* 52.(2), 391–396.

Lajoie, I., Tancredi, F. B., and Hoge, R. D. (Sept. 20, 2016) Regional Reproducibility of BOLD Calibration Parameter M, OEF and Resting-State CMRO2 Measurements with QUO2 MRI *PLOS ONE* 11.(9), e0163071 ISSN: 1932-6203.

Ledermann, H. P., Heidecker, H.-G., Schulte, A.-C., Thalhammer, C., Aschwanden, M., Jaeger, K. A., Scheffler, K., and Bilecen, D. (Nov. 2006) Calf Muscles Imaged at BOLD MR: Correlation with TcPo2 and Flowmetry Measurements during Ischemia and Reactive Hyperemia—Initial Experience *Radiology* 241.(2), 477–484 ISSN: 0033-8419.

Leftin, A., Roussel, T., and Frydman, L. (Apr. 25, 2014) Hyperpolarized Functional Magnetic Resonance of Murine Skeletal Muscle Enabled by Multiple Tracer-Paradigm Synchronizations *PLOS ONE* 9.(4), e96399 ISSN: 1932-6203.

Lota, A., Gatehouse, P., and Mohiaddin, R. (July 1, 2017) T2 mapping and T2* imaging in heart failure *Heart Failure Reviews* 22.(4), 431–440 ISSN: 1573-7322.

McLean, S., Lomber, S., Beye, A., Ciriello, J., Stavraky, T., and Woods, A. (2018) Introduction to Human Physiology: Fourth Custom, Edition for Western University Canada Pearson ISBN: 0-135-39238-1.

Michel, M., Gulac, P., Fischer, K., Jung, B., Longnus, S. L., and Guensch, D. P. (June 1, 2019) 22Effects of myoglobin oxygenation on oxygenation-sensitive cardiovascular magnetic resonance images: an in-vitro study *European Heart Journal - Cardiovascular Imaging* 20 (Supplement_2), jez111 ISSN: 2047-2404.

Murphy, A. and Gaillard, F. (2008) BOLD imaging URL: `https://radiopaedia.org/articles/bold-imaging?lang=us`.

Muscle Fibre Types (2022) Physiopedia URL: `https://www.physio-pedia.com/Muscle_Fibre_Types` (visited on 07/29/2022).

Niazy, R., Beckmann, C., Iannetti, G., Brady, J., and Smith, S. (2005) Removal of FMRI environment artifacts from EEG data using optimal basis sets *NeuroImage* 28.(3), 720–737 ISSN: 1053-8119.

Nishii, T., Kono, A. K., Nishio, M., Kyotani, K., Nishiyama, K., and Sugimura, K. (2015) Dynamic Blood Oxygen Level-dependent MR Imaging of Muscle: Comparison of Postocclusive Reactive Hyperemia in Young Smokers and Non-smokers *Magnetic Resonance in Medical Sciences* advpub, 2014–0105.

Noto, R., Leavitt, L., and Edens, M. (2020) Physiology, Muscle URL: `https://www.ncbi.nlm.nih.gov/books/NBK532258/`.

Ogawa, S., Lee, T. M., Kay, A. R., and Tank, D. W. (Dec. 1990) Brain magnetic resonance imaging with contrast dependent on blood oxygenation. *Proceedings of the National Academy of Sciences* 87.(24), 9868–9872.

Ortega, A., Frossard, P., Kovačević, J., Moura, J. M. F., and Vandergheynst, P. (Mar. 26, 2018) *Graph Signal Processing: Overview, Challenges and Applications.*

Partovi, S., Karimi, S., Jacobi, B., Schulte, A.-C., Aschwanden, M., Zipp, L., Lyo, J. K., Karmonik, C., Müller-Eschner, M., Huegli, R. W., Bongartz, G., and Bilecen, D. (2012) Clinical implications of skeletal muscle blood-oxygenation-level-dependent (BOLD) MRI *Magnetic Resonance Materials in Physics, Biology and Medicine* 25.(4), 251–261 ISSN: 0968-5243.

Patten, C., Meyer, R. A., and Fleckenstein, J. L. (2003) T2 Mapping of Muscle *Seminars in Musculoskeletal Radiology* 7.(4), 297–307 ISSN: 1089-7860, 1098-898X.

Piovanelli, E., Piovesan, D., Shirafuji, S., Su, B., Yoshimura, N., Ogata, Y., and Ota, J. (Jan. 2020) Towards a Simplified Estimation of Muscle Activation Pattern from MRI and EMG Using Electrical Network and Graph Theory *Sensors* 20.(3), 724 ISSN: 1424-8220.

Robert, B. W., Y.-C., C. N., E., H. M., Michael, T. R., and Ramesh, V. (2014) Magnetic Resonance Imaging: Physical Principles and Sequence Design, 2nd Edition WILEY-Blackwell ISBN: 978-0-471-72085-0.

Robinson, S. P., Howe, F. A., Rodrigues, L. M., Stubbs, M., and Griffiths, J. R. (July 1, 1998) Magnetic resonance imaging techniques for monitoring changes in tumor oxygenation and blood flow *Seminars in Radiation Oncology* Tumor Physiology and Metastases 8.(3), 197–207 ISSN: 1053-4296.

Rockel, C. P. (2017) Temporal Diffusion MRI of Post-Exercise Human Calf Muscles Thesis.

Rodríguez-Carreño, I., Gila-Useros, L., and Malanda-Trigueros, A. (2012) Motor Unit Action Potential Duration: Measurement and Significance in: *Advances in Clinical Neurophysiology* ed. by I. M. Ajeena Rijeka: IntechOpen chap. 7.

Soleus (2022) UW Radiology URL: `https://rad.washington.edu/muscle-atlas/soleus/` (visited on 07/05/2022).

Sumanth (2022) Simple Higuchi Fractal Dimension Implementation URL: `https://www.mathworks.com/matlabcentral/fileexchange/36027-simple-higuchi-fractal-dimension-implementation` (visited on 08/03/2022).

T., K., Sehgal, P., Jasuja, N., and Park, Y. (2013) Aerobic vs. Anaerobic Respiration URL: `https://www.diffen.com/difference/Aerobic_Respiration_vs_Anaerobic_Respiration`.

Tang, I.-N., Jao, T., Huang, Y.-A., Li, C.-W., Yu, Y.-C., and Chen, J.-H. (Oct. 1, 2020) A new MRI subject position to explore simultaneous BOLD oscillations of the brain and the body *Journal of Neuroscience Methods* 344, 108829 ISSN: 0165-0270.

Tibialis Anterior (2022) UW Radiology URL: `https://rad.washington.edu/muscle-atlas/tibialis-anterior/` (visited on 07/05/2022).

Towse, T. F., Childs, B. T., Sabin, S. A., Bush, E. C., Elder, C. P., and Damon, B. M. (2016) Comparison of muscle BOLD responses to arterial occlusion at 3 and 7 Tesla *Magnetic Resonance in Medicine* 75.(3), 1333–1340 ISSN: 1522-2594.

Uwano, I., Kudo, K., Sato, R., Ogasawara, K., Kameda, H., Nomura, J.-i., Mori, F., Yamashita, F., Ito, K., Yoshioka, K., and Sasaki, M. (Aug. 2017) Noninvasive Assessment of Oxygen Extraction Fraction in Chronic Ischemia Using Quantitative Susceptibility Mapping at 7 Tesla *Stroke* 48.(8), 2136–2141.

Vadera, S. and Jones, J. (2009) T1 Weighted Image URL: `https://radiopaedia.org/articles/t1-weighted-image`.

Wang, Y.-h. (n.d.) *1 The Tutorial: S Transform.*

Wilkinson, D. J., Piasecki, M., and Atherton, P. J. (Nov. 1, 2018) The age-related loss of skeletal muscle mass and function: Measurement and physiology of muscle fibre atrophy and muscle fibre loss in humans *Ageing Research Reviews* 47, 123–132 ISSN: 1568-1637.

Zamparo, P., Minetti, A., and Prampero, P. di (2022) Interplay among the changes of muscle strength, cross-sectional area and maximal explosive power: theory and facts | SpringerLink ().